Alkane Dehydrogenation in Scalable and Electrifiable Carbon Membrane Reactor

Authors: Lu Liu^{1†}, Antara Bhowmick^{2†}, Sichao Cheng^{1†}, Borja Hernandez Blazquez², Ying Pan¹, Junyan Zhang¹, Yuan Zhang³, Yuying Shu⁴, Dat T. Tran⁵, Yuqing Luo², Marianthi Ierapetritou², Chen Zhang^{1*}, Dongxia Liu^{1,2,6*}

Affiliations:

¹Department of Chemical and Biomolecular Engineering, University of Maryland; College Park, Maryland, 20742, United States.

²Department of Chemical and Biomolecular Engineering, University of Delaware; Newark, 19716, Delaware, United States.

³Department of Chemistry and Biochemistry, University of Maryland; College Park, Maryland, 20742, United States.

⁴W.R. Grace; Columbia, Maryland, 21044, United States.

⁵DEVCOM Army Research Laboratory; Adelphi, Maryland, 20783, United States.

⁶Lead contact

†These authors contributed equally to this work.

*Correspondence: czhang71@umd.edu; liud@udel.edu

Summary: Non-oxidative alkane dehydrogenation produces alkene and hydrogen products. The current processes face three challenges: limited conversion due to thermodynamics, rapid catalyst deactivation, and CO₂ emissions from process heating. A membrane reactor (MR) has potential to overcome the thermodynamic limit by removing H₂ in situ, but both catalyst and membrane tend to deactivate quickly. Here we report a carbon membrane reactor that integrates H₂-permeable carbon molecular sieve (CMS) hollow fiber membranes and siliceous zeolite supported metal catalysts. By lowering the reaction temperature using catalysts with a low threshold temperature and by overcoming the thermodynamic limit with CMS membranes, we achieve high conversion and catalyst stability. The electro-conductive nature of the CMS membrane enables Joule heating of the reaction, reducing CO₂ emissions. We demonstrate the CMS membrane reactor with recordhigh stability for propylene and ethylene production, the second and first-largest-volume chemicals used as feedstock globally.

Keywords: alkane dehydrogenation, metal/zeolite catalyst, carbon molecular sieve, membrane reactor, electrified process heating, carbon emission.

Introduction:

Light alkenes are extensively used as chemical building blocks in the production of important industrial products, including polymers, oxygenates, and chemical intermediates. The abundant and inexpensive natural gas liquids (NGLs) in the U.S. shift the light alkenes production from cracking of oil-based naphtha to dehydrogenation of shale-based light hydrocarbons¹⁻⁴. Nonoxidative dehydrogenation is an on-purpose technology to exclusively yield a particular alkene and hydrogen (H₂) from the corresponding alkane. The endothermic nature of the non-oxidative dehydrogenation reaction, however, requires high temperature to attain attractive conversion for industrial applications^{5,6}. The high temperature results in side reactions (i.e., cracking and coke formation) and catalyst deactivation by coking or sintering. Constant catalyst regeneration through oxidative de-coking and re-reduction cycles is required in commercial moving or fix-bed reactors^{7,8}. Alkane dehydrogenation reactors are traditionally heated by fossil fuel firing that contributes to ~30% CO₂ emissions. Membrane reactors (MRs) have the potential to overcome the thermodynamic limit by in-situ removal of by-product, resulting in increased product yields, lower reaction temperatures, and higher energy efficiency⁹⁻¹¹. Although the concept is highly attractive, alkane dehydrogenation MRs have not been practiced in industry due to two major challenges: catalyst and membrane have accelerated coking and deactivation due to H₂ depletion, and the inorganic or metallic membranes are costly to fabricate at large scale.

Taking propylene (C₃H₆) as an example, it is the second largest-volume chemical used as feedstock after ethylene globally. Non-oxidative propane (C₃H₈) dehydrogenation (PDH) to produce C₃H₆ and H₂ holds great promise to meet the increasing global C₃H₆ demand^{3,4}. State-of-the-art commercial PDH reactions employ alumina supported chromium oxide (Cr₂O₃/Al₂O₃) or platinum-tin (Pt-Sn/Al₂O₃) catalysts operated at temperature ~600-650 °C⁶. While good propane conversion (~35-50%) and C₃H₆ selectivity (~80-90%) can be achieved, the catalysts must be regenerated periodically (Cr₂O₃/Al₂O₃, every 7-15 minutes; Pt-Sn/Al₂O₃, every 7-10 days) to remove coke deposit and maintain activity¹². Process heat from direct fired furnaces¹³ or catalyst coke combustion^{14,15} produces CO₂ emissions. MRs comprising H₂-permeable palladium (Pd)based metal or inorganic oxide (alumina, silica or zeolite) membranes in combination with PDH catalysts have been actively pursued to reaching high conversions at low rection temperatures since the 1990s¹⁶. Rapid drop of conversion was typically observed in Pd-based MRs due to severe deactivation of membrane and catalyst materials. Although inorganic oxide MRs had better stability, propane conversion enhancement was low16. To date, achieving high C3H8 conversion, high C₃H₆ yield, high catalyst durability, and low CO₂ emissions in non-oxidative PDH remains a grand challenge.

Herein, we report the first stable, active, selective, and low CO₂ emissive on-purpose alkane dehydrogenation membrane reactor technology using scalable MRs (**Figure 1A**) consisting of a siliceous zeolite confined metal (i.e., M/zeolite) catalyst and an asymmetric carbon molecular sieve (CMS) hollow fiber membrane. The absence of Lewis and Brønsted acidic centers in the siliceous zeolite eliminates acid-catalyzed side reactions such as cracking and oligomerization that lead to low alkene selectivity and catalyst deactivation due to coke deposition. The small metal clusters are effective for alkane activation and suppression of side-reactions involving hydrogenolysis (C-C cleavage) and/or coke formation (C-C coupling) occurred on geometrically complex and large ensembles of metal atoms^{6,17,18}. The confinement of zeolite micropores prevents metal site sintering and the consequent deactivation¹⁹⁻²³. For the first time, asymmetric CMS hollow fine fiber (~300 μm outer diameter) membranes are used for MRs. Their thin separation layer allows rapid H₂ removal from the reaction mixture, thereby up shifting the reaction equilibrium to reach high conversions at low reaction temperatures. In comparison to catalysts (**Figure 1B**) and

membranes (**Figure 1C**) that were used in PDH MRs in literature, the CMS MR reaches up to 3 times as high as propane equilibrium conversion, record-low deactivation rate (**Figure 1D**) and excellent long-term durability (**Figure 1E**). The small diameter of the CMS hollow fibers gives significantly higher packing density and flexibility than conventional tubular or monolith inorganic membranes used for PDH MRs, and therefore are more suitable for large-scale applications^{24,25}. Additionally, the electro-conductive nature of the CMS hollow fibers allows them as the Joule-heating media to supply process heat from renewable electricity. This allows the invention of an electrifiable MR to reduce CO₂ emissions, distinct from all existing MR studies in alkane dehydrogenation.

Results and discussion:

PDH in CMS membrane reactor

The CMS hollow fiber membranes (**Figures 2A-B**) were made by pyrolysis (550 °C) of Matrimid[®] polyimide precursor hollow fiber membranes fabricated by dry-jet/wet-quench spinning²⁶. The precursor hollow fibers were pre-treated by vinyltrimethoxysilane to provide the asymmetric structure characterized by a porous substrate and a thin dense separation layer (~4.5 µm)²⁷. This asymmetric structure gives the CMS hollow fiber membrane simultaneously attractive H₂ permeance and high H₂/C₃H₈ separation factor that increases with operation temperature (**Figure 2D**). The silicalite-1 supported platinum (Pt) and zinc (Zn) (i.e., Pt-Zn/S1, **Figure 2C**) was used for non-oxidative PDH, which was hydrothermally synthesized (section S1.2.1). The physiochemical property characterizations (sections S2.2.1 and S2.2.2) confirmed the catalyst structure integrity. The catalyst tests in a packed-bed reactor (PBR) showed excellent stability (**Figure 1E**) and low threshold activation temperature (**Figure 2E**), as PDH over the Pt-Zn/S1 catalyst attained equilibrium conversions (section S1.5.4) at temperatures as low as 275 °C.

The CMS hollow fiber MR was assembled by packing the Pt-Zn/S1 catalyst on the shell side of CMS hollow fiber membranes (Figure 1A and Figure S2). The PDH reaction was carried out by flowing a C₃H₈/Ar mixture on the shell side and an inert sweep (Ar) to carry away the H₂ permeate on the bore side. We studied the roles of variables on C₃H₈ conversion and C₃H₆ selectivity (Figures 2E-I). As the reaction temperature increased from 350 to 500 °C, the C₃H₈ conversion increased from 3.2 to 36.0% (Figure 2E), which can be explained by the endothermic reaction nature. Increasing the reaction temperature caused the C₃H₆ selectivity to drop from nearly 100.0% to 92.8%, likely because side reactions such as cracking and cyclization that occurred at higher temperatures. As the number of CMS hollow fibers increased from 0 (i.e., PBR) to 19, the C₃H₈ conversion increased from 12.4% to 46.8%, almost quadrupling the thermodynamic equilibrium conversion (Figure 2F). Larger number of CMS hollow fibers increases the membrane permeation area and hence the H₂ permeation flow rate. The higher H₂ permeation flow rate reduces H₂ partial pressure in the reaction side, which drives the reversible PDH reaction forward according to the Le Chatelier's principle. As the WHSV of the propane feed decreased from 3.46 to 0.35 h⁻¹ at 450 °C, C₃H₈ conversion increased and the C₃H₆ selectivity dropped. Membrane reactors with more CMS fibers (19 fiber) and operated at higher temperature (500 °C) can be used to achieve commercially attractive conversion (36.5%) under high WHSV (3.46 h⁻¹) (Figure 2G). As the C₃H₈ feed partial pressure decreased from 80 to 10 kPa, C₃H₈ conversion increased with almost constant C₃H₆ selectivity (Figure 2H). As the sweep flow rate increased from 10 to 200 mL min⁻ ¹, both C₃H₈ conversion and C₃H₆ selectivity increased (**Figure 2I**). The enhanced conversion at

higher sweep flow rate can be attributed to increased H₂ permeation flux, which was due to lower permeate H₂ partial pressure and increased H₂ permeation driving force. The higher H₂ permeation flux also reduces H₂ partial pressure in the reaction side, which suppresses side reactions such as hydrogenolysis and hence increases the C₃H₆ selectivity.

The parametric studies guided the optimal CMS MR operation conditions in the long-term PDH test (Figure 1E). At 450 °C, after time-on-stream (TOS) of ~5 h (i.e., induction period), the MR achieved 34.1% C₃H₈ conversion, 2.4 times as high as that in PBR (14.0%). The MR also showed higher C₃H₆ selectivity (~97.1%) than the PBR (~89.4%). The enhanced conversion and selectivity allowed the CMS MR to improve C₃H₆ yield (i.e., 2.7 times as high as the PBR). It should be noted that the CMS MR had excellent stability for at least 110 h with a slight drop of C₃H₈ conversion (34.1% to 31.3%) and slightly increased C₃H₆ selectivity (97.1% to 98.3%). The slight decrease in C₃H₈ conversions could be due to catalyst coking, which was observed in thermo-gravimetric analysis of spent Pt-Zn/S1 catalyst showing 1.9% weight loss. The analysis on the spent membrane reactor did not show obvious particle sintering in catalyst (Figures S3 and S4) or morphology change in the CMS membrane (Figure S8). The catalyst activity can be recovered by exposing the spent catalyst to a H₂ gas flow at 500°C for 1 h (section S5). A dual-zone fluidized bed membrane reactor design can be used to counteract the catalyst deactivation/regeneration in continuous PDH operation²⁸. The increase in C₃H₆ selectivity was possibly due to the suppression of cracking reactions by absence of catalyst acidity and lowering of H₂ pressure in the shell side²⁹. This phenomenon was also reported by groups using the zeolite-based PDH membrane reactor, where propylene selectivity in MR was higher than that in PBR³⁰⁻³². Remarkably, the activity of the PDH catalyst can be recovered by removal of carbon deposits in a H₂ gas stream (Figure S12A). Compared with PDH MRs found in literature (Table S10), the CMS MR excels by having high conversion enhancement (Figures 1B-D), low operation temperature (Figure 1C), and the lowest deactivation rate (Figure 1D).

EDH in CMS membrane reactor

The attractive performance in PDH provided by the CMS hollow fiber MR is applicable to broader dehydrogenation chemistry of other alkanes such as ethane (C2H6), the most abundant NGL component. Ethylene (C₂H₄) is widely used in the chemical industry and is the most produced organic compound globally. The on-purpose ethylene (C₂H₄) production from non-oxidative ethane dehydrogenation (EDH) is an appealing on-purpose technology in the chemical industry^{1,3,4}. The higher C-H bond stability in ethane than that of propane requires a higher activation temperature for C₂H₄ production. Hence, we customized both CMS membrane and M/zeolite catalyst in the CMS MR for EDH. The CMS hollow fiber membrane was pyrolyzed at a higher temperature (675°C) to provide an attractive separation factor (Figure 3A) for the H_2/C_2H_6 gas pair (2.6 vs 3.9 Å), which is more closely sized than the H_2/C_3H_8 pair (2.6 vs 4.1 Å). The cobalt in dealuminated beta zeolite (i.e., Co/deAl-BEA) catalyst was prepared (section S1.2) and characterized (section S2.2.3) for EDH. The Co/deAl-BEA catalyst attained near-equilibrium conversion in PBR at temperature as low as 400 °C (Figure 3B) and showed no deactivation in a long-term stability test (Figure 3C). At 500 °C, in the initial stage of the TOS test, the CMS MR showed 16.6% C₂H₆ conversion, 2.5 times as high as the equilibrium conversion (6.7%). The C₂H₄ selectivity was also higher in the CMS MR (82.6%) than the PBR (71.3%), similar to the PDH study (Figure 1E). A drop in C₂H₆ conversion (16.6% to 12.4%) accompanied with an increase in C_2H_4 selectivity (82.6% to 94.4%) was observed after the TOS of ~110 h (Figure 3C). Compared to PDH, the conversion drop in EDH was more noticeable, which could be due to more carbonaceous deposit in the catalyst at the higher operation temperature. Notably, the EDH catalyst can fully recover its activity after calcination treatment in air (**Figure S12B**). The CMS MR showed high C₂H₆ conversion enhancement, low operation temperature, and the lowest deactivation rate than EDH MRs reported in literature (**Figures 3D-F** and Table S11).

Electrifiable CMS membrane reactor

To reduce CO₂ emissions from heating endothermic alkane dehydrogenation reactors, we employed Joule heating of the CMS hollow fiber membrane which benefits from the electrical conductivity of its conjugated electronic structure. While Joule-heated reactors have been reported in literature ³³⁻³⁵, to our best knowledge, Joule-heated MRs have not been explored. To electrify the MR, we assembled a CMS hollow fiber membrane with electrodes and placed it in a quartz tube housing with catalyst loaded on the shell side of the CMS hollow fiber membrane (Figure S13). Effective Joule heating of the CMS hollow fiber membrane was evidenced by color change as a direct current (DC) passed through (Figure 4A). In the absence of an external electric furnace, the CMS hollow fiber membrane functions as a Joule heating element to heat the catalyst bed for the PDH reaction. We conducted computational fluid dynamic modelling using COMSOL 6.0 in a two-dimensional (2D) axisymmetric geometry (Figure S14) with coupled equations for fluid motion, energy transport, and mass transport to determine the catalyst bed temperature (section S6). The simulated temperature is consistent with the one measured experimentally (Figure S15), indicating the effectiveness of the model. The simulated 2D axisymmetric temperature profile of Joule-heated CMS MR shows non-uniform temperature along both axial and radial directions (Figure 4B). The PDH reactions, however, take place effectively in the electrified CMS MR, as shown by higher propane conversions at higher catalyst bed temperatures (Figure 4C). The electrified CMS reactor is compact, efficient, and amenable to scaling up as the CMS hollow fibers are heating elements that eliminate the fuel-fired units required in commercial PDH processes.

Process simulation

We performed process simulations using Aspen Plus v.11 (section S7) for the electrifiable CMS MR to assess its commercial feasibility for PDH. The process contains propane feed and steam sweep streams, a CMS MR, H₂/C₃H₆/steam and C₃H₆/C₃H₈ separation units, and recycling of unreacted C₃H₈ and steam (**Figure 4D**). We developed an isothermal model to simulate the outputs from the PDH MR using the rate equation of the Pt-Zn/S1 catalyst and H₂/C₃H₆/C₃H₈ membrane permeation fluxes. The rate equation was derived from the Langmuir-Hinshelwood microkinetic model (section S3.1) and was determined under differential conditions in the PBR (section S3.2). The membrane permeation fluxes were calculated using the measured membrane permeance (Figure 2D). The inputs and outputs from the model were integrated into the PDH plant operation process. We compared the electrified CMS MR process to the commercial Catofin and Oleflex processes. The technoeconomic analysis (TEA) results (section S7.5.1) show that the commercial processes are more profitable than the Joule-heated PDH process in the CMS MR. A comparison of the cost breakdown for minimum selling price (MSP) of propylene (Figure 4E) indicates the price of electricity for Joule-heating is up to ~10 times as high as the process heat from fossil-fired furnaces, which is the major factor making the CMS MR less profitable. The membrane price also increases the investment costs, contributing to a higher MSP (Table S18). The MSP of propylene,

however, decreases steeply with conversion enhancement in the CMS MR and reduction of the energy consumption in the separation units in the designed PDH processes.

Life cycle analysis (LCA) was performed by comparing the CO_2 emissions from the commercial PDH processes with those from the CMS MRs heated by different electricity sources (section S7.5.2). When the electricity is from the U.S. grid, the PDH MR generates more CO_2 emissions (**Figure 4F**), which is mainly caused by two factors: (1) ~70% of electricity in the U.S. grid is from the fossil-based resources and (2) the use of electricity for process heat is less efficient than the production of steam by fossil fuel combustion. When the power source is provided by fully renewable electricity or nuclear power, the propylene production in the PDH in the electrifiable CMS MR reduces the CO_2 emissions by up to 20% (**Figure 4F** and section S7.5.2). The reduced CO_2 emissions is an important step towards the decarbonization of the industrial sector and the development of green, sustainable chemical manufacturing plants.

In summary, we demonstrate a scalable and electrifiable carbon MR for non-oxidative alkane dehydrogenation by coupling active and stable zeolite confined metal catalysts for lowtemperature alkane activation and H₂-permselective asymmetric CMS hollow fine fiber membranes for fast H₂ removal. The synergy between the M/zeolite catalyst and CMS membrane enables unprecedented enhancement in alkane conversion, alkene yield, and catalyst stability. The electro-conductive nature of the CMS hollow fibers enables the replacement of fossil fuel heating with Joule-heating to reduce CO₂ emissions. In non-oxidative PDH, the MR significantly improved C₃H₈ conversion (e.g., nearly 3 times the equilibrium conversion) and C₃H₆ selectivity, and reduced CO₂ emissions (up to 20%). Notably, the attractive performance was obtained at reaction temperature at least 150 °C below commercial PDH reactors, which suppressed coking and therefore allowed the MR to show outstanding stability far exceeding any known MR reported in PDH literature. The CMS MR can be adapted to other alkane dehydrogenation reactions such as EDH. To our best knowledge, this is the first scalable and electrifiable alkane dehydrogenation MR using scalable carbon hollow fine fiber membranes with high membrane packing density. The present work paves the road for green and sustainable on-purpose alkene and hydrogen production, and more broadly equilibrium-limited chemical manufacturing.

Experimental procedures:

Resource availability:

Lead contact

Further information and requests for resources should be directed to and will be fulfilled by the lead contact, Dongxia Liu (liud@udel.edu).

Materials availability

This study did not generate any new materials.

Data and code availability

All data associated with this study are included in the report and the supplemental information. Additional information is available from the corresponding authors upon reasonable request.

Platinum-zinc/silicalite-1 catalyst for non-oxidative PDH

Platinum-zinc/silicalite-1 (Pt-Zn/S1) catalyst was prepared by in-situ hydrothermal synthesis following an adapted precedure ^{20,36,37}. The Pt precursor (i.e., [Pt(NH₂CH₂CH₂NH₂)₂]Cl₂) solution was prepared by dissolving 0.24 g of PtCl₂ in an aqueous solution containing 9.00 g of DI water and 1.15 g of ethylenediamine. The Zn precursor (i.e., [Zn(NH₂CH₂CH₂NH₂)₃](acac)₂) solution was prepared by dissolving 0.84 g of Zn(acac)₂·xH₂O in an aqueous solution containing 8.00 g of DI water and 2.32 g of ethylenediamine. 2.64 g of [Pt(NH₂CH₂CH₂NH₂)₂]Cl₂ solution was added into a TPAOH solution that was prepared by mixing 26.00 g of 40 wt% TPAOH with 30.00 g of DI water. The mixture was stirred for 10 min followed by addition of 16.64 g TEOS. After continuous stirring for 6 h, 2.98 g of [Zn(NH₂CH₂CH₂NH₂)₃](acac)₂ solution was added. The mixture was further stirred for 30 min and then transferred into Teflon lined stainless steel autoclaves. The autoclaves were placed in a convection oven at 170 °C for 3 days under static condition. After the hydrothermal synthesis, the sample was collected by centrifugation and washed by DI water. The centrifugation and DI water washing steps were repeated until pH of the washing solution was about 9. The sample was dried in a convection oven at 70 °C overnight. The dried catalyst sample was pressed into a pellet, crashed, and sieved to maintain 180-425 µm particle size range.

Hollow fiber membrane preparation

Formation of polymer precursor hollow fiber membrane

Matrimid[®] precursor hollow fibers were formed using the dry-jet/wet-quench fiber spinning process with a custom-built hollow fiber spinning system (**Figure S1**). The polymer dope composition³⁸ and spinning parameters are summarized in Tables S1 and S2, respectively. Matrimid[®] 5218 polyimide powder was dried under vacuum at 110 °C overnight before dope preparation. The as-spun polymer hollow fibers were sequentially soaked in three separate DI water baths over the course of 72 h, three separate 20 min methanol baths, and three 20 min hexane baths. The polymer hollow fibers were dried in a fume hood overnight before being dried under vacuum at 75 °C for 12 h.

Formation of carbon molecular sieve (CMS) hollow fiber membrane

Silane pretreatment of precursor hollow fibers was performed to resist substrate collapse of CMS hollow fiber membranes during pyrolysis. The precursor hollow fibers were soaked in a 10 wt% VTMS/hexane solution for 24 h and then exposed to water-vapor saturated air for another 24 h. The VTMS-treated precursor hollow fibers were vacuum dried at 150 °C for 12 h prior to pyrolysis. The treated precursor hollow fibers were firstly placed into an "U"-shaped quartz reactor (outer diameter (OD):6.35 mm; inner diameter (ID): 4.35 mm), and then the quartz-reactor was loaded into a straight quartz tube (OD: 60 mm; ID: 54 mm, MTI Corporation, Richmond, CA) and heated in a three-zone tube furnace (MTI Corporation, Richmond, CA). Ultra-high purity Argon was introduced to the quartz tube at 500 mL min⁻¹ via a mass flow controller (MTI Corporation, Richmond, CA). The system oxygen level was kept below 5 ppm prior to pyrolysis, which was monitored by an oxygen analyzer (Cambridge Sensotec, Saint Ives, UK). In the pyrolysis process, the precursor fibers were first heated from room temperature to 250 °C at a rate of 0.22 °C s⁻¹. The temperature was then increased to Tfinal-15 (Tfinal is the final pyrolysis temperature) at a rate of 0.0642 °C s⁻¹ followed by increasing to T_{final} at a rate of 0.00417 °C s⁻¹. The value of T_{final} was set as 550 °C for CMS hollow fiber membranes for propane dehydrogenation and 675 °C for CMS membranes for ethane dehydrogenation. The heating was then held at T_{final} for 2 h and naturally cooled down to room temperature.

Alkane dehydrogenation in a CMS membrane reactor

The membrane reactor module shown in **Figure S2C** was used for testing alkane dehydrogenation in the membrane reactor conditions. Prior to the reaction test, the membrane reactor system was firstly flushed with the Ar gas flow (20 mL min⁻¹) overnight, as described for the separation tests in Section S1.3.2. Then the Ar gas flow in the shell side was switched to a mixture gas H_2/N_2 (20 mL min⁻¹, H_2/N_2 =1:5, ultrapure, Air gas) to pretreat the catalyst at 500 °C (0.0167 °C s⁻¹) for 3 h prior to reach the reaction temperature. The H_2/N_2 gas flow in the shell side was then switched back to the Ar flow to flush out of the residue H_2 gas in the reactor system. Afterwards, the Ar gas flow was switched to alkane (i.e., $C_x H_{2x+2}$, x = 3 for propane (C₃H₈) or x = 2 for ethane (C₂H₆), Research grade, Matheson) mixed with the Ar internal standard (ultra-high purity, Airgas) to start the dehydrogenation reaction. The bore side of the membrane reactor was kept with Ar gas flow in all these catalyst pretreatment and catalysis testing steps.

Experimental setup for electrifiable CMS membrane reactor

Joule heating of the CMS hollow fiber requires different design from the membrane module that was designed for the process heat from an external furnace (Figure S2C in Section S1.3). A straight reactor module was used in the experiment, as shown in Figure S13. Firstly, the CMS hollow fiber was prepared following the procedure described above. The Pt-Zn/S1 catalyst was pretreated using the setup for PBR testing in Section S1.4. The CMS hollow fiber and PDH catalyst were then assembled into the straight quartz reactor (OD: 6.35 mm) using stainless steel Swagelok® fittings. The assembly started from connecting the copper wire and the CMS hollow fiber with two pieces of copper foils (one at each side) at the indicated places in Figure S13B. The copper foil serves as a bridge to electrically connect copper wire with CMS hollow fiber while the copper wire does not go through the catalyst bed (Figure S13C). The connected copper wire and CMS hollow fiber (length: 150 mm) was placed into the quartz tube (length: 200 mm), and the quartz tube connected to two Swagelok® Ultra-Torr Tee fittings (one at each side). Two short pieces of quartz tube were connected to the second opening of these two Ultra-Torr Tees (Figure S13A). In order to acquire the reactor temperature, a thermocouple (K-type, OD: 0.25 mm, Omega) was placed into a silica capillary tube (ID: 0.53 mm, Restek) with one end closed. The silica capillary tube together with the thermocouple inside was aligned next to the CMS hollow fiber in the quartz reactor. Both ends of the CMS hollow fiber were connected to the silica capillaries for sweep gas delivery (Figure S13A). Epoxy (Duralco 120, Cotronics) was applied to all the connection positions to avoid gas leakage.

The next step is to load catalyst and to connect the module with the reactor rig for the catalysis testing. Prior to adding the catalyst, a pieces of quartz wool was inserted from the third opening of the Ultra-Torr Tee fitting and then positioned next to one of the copper foil connector inside the module. The Pt-Zn/S1 catalyst diluted with acid-washed quartz particles was loaded into the reactor from the same opening where the quartz wool went through. The catalyst bed stayed on the top of the quartz wool (**Figure S13C**). The quartz capillary tube that was connected to the CMS hollow fiber was connected to the propane feed gas delivery tunings. The third openings of the Tees were connected to the sweep gas delivery tubing. For the electrical circuit, the DC power source (Starpower) is directly connected to the Joule heating CMS membrane reactor. The reactor temperature is controlled by the DC power source under constant voltage mode. Temperature along the catalyst bed was recorded in-situ through moving the thermocouple position in the catalyst bed.

Acknowledgements:

The authors gratefully acknowledge the funding support from the National Science Foundation (NSF-CBET 1928325). The authors gratefully acknowledge the Maryland NanoCenter, the Surface Analysis Center, and the AIM Lab. D. L. gratefully acknowledges the support from the Department of Energy, Office of Fossil Energy (DE-FE0031877). C. Z. thanks faculty summer support from the Minta Martin Award and the Huntsman Corporation for kindly providing Matrimid® polymer samples. L. L. is grateful for the Hulka Energy Research Fellowship provided by the Maryland Energy Innovation Institute.

Author contributions:

L.L. prepared CMS membranes, conducted MR test, and collected data for PDH. A.B. synthesized catalysts for PDH, conducted MR test, and collected data for EDH. S.C. designed and conducted electrified MR tests and simulations. Y.P. and D.T.T. designed and constructed MR test facility. J.Z. synthesized the catalysts for EDH. Y.Z. helped with catalyst characterizations. B.H.B, Y.L. and M.I. conducted process simulation and LCA for the PDH processes. Y.S. did composition analysis for catalysts. C.Z. and D.L. supervised the project. All authors discussed the results and contributed to the final manuscript preparation.

Declaration of interests:

A patent application (U.S. Provisional Application No. 63/368,248) on this work was filed.

References:

- 1. Amghizar, I., Vandewalle, L.A., Van Geem, K.M., and Marin, G.B. (2017). New Trends in Olefin Production. Engineering *3*, 171-178. https://doi.org/10.1016/J.ENG.2017.02.006.
- 2. Malakoff, D. (2014). The gas surge. Science 344, 1464-1467. 10.1126/science.344.6191.1464.
- 3. National Academies of Sciences, E.M., Studies, D.E.L., Technology, B.C.S., and Alper, J. (2016). The Changing Landscape of Hydrocarbon Feedstocks for Chemical Production: Implications for Catalysis: Proceedings of a Workshop (National Academies Press).
- 4. Stangland, E.E. (2018). Shale Gas Implications for C2-C3 Olefin Production: Incumbent and Future Technology. Annual Review of Chemical and Biomolecular Engineering 9, 341-364. 10.1146/annurev-chembioeng-060817-084345.
- 5. Docherty, S.R., Rochlitz, L., Payard, P.-A., and Copéret, C. (2021). Heterogeneous alkane dehydrogenation catalysts investigated via a surface organometallic chemistry approach. Chemical Society Reviews *50*, 5806-5822. 10.1039/D0CS01424A.
- 6. Sattler, J.J.H.B., Ruiz-Martinez, J., Santillan-Jimenez, E., and Weckhuysen, B.M. (2014). Catalytic Dehydrogenation of Light Alkanes on Metals and Metal Oxides. Chemical Reviews *114*, 10613-10653. 10.1021/cr5002436.
- 7. Pretz, M., Fish, B., Luo, L., and Stears, B. (2017). Shaping the future of on-purpose propylene production. Hydrocarbon Processing *2017*.
- 8. Matthew T. Pretz, M.W.S. (2014) Catalytic Dehydrogenation Process. patent application PCT/US2014/060371.
- 9. Basile, A. (2013). Handbook of Membrane Reactors: Fundamental Materials Science, Design and Optimisation (Elsevier Science).
- 10. Ovalle-Encinia, O., and Lin, J.Y.S. (2022). Water-gas shift reaction in ceramic-carbonate dual-phase membrane reactor at high temperatures and pressures. Chemical Engineering Journal *448*, 137652. https://doi.org/10.1016/j.cej.2022.137652.
- 11. Morejudo, S.H., Zanón, R., Escolástico, S., Yuste-Tirados, I., Malerød-Fjeld, H., Vestre, P.K., Coors, W.G., Martínez, A., Norby, T., Serra, J.M., and Kjølseth, C. (2016). Direct conversion of

- methane to aromatics in a catalytic co-ionic membrane reactor. Science 353, 563-566. 10.1126/science.aag0274.
- 12. Chen, S., Chang, X., Sun, G., Zhang, T., Xu, Y., Wang, Y., Pei, C., and Gong, J. (2021). Propane dehydrogenation: catalyst development, new chemistry, and emerging technologies. Chemical Society Reviews *50*, 3315-3354. 10.1039/D0CS00814A.
- 13. Chaiyavech, P. (2002). Commericialization of the world's first oleflex unit. The Journal of the Royal Institute of Thailand 27,3.
- 14. Gartside, R.J. (2000) Catalytic hydrocarbon dehydrogenation system with prereaction. patent application US6392113B1.
- 15. Seo, S.-T., Won, W., Lee, K.S., Jung, C., and Lee, S. (2007). Repetitive control of CATOFIN process. Korean Journal of Chemical Engineering *24*, 921-926. 10.1007/s11814-007-0098-3.
- 16. See Table S10 in supplemental information.
- 17. Motagamwala, A.H., Almallahi, R., Wortman, J., Igenegbai, V.O., and Linic, S. (2021). Stable and selective catalysts for propane dehydrogenation operating at thermodynamic limit. Science *373*, 217-222. 10.1126/science.abg7894.
- 18. Pan, Y., Bhowmick, A., Wu, W., Zhang, Y., Diao, Y., Zheng, A., Zhang, C., Xie, R., Liu, Z., Meng, J., and Liu, D. (2021). Titanium Silicalite-1 Nanosheet-Supported Platinum for Non-oxidative Ethane Dehydrogenation. ACS Catalysis 11, 9970-9985. 10.1021/acscatal.1c02676.
- 19. del Campo, P., Martínez, C., and Corma, A. (2021). Activation and conversion of alkanes in the confined space of zeolite-type materials. Chemical Society Reviews *50*, 8511-8595. 10.1039/D0CS01459A.
- 20. Sun, Q., Wang, N., Fan, Q., Zeng, L., Mayoral, A., Miao, S., Yang, R., Jiang, Z., Zhou, W., and Zhang, J. (2020). Subnanometer bimetallic platinum–zinc clusters in zeolites for propane dehydrogenation. Angewandte Chemie 132, 19618-19627. https://doi.org/10.1002/ange.202003349.
- 21. Liu, L., Li, H., Zhou, H., Chu, S., Liu, L., Feng, Z., Qin, X., Qi, J., Hou, J., Wu, Q., et al. (2023). Rivet of cobalt in siliceous zeolite for catalytic ethane dehydrogenation. Chem *9*, 637-649. https://doi.org/10.1016/j.chempr.2022.10.026.
- 22. Qin, X., Wu, H., Wang, R., Wang, L., Liu, L., Li, H., Yang, B., Zhou, H., Liao, Z., and Xiao, F.-S. (2023). Domino catalysis for selective dehydrogenation of ethane with shifted thermodynamic equilibrium. Joule 7, 753-764. https://doi.org/10.1016/j.joule.2023.03.004.
- 23. Zhao, D., Tian, X., Doronkin, D.E., Han, S., Kondratenko, V.A., Grunwaldt, J.-D., Perechodjuk, A., Vuong, T.H., Rabeah, J., Eckelt, R., et al. (2021). In situ formation of ZnOx species for efficient propane dehydrogenation. Nature *599*, 234-238. 10.1038/s41586-021-03923-3.
- 24. Koros, W.J., and Lively, R.P. (2012). Water and beyond: expanding the spectrum of large-scale energy efficient separation processes. AIChE journal *58*, 2624. https://doi.org/10.1002/aic.13888.
- 25. Koros, W.J., and Zhang, C. (2017). Materials for next-generation molecularly selective synthetic membranes. Nature Materials *16*, 289-297. 10.1038/nmat4805.
- 26. Xu, L., Zhang, C., Rungta, M., Qiu, W., Liu, J., and Koros, W.J. (2014). Formation of defect-free 6FDA-DAM asymmetric hollow fiber membranes for gas separations. Journal of Membrane Science 459, 223-232. https://doi.org/10.1016/j.memsci.2014.02.023.
- 27. Bhuwania, N., Labreche, Y., Achoundong, C.S.K., Baltazar, J., Burgess, S.K., Karwa, S., Xu, L., Henderson, C.L., Williams, P.J., and Koros, W.J. (2014). Engineering substructure morphology of asymmetric carbon molecular sieve hollow fiber membranes. Carbon 76, 417-434. https://doi.org/10.1016/j.carbon.2014.05.008.
- 28. Medrano, J.A., Julián, I., García-García, F.R., Li, K., Herguido, J., and Menéndez, M. (2013). Two-Zone Fluidized Bed Reactor (TZFBR) with Palladium Membrane for Catalytic Propane Dehydrogenation: Experimental Performance Assessment. Industrial & Engineering Chemistry Research *52*, 3723-3731. 10.1021/ie303185p.

- 29. Rostami, R.B., Ghavipour, M., Di, Z., Wang, Y., and Behbahani, R.M. (2015). Study of coke deposition phenomena on the SAPO_34 catalyst and its effects on light olefin selectivity during the methanol to olefin reaction. RSC Advances *5*, 81965-81980. 10.1039/C5RA11288E.
- 30. Kim, S.-J., Liu, Y., Moore, J.S., Dixit, R.S., Pendergast, J.G., Jr., Sholl, D., Jones, C.W., and Nair, S. (2016). Thin Hydrogen-Selective SAPO-34 Zeolite Membranes for Enhanced Conversion and Selectivity in Propane Dehydrogenation Membrane Reactors. Chemistry of Materials *28*, 4397-4402. 10.1021/acs.chemmater.6b01458.
- 31. Dangwal, S., Ronte, A., Mahmodi, G., Zarrintaj, P., Lee, J.S., Saeb, M.R., Gappa-Fahlenkamp, H., and Kim, S.-J. (2021). Propane Dehydrogenation Reaction in a High-Pressure Zeolite Membrane Reactor. Energy & Fuels *35*, 19362-19373. 10.1021/acs.energyfuels.1c02473.
- 32. Kim, S.-J., Tan, S., Taborga Claure, M., Briones Gil, L., More, K.L., Liu, Y., Moore, J.S., Dixit, R.S., Pendergast, J.G., Jr., Sholl, D.S., et al. (2016). One-Step Synthesis of Zeolite Membranes Containing Catalytic Metal Nanoclusters. ACS Applied Materials & Interfaces 8, 24671-24681. 10.1021/acsami.6b06576.
- 33. Balakotaiah, V., and Ratnakar, R.R. (2022). Modular reactors with electrical resistance heating for hydrocarbon cracking and other endothermic reactions. AIChE Journal *68*, e17542. https://doi.org/10.1002/aic.17542.
- 34. Dong, Q., Yao, Y., Cheng, S., Alexopoulos, K., Gao, J., Srinivas, S., Wang, Y., Pei, Y., Zheng, C., Brozena, A.H., et al. (2022). Programmable heating and quenching for efficient thermochemical synthesis. Nature *605*, 470-476. 10.1038/s41586-022-04568-6.
- 35. Wismann, S.T., Engbæk, J.S., Vendelbo, S.B., Bendixen, F.B., Eriksen, W.L., Aasberg-Petersen, K., Frandsen, C., Chorkendorff, I., and Mortensen, P.M. (2019). Electrified methane reforming: A compact approach to greener industrial hydrogen production. Science *364*, 756-759. 10.1126/science.aaw8775.
- 36. Liu, L., Lopez-Haro, M., Lopes, C.W., Li, C., Concepcion, P., Simonelli, L., Calvino, J.J., and Corma, A. (2019). Regioselective generation and reactivity control of subnanometric platinum clusters in zeolites for high-temperature catalysis. Nature Materials *18*, 866-873. 10.1038/s41563-019-0412-6.
- 37. Liu, L., Lopez-Haro, M., Calvino, J.J., and Corma, A. (2021). Tutorial: structural characterization of isolated metal atoms and subnanometric metal clusters in zeolites. Nature Protocols *16*, 1871-1906. 10.1038/s41596-020-0366-9.
- 38. Clausi, D.T., and Koros, W.J. (2000). Formation of defect-free polyimide hollow fiber membranes for gas separations. Journal of Membrane Science *167*, 79-89. https://doi.org/10.1016/S0376-7388(99)00276-8.

Figure titles and legends:

Figure 1. CMS hollow fiber MR for alkane dehydrogenation.

- (A) Alkane is converted to alkene and H_2 over a M/zeolite catalyst. Metal clusters confined in siliceous zeolite activate alkane without deactivation. CMS membrane selectively separates H_2 from alkane/alkene hydrocarbons.
- (B)-(D) MR comprised of M/zeolite (i.e., Pt-Zn/S1) catalyst (B) and CMS hollow fiber membrane (C) achieved nearly 4-fold the thermodynamic equilibrium conversion and record-low deactivation rate (D) in PDH literature.
- (E) Conversion, yield, and selectivity of the CMS MR and PBR for PDH versus reaction time. Thermodynamic equilibrium conversion (section S1.5.4) was included for comparison.

(PBR conditions: reaction temperature=450°C, weight hourly space velocity (WHSV)=0.35 h⁻¹, 50% C₃H₈ balanced with argon (Ar); MR conditions: same as PBR, 100 mL min⁻¹ sweep gas flow, number of CMS hollow fibers=5; Digit numbers in (B)-(D) denote cited references from literature (Table S10)).

Figure 2. CMS MR component and performance for PDH.

- (A)-(C) Photo (A) and scanning electron microscopy (SEM) images (B) of CMS hollow fiber and SEM image of Pt-Zn/S1 catalyst (C).
- (D) Permeances and separation factors in CMS hollow fiber membranes.
- (E) Propane conversion and selectivity over Pt-Zn/S1 catalyst in the PBR and MR at different reaction temperatures.
- (F)-(I) Effects of (F) number of CMS hollow fibers, (G) WHSV, (H) propane partial pressure, and (I) sweep gas flow rate on propane conversion and propylene selectivity in the CMS MR.

(Basic testing conditions: sweep gas flow rate=100 mL min⁻¹, reaction temperature=450 °C, WHSV=1.73 h⁻¹ (50% C₃H₈/50% Ar), number of CMS fibers=5. Variable was purposely changed in (E)-(I) to study that variable effect. WHSV of 0.35 h⁻¹ was used in (F). The rest of variables were kept the same as basic testing conditions. Thermodynamic equilibrium conversions are included for comparison.)

Figure 3. CMS MR performance in EDH.

- (A) H₂ permeance and H₂/C₂H₆ separation factor of CMS hollow fiber membrane.
- (B) Ethane conversion and ethylene selectivity over Co/deAl-BEA catalyst in the PBR and MR at different reaction temperatures (PBR conditions: WHSV= 1.43 h⁻¹, 50% C₂H₆ balanced with Ar; MR conditions: same as PBR, and 100 mL min⁻¹ sweep gas flow, number of CMS hollow fibers=5).
- (C) Conversion, yield, and selectivity of the CMS MR and PBR for EDH versus reaction time (PBR conditions: reaction temperature=500°C, WHSV=0.29 h⁻¹, 50% C₂H₆ balanced with Ar; MR conditions: same as PBR, and 100 mL min⁻¹ sweep gas flow, number of CMS hollow fibers=5). (D)-(F) MR comprised of Co/deAl-BEA catalyst (D) and CMS hollow fiber membrane (E) achieved conversions above thermodynamic equilibrium and record-low deactivation rate (F) in EDH literature. Thermodynamic equilibrium conversions are included for comparison.

(Digit numbers in (D)-(F) denote cited references from literature (Table S11)).

Figure 4. Electrifiable CMS MR and plant process simulation for PDH.

- (A) Effect of power output on temperature of a Joule-heated CMS hollow fiber (60 mm in length). Photos were captured to indicate the appearances of CMS hollow fiber at different power output. (B) Simulated 2D axisymmetric temperature profile of the Joule-heated CMS MR. (Simulation conditions: MR loaded with Pt-Zn/S1 catalyst, 10 mL min⁻¹sweep gas flow rate, WHSV= 1.33 h⁻¹ (50% C₃H₈ balanced with Ar), number of CMS fiber =1).
- (C) Measured propane conversion and propylene selectivity in the Joule-heated CMS MR. Reaction temperature was indicated by an average temperature that was obtained from averaging the 2D axisymmetric temperature profiles (section S6.2). (Reaction conditions were identical to (B)).

(D) Flow chart for process simulation of PDH plant equipped with the Joule-heated CMS MR.

(E)-(F) TEA (E) and LCA (F) of the simulated CMS MR powered by different electricity sources (grid: electricity from the U.S. electrical grid; grid + H₂: process heat from electricity in the U.S. electrical grid and combustion of H₂ co-product formed from PDH; solar: renewable electricity from photovoltaics; wind: renewable electricity from wind power; nuclear: electricity from nuclear power; fossil: process heat from combustion of natural gas) and in comparison to the commercial Catofin and Oleflex processes.

Supplemental information:

Materials and Methods Supplementary Text Figures S1 to S29

Tables S1 to S23

S1. Materials and Methods

S1.1 Materials

Matrimid[®] 5218 polyimide was provided by Huntsman Corporation (Salt Lake City, UT). Vinyltrimethoxysilane (VTMS, 97%), N-Methyl-2-pyrrolidone (NMP, anhydrous, 99.5%), tetrahydrofuran (THF, anhydrous, 99.5%), ethanol (anhydrous, 99.5%) and hexane (mixture of isomers, anhydrous, 99%) were obtained from Sigma Aldrich (St. Louis, MO). Methanol (99.8% ACS, VWR Chemicals BDH[®]) and hexane (98.5% ACS, Millipore Sigma) were used for precursor hollow fiber solvent exchange. Platinum (II) chloride (PtCl₂) (99.5%, Beantown Chemical), zinc acetylacetonate hydrate (Zn(acac)₂·xH₂O) (96%, Alfa Aesar), ethylenediamine (>99.5%, Fluka Analytical), tetraethoxysilane (TEOS) (98%, Alfa Aesar), and tetrapropylammoniumhydroxide (TPAOH) (40wt% solution in water, Millipore Sigma), zeolite beta (BEA) (Si/Al ratio = 19, Alfa Aesar), nitric acid (70 vol%, Fisher Scientific), and cobalt (II) nitrate hexahydrate (Co(NO₃)₂·6H₂O) (99%, Acros Organics) were used for metal/zeolite catalyst synthesis. All chemicals were used as received. Deionized (DI) water was used in the experiment.

S1.2 Cobalt/dealuminated BEA catalyst for non-oxidative EDH

Dealuminated BEA (DeAl-BEA) was prepared by following the procedure reported by Harris et al¹. Typically, 1.00 g commercial BEA zeolite sample was mixed with 25 mL nitric acid (~70%) in a perfluoroalkoxy jar (Savillex) and heated to 80 °C in oil bath under 450 rpm stirring for 16 h. The solid was collected by centrifugation and washed with DI water until a pH of 7 was obtained prior to drying overnight at 70 °C. The incipient wetness impregnation method was used to prepare the DeAl-BEA supported cobalt (i.e., Co/DeAl-BEA) catalyst. In the synthesis, 0.15 g of cobalt (II) nitrate hexahydrate was dissolved in 0.50 g of DI water and then added dropwise to 1.00 g of DeAl-BEA and mixed with a polypropylene spatula to a uniform coloration on the evaporating basin. After drying in a fume hood for 16 h, the obtained solid was heated in a muffle furnace to 100 °C (1 °C min⁻¹) for 3 h, followed by ramping to 550 °C (1 °C min⁻¹) for 6 h under flowing air (Airgas, 800 cm³ min⁻¹). The sample was shaped into 180-425 μm particle size range using the same procedure as that of Pt-Zn/S1 catalyst.

S1.3 Membrane module preparation and separation performance tests

S1.3.1 Preparation of CMS hollow fiber membrane module

Stainless steel Swagelok® fittings and a "U"-shaped Quartz reactor were used for the membrane module construction. Epoxy (3MTM Scotch-WeldTM DP-100) was used as the sealing material. Swagelok® Ultra-Torr Tee was used on each side of the U-shape quartz tube. Remaining steps for the module construction followed similar procedures described in literature². Single-side length of the "U"-shaped membrane module is 27 cm and multiple CMS hollow fibers could be incorporated into the module. During membrane permeation and reaction tests, the epoxy-sealed module connections were kept outside the tubular furnace and exposed to ambient conditions. **Figure S2A** shows the schematics of the prepared membrane module.

S1.3.2 Membrane separation performance measurement

The separation performance of CMS hollow fiber membranes was evaluated in a reactor rig system, which is easily configured for membrane permeation, reaction, or membrane reactor tests when it

is connected to a membrane module (Figure S2A), a packed bed reactor module (Figure S2B) or a membrane reactor module (Figure S2C). The bottom part of the membrane module was placed inside a temperature-controlled furnace (National Electric Furnace FA120 type) where the temperature was controlled by a Watlow Controller (96 series). The module temperatures were measured using a K-type thermocouple touching the middle-bottom external surface of the "U"shaped quartz tube. In the membrane permeation test, the membrane module was first flushed with inert Ar gas flow at both shell and bore sides of the CMS hollow fibers overnight at ambient conditions to remove trapped air in the system. Afterwards, the module was heated to target temperature at a ramp rate of 0.0417 °C s⁻¹. A binary feed mixture (e.g., H₂/C₃H₈ at 1 bar) was introduced to replace the Ar flow in the hollow fiber shell side. All transfer lines in the reactor rig were maintained at temperatures greater than 100 °C by resistive heating to prevent any potential condensation. A gas chromatograph (GC, Agilent 6890) equipped with a packed column (HayeSep DB, 2 m in length, 2 mm ID x 1/8" OD, Silco HP) connected to a thermal conductivity detector (TCD) and a methylsiloxane capillary column (GS-GasPro, 50.0 m x 320 μm x 0.52 μm) connected to a flame ionization detector (FID) was used to separate and quantify the feed, retentate and permeate streams.

Permeability is a measure of membrane intrinsic productivity and is defined as partial pressure difference and membrane thickness normalized flux³. Because the separation layer thickness of asymmetric hollow fiber membranes usually cannot be unambiguously determined, permeance (P_i/l) is often used to describe the membrane productivity, which is defined as partial pressure difference (Δp_i) normalized flux (I_i)

$$\left(\frac{P_i}{l}\right) = \frac{J_i}{\Delta p_i} \tag{Eq. S1}$$

where P_i is the permeability of component i and l is membrane separation layer thickness. The units often used for permeability and permeance are Barrer and gas permeation unit (GPU), respectively.

$$1 \text{ Barrer } = 10^{-10} \frac{\text{cm}^3(\text{STP}) \cdot \text{cm}}{\text{cm}^2 \cdot \text{s} \cdot \text{cmHg}}$$
 (Eq. S2)

$$1 \text{ GPU } = 10^{-6} \frac{\text{cm}^3(\text{STP})}{\text{cm}^2 \cdot \text{s} \cdot \text{cmHg}}$$
 (Eq. S3)

Permselectivity is a measure of membrane separation efficiency. The ideal permselectivity (e.g., $\alpha_{A/B}$) of a membrane with negligible downstream pressure is defined as the ratio of permeabilities (i.e., P_A and P_B) or permeances (P_A/l and P_B/l) of components A and B in the separation tests.

$$\alpha_{A/B} = \frac{P_A}{P_B} = \frac{P_A/l}{P_B/l}$$
 (Eq. S4)

For a mixture feed, separation factor $(\alpha_{A/B})$ is often used to describe membrane separation efficiency for a mixture of A and B components,

$$\alpha_{A/B} = \frac{y_A/y_B}{x_A/x_B}$$
 (Eq. S5)

where y and x are molar composition at membrane permeate side and retentate side, respectively.

The temperature dependence of permeance follows an Arrhenius relationship⁴,

$$\left(\frac{P_i}{l}\right) = \left(\frac{P_{0i}}{l}\right) \exp\left(-\frac{E_{P,i}}{RT}\right) \tag{Eq. S6}$$

where P_{0i}/l is the pre-exponential factor and $E_{P,i}$ (kJ mol⁻¹) is the apparent activation energy for permeation.

S1.4 Alkane dehydrogenation tests

S1.4.1 Alkane dehydrogenation in a packed bed reactor

Non-oxidative dehydrogenation of alkane was performed over the catalyst (diluted with acid-washed quartz particles) in a packed bed reactor (PBR) shown in **Figure S2B** above. Prior to the reaction tests, the catalyst was pretreated in a H_2/N_2 (20 mL min⁻¹, H_2/N_2 =1:5, ultrapure, Air gas) mixture gas at 500 °C (0.0167 °C s⁻¹) for 3 h. After the temperature ramped to the target reaction temperature, the H_2/N_2 gas flow was switched to alkane (i.e., C_xH_{2x+2} , x = 3 for propane (C₃H₈) or x = 2 for ethane (C₂H₆), Research grade, Matheson) mixed with the Ar internal standard (ultrahigh purity, Airgas) to start the dehydrogenation reaction test.

The alkane conversion $(\chi_{C_xH_{2x+2}})$, alkene product selectivity $(S_{C_xH_{2x}})$ and yield $(Y_{C_xH_{2x}})$ were calculated by the following equations,

$$\chi_{C_x H_{2x+2}}(\%) = \frac{F_{C_x H_{2x+2}}^{in} - F_{C_x H_{2x+2}}^{out}}{F_{C_x H_{2x+2}}^{in}} \times 100\%$$
 (Eq. S7)

$$S_{C_x H_{2x}}(\%) = \frac{F_{C_x H_{2x}}}{F_{C_x H_{2x+2}}^{in} - F_{C_x H_{2x+2}}^{out}} \times 100\%$$
 (Eq. S8)

$$Y_{C_x H_{2x}}(\%) = \chi_{C_x H_{2x+2}} \times S_{C_x H_{2x}}$$
 (Eq. S9)

where $F_{C_xH_{2x+2}}^{in}$, $F_{C_xH_{2x+2}}^{out}$, and $F_{C_xH_{2x}}$ are the alkane flow rates at the inlet and outlet of the reactor, and alkene product flow rate at the reactor outlet, respectively. The dehydrogenation reaction in the PBR in the absence of catalyst was tested at the same conditions. The reaction due to gas phase chemistry was negligible at the studied reaction conditions.

S1.4.2 Alkane dehydrogenation in a CMS membrane reactor

The alkane conversion and alkene selectivity in membrane reactor were calculated using the following equations,

$$\chi_{C_x H_{2x+2}}(\%) = \frac{F_{C_x H_{2x+2}}^{in} - \left(F_{C_x H_{2x+2, shell}}^{out} + F_{C_x H_{2x+2, bore}}^{out}\right)}{F_{C_x H_{2x+2}}^{in}} \times 100\%$$
 (Eq. S10)

$$S_{C_x H_{2x}}(\%) = \frac{\left(F_{C_x H_{2x, shell}} + F_{C_x H_{2x, bore}}\right)}{F_{C_x H_{2x+2}}^{in} - \left(F_{C_x H_{2x+2, shell}}^{out} + F_{C_x H_{2x+2, bore}}^{out}\right)} \times 100\%$$
 (Eq. S11)

where $F_{C_xH_{2x+2,shell}}^{out}$, $F_{C_xH_{2x+2,bore}}^{out}$, $F_{C_xH_{2x,shell}}$, and $F_{C_xH_{2x,bore}}$ are the alkane flow rates at the outlet of the shell and bore sides as well as alkene product flow rates at the outlet of the shell and bore sides of the reactor, respectively. The alkene yield in the MR was calculated using Eq. S9. The dehydrogenation reaction in the MR in the absence of catalyst was tested at the same conditions. The reaction due to gas phase reactions was negligible at the studied reaction conditions.

S1.4.3 Catalyst stability analysis in alkane dehydrogenation

To quantify the stability (or deactivation behavior) of the catalyst in either PBR or MR conditions, the first-order deactivation kinetics was assumed to evaluate the deactivation coefficient of the catalyst in alkane dehydrogenation. This method has been used to analyze the catalytic reactions on supported metal catalysts in the past⁵. The equation for calculating the deactivation coefficient (k_d) has been reported previously⁶, and is shown below,

$$k_d = \frac{ln\left(\frac{1-\chi_{C_X H_{2X+2}}}{\chi_{C_X H_{2X+2}}}\right) - ln\left(\frac{1-\chi_{C_X H_{2X+2}}^0}{\chi_{C_X H_{2X+2}}^0}\right)}{t}$$
(Eq. S12)

where $\chi^o_{C_x H_{2x+2}}$ is the initial (i.e., the moment that reaction reached steady state) alkane conversion and $\chi_{C_x H_{2x+2}}$ is the final alkane conversion at time-on-stream (TOS) tests for a period of t (h).

S1.4.4 Equilibrium conversion of alkane dehydrogenation

We calculated thermodynamic equilibrium conversion for alkane dehydrogenation reactions (i.e., $C_3H_8 = C_3H_6 + H_2$ and $C_2H_6 = C_2H_4 + H_2$) at the experimental testing conditions using the van't Hoff equation,

$$\frac{dlnK_{eq}}{dT} = \frac{\Delta H_r}{RT^2} \tag{Eq. S13}$$

where K_{eq} is the equilibrium constant, T is the reaction temperature (K), ΔH_r is the enthalpy of reaction (kJ·mol⁻¹), and R is the gas constant (J·mol⁻¹·K⁻¹), respectively. ΔH_r depends on the reaction temperature as shown by the equations below,

$$\Delta H_r(T) = \Delta H_r^0 + \int_{T_0}^T \Delta C_{r,p} dT$$
 (Eq. S14)

$$C_p = A + BT + CT^2 + DT^3$$
 (Eq. S15)

$$\Delta C_{r,p} = \Delta A + \Delta BT + \Delta CT^2 + \Delta DT^3$$
 (Eq. S16)

in which ΔH_r^0 is the enthalpy of reaction at STP condition, T_0 is the ambient temperature (25 °C), C_p is the constant pressure heat capacity (J·mol⁻¹·K⁻¹), A, B, C, and D are the coefficients in the calculation equation for C_p at different temperatures, and $\Delta C_{r,p}$ is the change of heat capacity due to a reaction. Substituting Eq. S16 and Eq. S14 into Eq. S13, we have,

$$K_{eq}(T) = K_{eq}^{0} \exp \left\{ \frac{\Delta H_{r}^{0} - (\Delta A \cdot T_{0} + \frac{\Delta B}{2} \cdot T_{0}^{2} + \frac{\Delta C}{3} \cdot T_{0}^{3} + \frac{\Delta D}{4} \cdot T_{0}^{4})}{R} \cdot \left(\frac{1}{T_{0}} - \frac{1}{T} \right) + \frac{\Delta A \cdot \ln \left(\frac{T}{T_{0}} \right) + \frac{\Delta B}{2} \cdot (T - T_{0}) + \frac{\Delta C}{6} \cdot (T^{2} - T_{0}^{2}) + \frac{\Delta D}{12} \cdot (T^{3} - T_{0}^{3})}{R} \right\}$$
 (Eq. S17)

where K_{eq}^0 is the equilibrium constant at STP condition. The calculation for K_{eq}^0 is shown by the Eq. S18-S21 below.

$$K_{eq}^0 = \exp\left(-\frac{\Delta G_r^0}{RT_0}\right) \tag{Eq. S18}$$

$$\Delta G_r^0 = \Delta H_r^0 - T_0 \Delta S_r^0 \tag{Eq. S19}$$

$$\Delta H_r^0 = \sum_i \nu_i \, \Delta H_{i,f}^0 \tag{Eq. S20}$$

$$\Delta S_r^0 = \sum_i \nu_i \, S_{i,f}^0 \tag{Eq. S21}$$

where ΔG_r^0 is the standard Gibbs free energy of reaction, T_0 is standard temperature (298.15 K), ΔS_r^0 is the standard entropy of reaction, v_i is the stoichiometric coefficient of species i. $\Delta H_{i,f}^0$ and $S_{i,f}^0$ stands for standard enthalpy of formation and standard entropy of formation of compound i, respectively. **Table S3** lists the corresponding thermodynamic data used for the equilibrium conversion calculations for both ethane and propane dehydration reactions⁷.

The reaction equilibrium constant (K_{eq}) at a fixed reaction equilibrium condition can also be expressed from the reaction compositions,

$$K_{eq} = \prod_{i} \left(\frac{p_{i}}{p^{0}}\right)^{\nu_{i}} = \frac{a\chi_{C_{X}H_{2X+2}}^{eqbm}}{\left(1 - \chi_{C_{X}H_{2X+2}}^{eqbm}\right)\left(1 + a\chi_{C_{X}H_{2X+2}}^{eqbm}\right)}$$
(Eq. S22)

where p_i is the partial pressure of gas species i, p^0 is the standard pressure (1 atm), a is the alkane fraction in the feed stream (balanced by Ar internal standard), $\chi^{eqbm}_{C_xH_{2x+2}}$ is the thermodynamic equilibrium conversion. Then, $\chi^{eqbm}_{C_xH_{2x+2}}$ can be calculated using the following equation,

$$\chi_{C_x H_{2x+2}}^{eqbm} = \frac{\kappa_{eq}(a-1) + \sqrt{\left(\kappa_{eq}(1-a)\right)^2 + 4a\left(1 + \kappa_{eq}\right)\kappa_{eq}}}{2a(1 + \kappa_{eq})} \times 100\%$$
 (Eq. S23a)

H₂ removal ratio (y) is introduced to calculate the thermodynamic conversion with H₂ elimination from the shell side of the MR:

$$\chi^{eqbm}_{C_x H_{2x+2}} = \frac{\kappa_{eq}(a(1-y)-1) + \sqrt{\left(\kappa_{eq}(1-a(1-y))\right)^2 + 4a(1-y)(1+\kappa_{eq})\kappa_{eq}}}{2a(1+\kappa_{eq})(1-y)} \times 100\%$$
 (Eq. S23b)

When y equals 0, it is equilibrium conversion in PBR. Take T=450 °C, 50 kPa C₃H₈/50 kPa Ar (a=0.5) as an example, when y=0, $\chi_{C_3H_8}^{eqbm}$ =12.4%; y=20%, $\chi_{C_3H_8}^{eqbm}$ =14.1%; y=40%, $\chi_{C_3H_8}^{eqbm}$ =16.0%; y=60%, $\chi_{C_3H_8}^{eqbm}$ =19.0%; y=80%, $\chi_{C_3H_8}^{eqbm}$ =25.5%; y=90%, $\chi_{C_3H_8}^{eqbm}$ =33.7%; y=95%, $\chi_{C_3H_8}^{eqbm}$ =43.7%; y=99%, $\chi_{C_3H_8}^{eqbm}$ =70.4%, respectively.

The conversion in alkane dehydrogenation in the MR condition was compared to the equilibrium conversion by calculating the conversion enhancement using,

$$Conversion/Eqbm. Conversion = \frac{\chi_{C_x H_{2x+2}}}{\chi_{C_x H_{2x+2}}^{eqbm}} \times 100\%$$
 (Eq. S24)

S2. Catalyst and membrane characterization

S2.1 Characterization techniques

Morphologies of catalyst and hollow fiber membrane materials were examined by a XEIA3 TESCAN scanning electron microscope (SEM). The morphologies of catalysts were further measured using a transmission electron microscope (JEM 2100 LaB6). XRD patterns of the

catalysts were recorded using a Bruker D8 Advance Lynx Powder Diffractometer (LynxEye PSD detector, sealed tube, Cu Kα radiation with Ni β-filter). N₂ adsorption/desorption isotherms were measured using an Autosorb-iQ analyzer (Quantachrome Instruments) at 77 K. The samples were outgassed at 573 K for 8 h at 1 mmHg pressure prior to measurements. Elemental compositions of the catalysts were determined by an inductively coupled plasma-optical emission spectrometry (ICP-OES).

S2.2 Catalyst characterization data

S2.2.1 Chemical composition

The chemical compositions of Pt-Zn/S1 and Co/DeAl-BEA catalysts are summarized in **Table S4**. The nominal Pt and Zn concentrations in the Pt-Zn/S1 catalyst are 0.90wt% and 1.40wt%, respectively. The actual Pt and Zn concentrations are lower than the nominal loadings, which could be caused by the extensive washing during sample preparation. The actual Co concentration (3.04wt%) is similar to the nominal loading (3.00 wt%) in the preparation of Co/DeAl-BEA catalyst.

S2.2.2 Morphological, crystalline and textural properties of Pt-Zn/S1 catalyst

The morphology of Pt-Zn/S1 catalyst particles is shown by the SEM images in Figure S3. The assynthesized sample (Figure S3A-B) primarily contains coffin-shaped particles with sizes in the range of 3-6 µm. It also consists of a small portion of irregular shaped particles, and some of them form aggregates. After the pre-reduction treatment, the sample keeps the similar morphology to the as-synthesized one except that the number of irregular shaped particles increased (Figure S3C-D). The increase in irregular shaped particles could be caused by the transformation of organics in the as-synthesized catalysts into carbonaceous materials due to the reductive pretreatment atmosphere. The pre-treated Pt-Zn/S1 sample was also examined by the TEM observations. Similar to results shown by the SEM images, the sample contains non-uniform particle sizes and morphologies (Figure S4A). A closer TEM examination on the particles shows that Pt-Zn clusters exist in the regular and irregular shaped particles (Figure S4B). The Pt-Zn clusters are quite uniform and small, with an average size of ~1.17nm.

Figure S5A shows XRD patterns of the as-synthesized and pre-reduced Pt-Zn/S1 catalysts. The samples show the characteristic signature reflections of highly crystalline MFI diffraction patterns. The prereduction treatment neither destroyed the MFI structure nor caused formation of new crystalline phases. No detectable peaks can be assigned to the Pt or ZnO materials, demonstrating that Pt and Zn are highly dispersed in the silicalite-1 support. N₂ adsorption/desorption isotherm (**Fig. S5B**) was used to reveal the textural property of the pre-reduced sample Pt-Zn/S1. The Brunauer-Emmett-Teller (BET) surface area, total pore volume and micropore volume of this sample are summarized in **Table S4** above.

S2.2.3 Morphological, crystalline and textural properties of Co/DeAl-BEA catalyst

Morphologies of the as-synthesized Co/DeAl-BEA catalyst are shown by the SEM and TEM images in **Figure S6.** The sample contains nearly spherical particles with sizes ranging from 0.2 to $1.0 \, \mu m$ (**Figure S6A-C**). The presence of Co species in the sample was confirmed by the TEM image in **Figure S6D**, showing a good dispersion on the support with sizes in the nanometer range.

To test the influence of dealumination and incipient impregnation methodology on zeolite support, XRD patterns and N₂ adsorption-desorption isotherms were measured on parent BEA, dealuminated BEA (DeAl-BEA), and Co/DeAl-BEA samples. As shown in **Figure S7A**, the characteristic diffraction peaks at 7.6° and 22.6°, corresponding to (101) and (302) planes of BEA topology⁸ present in all XRD patterns, indicating the preservation of zeolitic structure during the acid treating and metal loading processes. It is worth noting that the (302) diffraction peak of dealuminated Beta changes from 22.7° to 22.82° compared to the parent H-Beta, and shifts back to 22.6° for Co/DeAl-BEA. This back-and-forth behavior indicates the lattice shrinkage and expansion^{9,10} due to silanol nest formation and condensation, which play critical roles in anchoring highly dispersed metal species on zeolite support. And the absence of cobalt oxide peaks in the Co/BEA sample's XRD pattern also implies the formation of small cobalt species. N₂ isotherms (**Figure S7B** and **Table S4**) also confirm the consistent surface area and pore structure for all BEA-based samples.

S2.3 Morphologies of precursor and CMS hollow fiber membranes

Morphology of precursor and CMS hollow fiber membranes was characterized by SEM. The precursor hollow fiber had an outer diameter $\sim\!365~\mu m$ with a highly porous substructure. After pyrolysis, the CMS hollow fiber showed reduced outer diameter $\sim\!315~\mu m$ with a dense separation layer $\sim\!4.5~\mu m$ on top of a porous substrate.

S3. Microkinetic rate equation for PDH over Pt-Zn/S1 catalyst

S3.1 Rate equation derivation

Langmuir-Hinshelwood (L-H) mechanism was proposed for propane activation in PDH over the Pt-Zn/S1 catalyst. This mechanism has been applied to the Pt-based catalysts for PDH in literature 11-14. **Scheme S1** shows the elementary reaction steps in the L-H mechanism. The reaction starts from dissociative adsorption of propane on the active site (*) of the catalyst, producing C₃H₇* and H* species (Step 1). Activated C₃H₇* species undergoes a surface dehydrogenation reaction to form C₃H₆* and H* species (Step 2). Then C₃H₆* desorbs from the active site to produce propylene and release the active site (*) (Step 3). The adsorbed hydrogen species desorbs to produce hydrogen gas co-product (Step 4) and release the active sites. The propane activation is assumed to be the rate limiting step (RLS) in the scheme. Both forward and backward reactions in Step 1 is considered in the rate equation.

$$C_3H_8 + 2 * \stackrel{K_1}{\leftrightarrow} C_3H_7^* + H^*$$
 (Step 1, RLS)

$$C_3H_7^* + * \stackrel{K_2}{\leftrightarrow} C_3H_6^* + H^*$$
 (Step 2)

$$C_3H_6^* \stackrel{K_3}{\leftrightarrow} C_3H_6 + *$$
 (Step 3)

$$2H^* \stackrel{K_4}{\leftrightarrow} H_2 + 2 *$$
 (Step 4)

Scheme S1. Elementary steps in Langmuir-Hinshelwood reaction mechanism proposed for propane activation on Pt-Zn/S1 catalyst in PDH.

On the basis of Step (1) in **Scheme S1**, the C_3H_8 reaction rate $(r_{C_3H_8})$ is,

$$r_{C_3H_8} = r_1 = N(k_1^+ p_{C_2H_8} \theta_*^2 - k_1^- \theta_{C_2H_7} \theta_H)$$
 (Eq. S25)

where N is the quantity of catalyst tested, k_1^+ is the rate constant of forward reaction, $p_{C_3H_8}$ is the partial pressure of propane in the feed, θ_* is the fraction of free active sites, k_1^- is the rate constant of backward reaction, $\theta_{C_3H_7}$ is the fraction of active sites occupied by C_3H_7 species, and θ_H is the fraction of active sites occupied by H species, respectively. The equilibrium constant (K_1) is defined by $K_1 = k_1^+/k_1^-$ in the reaction step (1). When quasi-equilibrium approximation is applied to Steps (2)-(4) in Scheme 1, as shown in Eqs. S26-28 in sequence, we can obtain expressions for $\theta_{C_3H_7}$, $\theta_{C_3H_6}$ (i.e., fraction of active sites occupied by C_3H_6 species), and θ_H , accordingly. In these equations, k_2^+ and k_2^- , k_3^+ and k_3^- , and k_4^+ and k_4^- , are the forward and backward rate constants for Steps (2)-(4), respectively. Similarly, K_2 , K_3 , and K_4 are defined by the ratios of k_2^+/k_2^- , k_3^+/k_3^- , and k_4^+/k_4^- in these reaction steps. $p_{C_3H_6}$ and p_{H_2} are partial pressures of propylene and hydrogen in the reaction.

$$r_2 = k_2^+ \theta_{C_3H_7} \theta_* - k_2^- \theta_{C_3H_6} \theta_H \approx 0$$
 (Eq. S26)

$$r_3 = k_3^+ \theta_{C_3H_6} - k_3^- p_{C_3H_6} \theta_* \approx 0$$
 (Eq. S27)

$$r_4 = k_4^+ \theta_H^2 - k_4^- p_{H_2} \theta_*^2 \approx 0$$
 (Eq. S28)

From these equations, the expressions for $\theta_{C_3H_7}$, $\theta_{C_3H_6}$, and θ_H are,

$$\theta_{C_3H_6} = \frac{p_{C_3H_6}\theta_*}{K_3}$$
 (Eq. S29)

$$\theta_{\rm H} = \frac{\sqrt{p_{\rm H_2}} \, \theta_*}{\sqrt{K_4}} \tag{Eq. S30}$$

$$\theta_{C_3H_7} = \frac{p_{C_3H_6}\sqrt{p_{H_2}}}{K_2K_3\sqrt{K_4}}\theta_*$$
 (Eq. S31)

From the site balance equation (i.e., $\theta_* + \theta_{C_3H_7} + \theta_{C_3H_6} + \theta_H = 1$) of active sites in the catalyst, we solve for the expression for θ_* ,

$$\theta^* = \frac{1}{1 + \frac{p_{C_3H_6}}{\kappa_3} + \frac{\sqrt{p_{H_2}}}{\sqrt{\kappa_4}} + \frac{p_{C_3H_6}\sqrt{p_{H_2}}}{\kappa_2\kappa_3\sqrt{\kappa_4}}}$$
(Eq. S32)

After substituting $\theta_{C_3H_7}$, θ_H and θ^* into Eq. S25, the rate equation for C_3H_8 consumption is,

$$r_{C_3H_8} = \frac{N(k_1^{\dagger}p_{C_3H_8} - \frac{p_{C_3H_6}p_{H_2}}{K})}{\left(1 + \frac{p_{C_3H_6}}{K_3} + \frac{\sqrt{p_{H_2}}}{\sqrt{K_4}} + \frac{p_{C_3H_6}\sqrt{p_{H_2}}}{K_2K_3\sqrt{K_4}}\right)^2}$$
(Eq. S33)

in which K is defined as, $K = \frac{K_2 K_3 K_4}{k_1^-}$.

S3.2 Kinetics measurements and rate equation determination

S3.2.1 Kinetics data measurement

The experimental setup described for catalysis tests in PBR was used for collecting kinetics data for rate equation determination. In the experiment, catalyst samples (0.005 g-0.012 g) diluted with acid-washed quartz particles (0.088g-0.095g, 180-425 µm size range, European Commission) were treated in 5%H₂/N₂ gas flow (20 mL min⁻¹, ultrapure, Airgas) at 500 °C (2 °C min⁻¹) for 3 h prior to cooling in Ar flow to the reaction temperature. Steady-state propane dehydrogenation or propylene hydrogenation reactions were carried out under atmospheric pressure, in a temperature range of 363-708 K, and under conditions of differential conversion (<4.0%). Ar was used as the internal standard. **Table S5** summarizes the experiments conducted in the kinetics study.

S3.2.2 Determination of kinetic parameters in rate equation

To determine k_1^+ in Eq. S33, we firstly measured the reaction rate (i.e., propane consumption rate) as function of propane pressure at different temperatures (Exp. 1 in **Table S5** and **Figure S9A**). The reaction rate increased with increasing propane pressure and reaction temperature. In the absence of hydrogen and propylene, Eq. S33 can be simplified into,

$$\frac{r_{C_3H_8}}{N} = k_1^+ p_{C_3H_8}$$
 (Eq. S34)

 k_1^+ is the slope of the plot of $\frac{r_{C_3H_8}}{N}$ versus $p_{C_3H_8}$. To further determine other kinetics parameters, co-feeding of the reaction product into the propane stream was conducted. **Figure S9B** shows the reaction rate as a function of H_2 partial pressure in the presence of 50 kPa C_3H_8 feed. Although higher temperature led to a faster reaction rate, the presence of H_2 co-feed caused the drop in the reaction rate. For this experiment (Exp. 2 in **Table S5**), the rate equation is linearized into,

$$\sqrt{\frac{Np_{C_3H_8}}{r_{C_3H_8}}} = \frac{1}{\sqrt{k_1^+}} + \frac{1 + \sqrt{p_{H_2}}}{\sqrt{k_1^+ K_4}}$$
 (Eq. S35)

in which the intercept and slope are $\frac{1}{\sqrt{k_1^+}}$ and $\frac{1}{\sqrt{k_1^+ K_4}}$, respectively. **Figure S9C** shows the linear plot

of kinetics data collected in the Exp. 2 according to the Eq. S35. The k_1^+ values determined from this experiment is comparable to that of the Exp. 1. The adsorption equilibrium constant (K_4) was determined from the slope of **Figure S9C** and the average k_1^+ values from Exp. 1 and Exp. 2. **Table S6** summarizes the values of k_1^+ and K_4 obtained from these two experiments.

Exp. 3 in **Table S5** was conducted to determine K_3 in the rate equation. At a fixed propylene partial pressure, the correlation between the reaction rate and partial pressure of propane $(p_{C_3H_8})$ is expressed by Eq. S36. The linear plot of $\frac{r_{C_3H_8}}{N}$ versus the partial pressure of $p_{C_3H_8}$ gives the slope of $\frac{k_1^+}{\left(1+\frac{p_{C_3H_6}}{K_2}\right)^2}$. Since k_1^+ has been determined from Exps. 1 and 2, the desorption equilibrium

constant of propylene from the catalyst (K_3) can be calculated accordingly. **Figure S10A** presents the reaction rate linearly increases with the partial pressure of propane and temperature. Since the presence of propylene suppresses propane conversion, slightly higher temperatures were used in Exp. 3 than those in Exps. 1 and 2. The k_1^+ values at these higher temperatures were calculated using the Arrhenius equation that was generated from the fitting of the rate constant data (details in Section S3.2.3 below) in **Table S5**. The calculated values k_1^+ and K_3 in these testing temperatures are summarized in **Table S7**.

$$\frac{\mathbf{r}_{\mathsf{C_3H_8}}}{\mathsf{N}} = \frac{\mathbf{k}_1^{\dagger} p_{\mathsf{C_3H_8}}}{\left(1 + \frac{p_{\mathsf{C_3H_6}}}{\mathsf{K_3}}\right)^2} \tag{Eq. S36}$$

Up to this point, the remaining parameters of Eq. S33 are k_1^- (rate constant of backward reaction in Step (1)) and K_2 (adsorption equilibrium constant of Step (2)). In order to determine them, we carried out the backward reaction (i.e., hydrogenation of propylene) tests, conditions shown in Exp. 4 in **Table S5**. By fixing the hydrogen pressure, the hydrogenation rate (i.e., propane formation rate) as a function of partial pressure of propylene was measured. **Figure S10B** shows the reaction rate increases with partial pressure of propylene and reaction temperature. The linearized rate equation for this set of experimental tests is shown below,

$$\sqrt{\frac{Np_{C_3H_6}p_{H_2}}{r_{C_3H_8}}} = \sqrt{K} \left(1 + \frac{\sqrt{p_{H_2}}}{\sqrt{K_4}} \right) + \sqrt{K} \left(\frac{1}{K_3} + \frac{\sqrt{p_{H_2}}}{K_2K_3\sqrt{K_4}} \right) p_{C_3H_6}$$
 (Eq. S37)

where the intercept is $\sqrt{K}\left(1+\frac{\sqrt{p_{H_2}}}{\sqrt{K_4}}\right)$ and the slope is $\sqrt{K}\left(\frac{1}{K_3}+\frac{\sqrt{p_{H_2}}}{K_2K_3\sqrt{K_4}}\right)$. The division of the slope by the intercept cancels out the \sqrt{K} term. Since K_3 and K_4 have been measured from the previous experiments, the only unknown quantity is K_2 and is determined from this ratio. It is known $K=\frac{K_2K_3K_4}{k_1^-}$, while K_3 can be determined from the intercept of the plot. Therefore, the last parameter, K_1^- , can be measured. The linearized plots for data in **Figure S10B** are included in **Figure S10C**. The measured K_1^- and K_2 values are summarized in **Table S8**. Due to the high reactivity of propylene, much lower temperatures in Exp. 4 were used to control the differential reaction conditions. The values of K_3 and K_4 (**Table S8**) were extrapolated to this low temperature range by using the Van's Hoff Equations obtained from the fitting of the K_3 and K_4 measured from the Exps. 2 and 3.

S3.2.3 Determination of activation energy and adsorption energy equations

The rate constant (k₁⁺ or k₁⁻) for PDH over the Pt-Zn/S1 catalyst at different temperatures can be used to calculate the activation energy and pre-exponential for propane consumption in the forward reaction or propylene consumption in the backward reaction. By plotting the natural logarithm of rate constants versus the inverse temperature (Eq. S38, **Figure S11A** and **Figure S11C**), these quantities were calculated and summarized in **Table S9**. Similarly, the adsorption energy and pre-exponential can be obtained by plotting the natural logarithm of adsorption constant versus the inverse temperature (Eq. S39, **Figure S11A-C** and **Table S9**). From these quantities, by using the Eq. S38 and Eq. S39, the rate equation developed for PDH in this study can be broadly applied to different reaction conditions, which forms the basis for the process simulation in Section S5 below.

$$k=k_0e^{\left(-\frac{E_a}{RT}\right)}$$
 (Eq. S38)

$$K=K_0e^{\left(-\frac{\Delta H}{RT}\right)}$$
 (Eq. S39)

S4. Performance comparison between CMS membrane reactor and literature data

Table S10-11 summarized the experimental studies of non-oxidative propane dehydrogenation membrane reactors 15-40 and non-oxidative ethane dehydrogenation membrane reactors 41-49.

S5. Regeneration of Pt-Zn/S1 and Co/DeAl-BEA catalysts

After the long-term (i.e., 112 h) test of PDH over the Pt-Zn/S1 catalyst in the MR, we regenerated the catalyst by exposing the spent catalyst to a hydrogen gas flow for a period of time. Specifically, the spent catalyst was taken out from the MR and loaded into a PBR. After flushing the reactor rig system with H₂ gas flow (Ultra high purity, Airgas, 20 mL min⁻¹) at ambient temperature for 0.5 h, the catalyst temperature was ramped (2.5 °C min⁻¹ ramp rate) to 500°C and kept at 500°C for 1 h. We then measured the propane reaction rates over spent and regenerated catalysts and compared these rates to that of the fresh Pt-Zn/S1 catalyst. **Figure S12A** shows that the regenerated Pt-Zn/S1 has recovered the catalytic activity from the spent one, and the rate is comparable to that of the fresh Pt-Zn/S1 catalyst.

Similarly, we studied the regeneration of spent Co/DeAl-BEA catalyst after the long-term (i.e., 110 h) EDH test over this catalyst in the MR. The regeneration was done by transferring the spent catalyst from the MR into a crucible. The catalyst in the crucible was heated in a muffle furnace to 100 °C (1 °C min⁻¹) for 3 h, followed by ramping to 550 °C (1 °C min⁻¹) for 6 h under flowing air (Airgas, 800 cm³ min⁻¹). The ethane reaction rates over the fresh, spent and regenerated Co/DeAl-BEA catalysts were measured under the same reaction conditions. **Figure S12B** shows that the catalyst activity is recovered from this regeneration operation, comparable to the activity of the fresh Co/DeAl-BEA catalyst.

S6. Computational fluid dynamic modeling in electrified membrane reactor

Model setup

The temperature profile of the reactor with process heat from Joule heating of the CMS hollow fiber was modelled using Comsol 6.0 in a 2D-axisymmetric geometry (**Figure S14**) with fully coupled equations for fluid motion, energy transport, and mass transport. The following sections briefly describe the implementation of this modeling.

- (1) Meshing: For fluid domains, a triangular mesh with a maximum resolution of 0.05 mm was employed, with improved resolution in the boundary layer domain. A quadratic mesh was used for the CMS membrane and reactor wall.
- (2) Fluid motion: The fluid motion is at laminar in both permeate and retentate sides with the Reynolds number never exceeding 850, well below the transition towards the turbulent regime beginning at 2100. Fluid motion was implemented as following,

$$\frac{\rho}{\epsilon_{p}}(u \bullet \nabla) \frac{u}{\epsilon_{p}} = \nabla \bullet \left[-pI + \frac{\mu}{\epsilon_{p}} \left(\nabla u + (\nabla u)^{T} \right) - \frac{2}{3} \frac{\mu}{\epsilon_{p}} (\nabla \bullet u)I \right] - \left(\mu \kappa^{-1} + \beta \rho |u| + \frac{\rho \nabla \bullet u}{\epsilon_{p}^{2}} \right) u$$
 (Eq. S40)

where ρ is the density, \mathcal{E}_p is the porosity of the material, u is the velocity, ∇ is vector differential operator, p is the pressure, u is the velocity, I is the identity matrix, μ is the dynamic viscosity of the fluid, T is the transpose of the matrix, κ is the permeability of the porous material, and β is momentum correction factor. The dynamic viscosity of the fluid mixture μ_{mix} follows the Darcian flow model and can be expressed as following,

$$\mu_{mix} = \sum_{i=1}^{N} \frac{x_i \mu_i}{\sum_i x_i \Phi_{ij}}$$
 (Eq. S41)

where x_i is molar fraction of species i, μ_i is species viscosity, and Φ_{ij} is a dimensionless quantity defined by Eq. S42.

$$\Phi_{ij} = \frac{1}{\sqrt{8}} \left(1 + \frac{M_i}{M_j} \right)^{-\frac{1}{2}} \left[1 + \left(\frac{u_i}{u_j} \right)^{\frac{1}{2}} \left(\frac{M_j}{M_i} \right)^{\frac{1}{4}} \right]^2 \qquad (i \neq j)$$
 (Eq. S42)

In this equation, i and j are fluid specie ($i \neq j$). M is the molecular weight of each species.

The boundary conditions for the fluid dynamics are specified as volumetric flow rate and pressure at the inlets of shell and bore sides of the reactor. The viscosity of the gas mixture follows Davidson's calculation⁵⁰. The density of the gas mixture is assumed to follow the ideal gas behavior.

(3) Mass transport: Mass transport was implemented as Eq. S43, where J_i is mass flux vector and c_i is the concentration of species i, and r_i is the rate expression for consumption of reactant or formation of product.

$$\nabla \bullet J_i + u * \nabla c_i = r_i \tag{Eq. S43}$$

The mass flux is defined as,

$$J_i = -D_{e,i} \nabla c_i \tag{Eq. S44}$$

where $D_{e,i}$ is the effective diffusion coefficient.

The rate expression is obtained by adopting the derived kinetic model listed in Eq. S33 and kinetic parameters listed in **Table S9**.

(4) Energy transport: Energy was implemented according to Eq. S45, where C_p is the heat capacity, Q_j is the heat source of joule heating fiber, Q_r is the heat source of reaction, k_{eff} is the effective thermal conductivity coefficient.

$$\rho_f C_{p,f} u \bullet \nabla T + \nabla \bullet (-k_{eff} \nabla T) = Q_j + Q_r$$
 (Eq. S45)

The effective thermal conductivity coefficient of packed bed in the study was described by,

$$k_{eff} = \mathcal{E}_p k_f + (1 - \mathcal{E}_p) k_s \tag{Eq. S46}$$

where, k_f is the thermal conductivity of the gas, and k_s being the thermal conductivity of the catalyst. The thermal conductivity of the gas mixture can be evaluated from,

$$k_f = \sum_{i=1}^{N} \frac{x_i k_i}{\sum_j x_j \Phi_{ij}}$$
 (Eq. S47)

The temperature profile of the outer surface of the quartz tube was measured experimentally and added into the model. The external heat loss only includes convective heat transfer at the outer surface of the quartz tube. Fixed temperature was given at inlets.

The CMS hollow fiber was assumed to provide uniform power output, which was calculated by Eq. S48, in which V is the voltage supplied and I is the current. The resistance of the copper

connections is assumed to be negligible. The heat source of the reaction can be expressed by Eq. S49, where r is the rate of the PDH reaction, and ΔH_r is the heat of the PDH reaction.

$$Q_i = VI (Eq. S48)$$

$$Q_r = r\Delta H_r \tag{Eq. S49}$$

<u>Simulation result evaluation and catalyst bed temperature</u>

To evaluate the simulation result, the experimental measured axial temperature profile along 1.08 mm radial position indicated in **Figure S14** was compared with the simulated 2D axisymmetric temperature profile under same reaction conditions. The simulated 1D axial temperature profile at 1.08 mm radial position (**Figure S15**) was extracted from 2D temperature profile and compared with experiment results. The simulated result shows excellent consistency with the experimental result. As the radial direction has significant temperature difference, the average catalyst bed temperature was obtained from the simulated 2D temperature profile and included in **Figure 4B**.

S7. Process modeling, technoeconomic and life cycle analyses for PDH

Technoeconomic (TEA) and life cycle analyses (LCA) were performed to evaluate the alkane dehydrogenation processes in the CMS membrane reactor. The PDH process was selected as case study and compared with the current state-of-art, Catofin and Oleflex processes. All the processes have been modeled in Aspen Plus v.11 using NRTL as thermodynamic package. Section S7.1 summarizes Catofin and Oleflex processes, and section S7.2 defines the new process using the CMS membrane reactor. Sections S7.3 and S7.4 present the assumptions in TEA and LCA and the sensitivity analyses, and Section S7.5 shows the results.

S7.1 Modeling of PDH in Catofin and Oleflex processes

Catofin is the most widely used process to produce propylene⁵¹. The process uses multiple adiabatic reactors with intermediate process heat. Heat is supplied by a furnace at 650°C with a thermal efficiency of 75%⁵², see **Fig. S16** below. The reactors have been modeled by assuming a conversion of 16% in each, which results in an overall conversion of 40%⁵¹. The reaction products in the process are cooled down and sent to a pressure swing adsorption (PSA) system to remove H₂ as co-product. The PSA system comprises of two beds: one in operation and the other in regeneration. It has a H₂ separation efficiency of 82% and operates at 27 °C and 4.0 bar⁵³. A compressor and a heat exchanger are placed before the PSA. A pressure drop of 1.5 bar is assumed in the bed. After the PSA, the product stream needs to be compressed and cooled down in three steps to get a pressure of 23.0 bar in the propylene and propane (i.e., C3) splitter⁵⁴. The column is modeled with short-cut methods for recovering 99% of the propylene in the distillate. The distillate on the top is the propylene that is sold as a finished product. The residue that consists of propane is recycled back to the dehydrogenation reactor.

As an alternative to the Catofin process, the second most widely implemented process for PDH is Oleflex 55. Oleflex process is similar to Catofin with differences in the reactor and the recovery of light fractions, see **Figure S17**. This process consists of four reactors (assuming a 12% conversion in each to get an overall 40% conversion) and a catalytic regeneration unit (CCR). The product stream is sent to a "cold box" (a cryogenic separation column) to separate the H₂ co-product first. After H₂ separation, the hydrocarbon stream is sent to a de-ethanizer where light hydrocarbon

fractions in the product stream are removed. It is assumed that ethane and methane are generated as byproducts in the dehydrogenation reactor with conversion of 1%. After the removal of light hydrocarbons, a C3 splitter to separate propylene and propane is used. As with the Catofin process, propane is recycled back to the dehydrogenation reactor.

S7.2 Modeling of PDH in CMS membrane reactor

The PDH in CMS membrane reactor reached >40% single pass conversion at 450 °C. Thus, one reactor unit was used in the process diagram in **Figure S18**. The feasibility of Joule heating of the CMS hollow fibers allows the process heat supplied from the reactor inside, distinct from the conventional reactor operations with process heat from an external furnace. The "inside-out" heating mode should reduce energy losses. The usage of multiple CMS hollow fibers with catalyst packed in the void space among the hollow fibers in the membrane reactor could lead to uniform heating in the catalyst bed because each of CMS hollow fibers functions as a heating source. This is different from one-way heat transfer mode (i.e., heat transfers from external furnace to catalyst bed in reactor) in the conventional PDH process. Based on these facts, an isothermal reactor was assumed for the CMS membrane reactor for PDH. In addition, electricity can be directly used as the energy source for the CMS membrane reactor, besides the fossil fuel combustion like that being practiced in the state-of-the-art PDH processes.

In **Figure S18**, it is important to note that there are two streams in the flow diagram: the reactive stream that contains mainly propane and propylene and the sweep stream that contains the sweep gas (steam), H₂ and the propylene permeate. Further details of the modeling of each unit are given below.

S7.2.1 Modeling of CMS membrane reactor

Two events take place in the CMS membrane reactor, the catalytic propane activation in the reactive stream and the product separation in situ that transfers hydrogen, propylene, and traces of propane from the shell side to the bore side of the hollow fibers. The reactor operates at 450 °C and it has two feeds: the reactive stream containing only propane and traces of propylene (<0.1wt%) and the sweep stream of pure steam with a molar ratio of 100:1 at the entrance.

The modeling of the reactor in Aspen is carried out using an equivalent system composed of a stochiometric isothermal reactor followed by a separator. In the stochiometric reactor, the steam of the sweep side is considered inert, but it requires to define a conversion. This conversion of the equivalent Aspen Plus® reactor and the separation fractions of the separator are obtained from a one-dimensional isothermal plug flow reactor model, see Eq. S50 and Eq. S51. Several assumptions are made in this model: (1) no axial dispersion, (2) no radial diffusion, (3) no mass transfer resistance, and (4) no pressure drop. The mass balance equations for the reactive (Eq. S50) and sweep (Eq. S51) streams are given below,

$$\frac{dF_{r,i}}{dz} = \rho_b \pi (R_2^2 - nR_1^2) r_i - 2\pi n R_1 Q_i (P_{r,i} - P_{s,i})$$
 (Eq. S50)

$$\frac{dF_{s,i}}{dz} = 2\pi n R_1 Q_i (P_{r,i} - P_{s,i})$$
 (Eq. S51)

where $F_{r,i}$ (mol/s) is the molar flow rate of component i in the reactive stream, z (m) is the catalyst bed length, ρ_b (g/m³) is the catalyst density, R_1 (m) is the outer radius of hollow fiber, R_2 (m) is

the inner radius of the quartz tube, n is the number of CMS hollow fibers, r_i (mol/s/mol_{cat}) is the rate of reaction, Q_i (mol/s/m²/atm) is the gas permeance, $P_{r,i}$ and $P_{s,i}$ (atm) are the partial pressures of component i in the reactive and sweep streams, and $F_{s,i}$ (mol/s) is the molar flow rate of component i in the sweep stream. The differential equations are solved using the Runge-Kutta method in MATLAB.

The results obtained in the 1-D kinetic model are used to define the conversion and separation fractions of an equivalent reactor plus a separator in Aspen® Plus. The conversion of the equivalent reactor ($X_{C_3H_8}$), modeled as isothermal, is determined from the kinetic results as presented in Eq. S52, where F_{out,r,C_3H_8} is the propane at the exit in the reactive side, F_{out,s,C_3H_8} is the propane at the exit in the sweep side, and F_{in,r,C_3H_8} is the flux at the entrance, respectively. The separation fraction of each component in the separator of the Aspen® Plus simulation, $f_{sep,i}$, is determined as in Eq. S53, where $F_{out,r,i}$ and $F_{out,s,i}$ are the mass flow rates for every component in the reactive and sweep sides, respectively. A summary of the results for the base case is provided in **Table S12**.

$$X_{C_3H_8}(\%) = \frac{(F_{out,r,C_3H_8} + F_{out,f,C_3H_8}) - F_{in,r,C_3H_8}}{F_{in,r,C_3H_8}}$$
(Eq. S52)

$$f_{sep,i} = \frac{F_{out,r,i}}{(F_{out,r,i} + F_{out,s,i})}$$
(Eq. S53)

S7.2.2. Product separation and propane recovery

The two streams leaving the reactor are cooled down to 30°C and the sweep stream is sent to two consecutive flash separators to separate the water from the gas components. After removing the water in "Flash-1", the sweep stream is composed of H_2 (58% in mol), propylene (30% in mol), propane (11% in mol), and traces of vapor (~1%). This gas stream obtained in "Flash-1" is sent to a PSA system where H_2 is removed with an efficiency of 82.5%⁵³. The PSA system operates at 30°C and 4 bar, so it is necessary to compress and cool down the stream before this unit. Two PSA beds are considered in the system, one in operation and the other in regeneration. After removing the H_2 , a rich propylene stream (~80% propylene) is obtained as a product.

The reactive stream obtained in the CMS membrane reactor, stream S-7 of **Figure S18**, contains a mixture of H₂, propane, and propylene that must be separated. After cooling down this stream, H₂ is recovered with the PSA system that requires the gas stream to be compressed and cooled down. After the PSA, the product obtained is mainly composed of propane and propylene that are separated in a distillation tower at high pressure (23 bar)⁵⁴. The tower is designed with short-cut methods, to recover 99% of the light component, propylene, in the distillate and allowing only 1% of the heavy component, propane, to leave the tower in the distillate. The resultant tower has 148 trays, and a recycle ratio of 16, which are in the range (100-200 trays and recycle ratio between 10 and 20^{56,57}) reported in previous reports. The propylene obtained in the head can be sold as a finished product. The propane obtained at the bottom is recycled to increase the yield of the process.

S7.3 Assumptions in TEA and LCA of PDH in CMS membrane reactor

S7.3.1 Assumptions in technoeconomic analysis

TEA is performed to determine the economic potential of PDH for propylene production in the CMS membrane reactor system compared with the current state-of-the-art. The plant designed

operates 8,000 h per year and processes 500 kt/y of propane, similar to the ones reported in literature⁵¹. The minimum selling price (MSP) of propylene is used for comparing the potential of this new technology to other technologies. Discounted cash-flow method is followed for computing the MSP, assuming an internal rate of return of 10%⁵⁸ 20 years are considered for the life of the plant. A corporate tax of 21%⁵⁹ is also imposed on the profits in the estimation of the MSP. The MSP estimation requires computing the capital costs (CAPEX) and operating costs (OPEX) of the process. Aspen Process Economic Analyzer v.11 is used to estimate the investment cost and the installation for most of the process units. Since they are not available in Aspen, the costs for reactors and the PSA systems are determined using custom estimations as described below. All the costs estimated by Aspen Process Economic Analyzer v.11 are based on 2018 Q1, so they are updated with the plant cost index of the Chemical Engineering Magazine to the values of 2021^{60,61}.

(1) The investment cost of the PSA systems is determined by the cost of the vessel plus the cost of the adsorbent. The mass flow rate of the hydrocarbons (propylene, propane, C₂ and methane) and 17.5% of the H₂ (note that the remaining 82.5% is separated based on the efficiency of the bed⁵³) are used to determine the mass of adsorbent required in the bed, see Eq. S54. HZSM-5 zeolite is used as adsorbent.

$$m_{HZSM5,i} = \frac{n_i \cdot t_{op}}{csorp_i}$$
 (Eq. S54)

In Eq. S54, $m_{HZSM5,i}$ stands for the mass of HZSM-5 zeolite required for adsorption of each compound i, n_i is the molar flowrate of each component i, t_{op} is the operating time of the bed (assumed to be 370 s⁶²), and $Csorp_i$ is the sorption capacity of each component (propane⁶³, propylene⁶³, ethane⁶⁴) on HZSM-5. The mass required is used to determine the investment cost of the sorbent. The price of HZSM-5 used as sorbent has been determined with the CatCost tool following the example given in⁶⁵. The price obtained is \$9.72/kg and a replacement period of 5 years is assumed. The mass is also used to determine the volume of the vessel with a density of 875 kg/m³. Based on the volume, the vessel is designed following the procedure reported in Walas⁶⁶. The vessel is assumed to be made of steel with a length to diameter (i.e., L/D) ratio of 2.5⁶⁶. The thickness is computed following the ASME method, selecting the highest one obtained for the longitudinal and circumferential stresses. The thickness for the longitudinal stress (t_l) is computed as in Eq. S55 and the thickness for the circumferential stress (t_c) is computed in inches as in Eq. S56.

$$t_l = \frac{PR}{2SE + 0.4P} \tag{Eq. S55}$$

$$t_c = \frac{PR}{SE - 0.6P} \tag{Eq. S56}$$

In these two equations, P is the internal pressure of the vessel (psi), R is the internal radius (inch), S is the maximum allowable stress of steel 15,000 (lb/in²),⁶⁷ E is the welding factor assumed to be $0.85.^{68}$ The thickness and the internal volume allow to determine the volume difference, which is the steel volume, and the steel mass can be determined with a density of 7,850 kg/m³.⁶⁹ The mass obtained for the vessel is finally applied to compute the cost of the vessel as reported in Towler and Sinnot⁷⁰, see Eq. S57. The cost of the vessel (C_{vessel}) is updated to 2021 with the CEPCI indexes^{60,61}.

$$C_{nessel} = a + bS^n (Eq. S57)$$

In Eq. S57, a is -2,500, b is 200, S is the mass of steel in kg and n stands for 0.6.⁷⁰ Since two vessels are operating simultaneously, the overall capital cost (vessel plus sorbent) is multiplied by 2.

(2) Capital cost of PDH reactors in Catofin and Oleflex processes are computed with cost of the catalyst plus cost of the furnace to supply the process heat. The catalyst mount $(m_{catalyst})$ is determined from the volume hourly space velocity (VHSV), i.e., 0.1 L g_{cat}^{-1} h⁻¹, as shown in Eq. S58, where V and $x_{C_3H_8}$ are the volume flow rate and the molar fraction of propane, respectively. Catofin employs alumina supported chromium oxide (Cr_2O_3/Al_2O_3) catalyst that has 20wt% Cr_2O_3 loadings⁶¹.

$$m_{catalyst} = \frac{v_{x_{C_3H_8}}}{v_{HSV}}$$
 (Eq. S58)

The catalyst cost is estimated with the CatCost estimation tool [B-14]. The estimation is performed by the "Step Method". In all the cases, a medium size plant of 10 tons per day (i.e., 10 t/d) with 1 day of production and 1 day of cleaning is used based on the default settings. The remaining economic inputs also use the default values. In the Catcost tool, alumina is selected as support and chromium nitrate (Cr(NO₃)₃) with a price of \$20/kg⁷¹ is used. The Cr(NO₃)₃ amount ($m_{Cr(NO_3)_3}$) per kg of Al₂O₃ support is determined from the 20wt% Cr₂O₃ concentration in the catalyst⁷¹ and the reaction equation of 2Cr(NO₃)₃ \rightarrow Cr₂O₃+6NO₂+1.5O₂. Eq. S59 shows the calculation method, where $MW_{Cr(NO_3)_3}$ and $MW_{Cr_2O_3}$ are the molecular weights of Cr(NO₃)₃ and Cr₂O₃ respectively, and $m_{Cr_2O_3}$ is the mass of Cr₂O₃ compound determined from Eq. S58.

$$m_{Cr(NO_3)_3} = 2 \frac{MW_{Cr(NO_3)_3}}{MW_{Cr_2O_3}} \cdot m_{Cr_2O_3}$$
 (Eq. S59)

The equipment used in the catalyst synthesis depends on how the catalyst is prepared. An "incipient wetness" approach is selected initially for impregnation, together with a rotatory dryer and a kiln⁷². The cost of the catalyst obtained in the tool is \$16.78/kg. The catalyst lifetime is assumed to be 3 years.

(3) In the case of PDH in the CMS membrane reactor, the cost is estimated by splitting the unit into three parts: catalyst, membrane and vessel. The catalyst cost is estimated with the CatCost estimation tool⁶⁵. Following the catalyst synthesis procedure described in Section 1.2.1, the reagents were determined, and their estimated costs are summarized in **Table S13**^{65,73-76}.

The apparatuses considered for catalyst preparation include: 5 mixers (3 of them for the raw materials preparation and 2 for autoclaves), 1 continuous kiln, 1 plate and frame filter, 1 mixing reactor used as mixing tank for washing, 1 rotary dryer and 1 extruder. With these inputs, the cost obtained for the catalyst is \$65.5/kg. The catalyst showed outstanding stability in the PDH, so it is assumed to be replaced every 10 years.

The membrane is estimated with a price of $100/\text{m}^2$ for a module of 3000 m^2 . The mass transfer area is given by the fibers, which are expected to have a discount by buying large quantities and the scale-up is performed with a 6/10 rule.

The vessel is designed in a similar way to the PSA system. The average density of the catalyst is assumed to be 875 kg/m³. The volume obtained is used to compute the length and diameters of the vessel with a L/D ratio of 2.5. The thickness and cost are calculated as in Eqs. S55-S57. Finally, the cost is updated to 2021.

Apart from the CAPEX, the operating costs are also estimated. The following assumptions are made:

- (1) The cost of the propane is assumed to be $1.8/\text{gal}^{78}$.
- (2) Utilities costs are assumed as $\underline{\phi}6.35$ /kWh for electricity⁷⁹, \$6.6/MMBTU for natural gas⁸⁰ and $2.1 \cdot 10^{-7}$ \$/kJ for refrigerating water⁸¹.
- (3) H_2 co-product is sold at a price of \$1.7/kg⁸².
- (4) 12 operators (4 of them working simultaneously) are assumed in the plant, divided into the following four shifts: dehydrogenation reactor, H₂ separation, propylene separation and utilities management.
- (5) The cost of supervision is computed as 15% of the total labor cost of the operators⁸³.
- (6) Maintenance cost per year is determined using 4% of the total CAPEX⁸³.
- (7) Operating charges are computed as the sum of the charges for product control in the laboratories are assumed to be 15% of the labor expenses.
- (8) Insurance, local property taxes, rent, etc. are also estimated with an average value of 15% of the labor costs⁸³.
- (9) Plant overhead costs are determined as 60% of the total expense for operating labor, supervision, and maintenance⁸³.
- (10) Administrative costs are computed as 25% of the total labor costs⁸³.

7.3.2 Assumptions in life cycle analysis

LCA is performed following Traci method⁸⁴ to evaluate the environmental performance of PDH in the CMS membrane reactor versus conventional processes. System expansion method has been performed with Ecoinvent® v3.8 as a database for estimating the emissions of the processes, simplified as in **Figure S19**. One kilogram of propylene is taken as a functional unit. The following assumptions are considered in the LCA:

- (1) Only materials used in continuous manufacturing are considered. Other materials involved in the construction phase, infrastructure, and catalyst preparation are not considered.
- (2) Propane is assumed to be provided by a third vendor accounting for the CO₂ emissions of the processing and distribution.
- (3) Hydrogen sold as a by-product is assumed to substitute hydrogen produced by steam reforming.
- (4) Cooling water is assumed to have a gradient of 5°C in the cooling tower. It is assumed that 1% of the cooling water is evaporated into the atmosphere⁸⁵, and the remaining 99% is recycled.

- (5) As a base case, electricity is supplied from a medium voltage grid based on the average technology and loss in the US. In cases where other renewable sources are used, the emissions factors are computed accordingly.
- (6) Heat is assumed to be supplied from a furnace fed with natural gas.
- (7) CO₂ emissions generated in the regeneration of the catalyst are also included. They are computed from the complete coke (assumed as pure carbon) oxidation deposited in the catalyst. Catofin has a deposition of 0.1w% of coke per mass of catalyst in 10 min, Oleflex has a deposition of 10w% of coke per mass of catalyst over 100 h and CMS reactor has a deposition of 1.8w% of coke per mass of catalyst over 110 h.

S7.4 Scenario analyses

Sensitivity analysis is performed on several process variables to understand their effects on the process and how different processing alternatives can increase or reduce the MSP of propylene and the environmental impacts. The variables analyzed are described below.

(1) Pinch temperature: The effect of pinch temperature for the integration of HEX-1 with HEX-2 and HEX-3 of Figure S18 is evaluated. The default value is assumed to be 5 °C, but higher or lower pinch temperatures are evaluated for 3 °C and 10 °C, respectively. Higher pinch temperatures reduce the area required and the CAPEX since LMTD is higher. However, higher pinch in the energy integration also results in less energy integrated and more external energy requirements. Eq. S60 is used for computation of the additional heat requirements defined as where Q_{ext} . $T_{out\ HEX1}$ and $T_{in\ HEX1}$ are outlet and inlet temperatures of HEX-1, $\overline{c_{p_{cold}}}$ and $F_{tot,cold}$ are average heat capacity and flow rate of cold stream in HEX-1, and Q_{int} is energy supplied (integrated) from HEX-2 and HEX-3, respectively. The energy supplied from the integration is given The energy supplied from the integration with the hot stream (Inlets of HEX-2 and HEX-3) at the exit of the reactor is computed from the energy balance using Eq. S61, in which F_h is the sum of the flow rate of the inlets in HEX-2 and HEX-3. $\overline{c_{p_{a,cold}}}$ is the mass average heat capacity of the gas, $T_{h in}$ is the inlet temperature of the hot stream, Tboil is the boiling temperature of water, wwater is the mass fraction of water, λ is the vaporization enthalpy of water, $c_{p_{l,cold}}$ is the average heat capacity of the mixture including water as liquid and $T_{out\ hot}$ is the inlet temperature of the exits defined as the cold temperature plus the pinch temperature, ΔT_{pinch} . This heat can be used to compute the heat transfer area as shown in Eq. S62, where all the temperatures are summarized in Table S12. Note that both Eqs. S61 and S62 need to define the temperatures. For heat transfer to occur, the temperature difference between the hot and cold streams needs to be positive, and it is necessary to fix a value for the temperature at cold exit of the hot stream, the pinch temperature. The values for the temperatures are given in **Table S14**.

$$Q_{ext} = (T_{out\ HEX1} - T_{in\ HEX1}) \cdot \overline{c_{p_{cold}}} \cdot F_{tot,cold} - Q_{int}$$
 (Eq. S60)

$$Q_{int} = F_h \cdot \overline{c_{p_{g,cold}}} \cdot (T_{h\,in} - T_{boil}) + F_h \cdot w_{water} \cdot \lambda + F_h \cdot \overline{c_{p_{l,cold}}} \cdot (T_{boil} - T_{out\,hot}) \quad \text{(Eq. S61)}$$

$$Q_{int} = U \cdot A \cdot \frac{(T_{hin} - T_{cout}) - (T_{cin} - T_{hout})}{\ln(\frac{T_{hin} - T_{cout}}{T_{cin} - T_{hout}})}$$
(Eq. S62)

- (2) Ratio of sweep flow rate to reactive feed flow rate: The ratio of sweep flow in the bore side to the feed flow in the shell side (i.e., steam/propane flow rate ratio) in the reactor is varied by adjusting the steam flow rate at a fixed propane flow rate. A decrease in the steam/propane flow rate ratio reduces the energy consumption since the heat requirements depend on the mass flowrate of steam to be heated. However, this decrease also reduces the conversion since less H₂ permeates. In order to maintain the same conversion in the process, for the steam/propane flow rate ratio of 10, two cases were modelled:
- The first case involves a process structured with two reactors (i.e., #1 and #2 reactor) of the same size in series (**Figure S20**). The use of the secondary reactor increases the capital cost. A summary of the characteristics of the reactors in this case is given in **Table S15**.
- The second case follows a similar strategy but having 2 smaller reactors with the total size of the single reactor of **Figure S18**. Between the two smaller reactors, a fresh stream with a steam/propane flow rate ratio of 10 is introduced, reducing the heat consumption versus the ratio of 100, see **Figure S21**. Furthermore, the concentration of propylene and H₂ in the sweep side is also reduced when the fresh stream is introduced, improving their permeation. This enhances the transport versus a single reactor, as can be checked by comparing the conversion of the first reactor in **Table S15** versus the conversion of the second reactor in **Table S16**. Note that Reactor #1 of **Table S15** has the same Steam:Propane ratio of 10 and the same amount of catalyst than the two reactors of **Table S16**.
- (3) Use of H₂ co-product: H₂ can be burnt in the furnace to supply process heat, reducing CO₂ emissions and external energy consumption. However, using it as fuel is expected to worsen the process economics since it is an expensive product to synthesize, and there are cheaper fuels to cover the energy requirements.
- (4) Alternative electricity sources: Technologies with low emissions have been studied with the emissions calculated using Ecoinvent® and the following prices. The modification in the economic analysis has been only considered for renewable-based sources like photovoltaic and wind energy, which are assumed to have a price of 63 c/kWh and 26 c/kWh⁸⁶. Nuclear is assumed with the same price as electricity.

A summary of all the case studies together with the codes for all cases for identification is given in **Table S17**.

S7.5 TEA and LCA results

S7.5.1 TEA results

The MSP of propylene and the CAPEX for a plant processing 500 kt/y in all case studies are summarized in **Table S18**. The results show that conventional processes and in particular Oleflex, are more profitable than the new PDH process designed for the CMS membrane reactor. A comparison of the cost breakdown for MSP is provided in **Figure S22-S23**. In all the cases studied, the price of propane is the main contributor to the final propylene price explaining why propylene price is highly dependent on petroleum prices. However, since the unreacted propane is recycled, the overall yield of the entire process is very similar for all the processes and the main differences are due to the conversion in the reactor, the energy consumption and their prices, and the investment cost of the plants. Current technologies such as Catofin and Oleflex show lower MSP

than the CMS membrane reactor developed in the present work. Although the CMS membrane reactor reduces the electricity requirements in the separation of H₂, and the heat requirements in the depropanizer are lower since less mass is separated as shown in other studies⁵⁶, there is an increase in the energy due to the need of heating the sweep gas (which cannot be perfectly integrated), see **Table S19**. Furthermore, the price of electricity is nearly 10 times higher than heating with a furnace in the reactor making the new reactor less competitive than conventional technologies. In addition to the energy costs, the membrane price also increases the investment costs, resulting in a higher MSP. A breakdown of the CAPEX is provided in **Figure 24-25**. For further details of the contributors in the reactor, **Figure S26** provides a breakdown of the elements that compose the conventional reactors and the CMS membrane reactor.

S7.5.2 LCA results

LCA is performed by comparing the CO₂ emissions from the conventional processes to those in different alternatives of the new membrane reactor process. The environmental impact results of all the studied processes are provided in **Tables S20-S23**. A comparison of all the emissions versus the Catofin process taken as base case is also provided in **Tables S20** and **S23**. The comparison shows that the new technology has more emissions than the state-of-art-processes. Even when the reactor is internally split into two small reactors with two sweep streams, the CO₂ emissions are 13% higher than the Catofin process. These higher emissions are due to two main factors as discussed below.

- (1) The electricity mix of US has a high contribution of fossil-based resources (around 70% is coming from natural gas, petroleum, and coal).
- (2) The use of electricity generated from a fossil-based resource through a Rankine, Brayton, or any other cycle is less efficient than the production of steam straightforwardly by burning the fossil fuel. The heat transfer efficiency in a furnace is the only barrier with values around $\sim 80\%^{52}$, so only 20% of the energy contained in the fuel is lost. However, through a Rankine cycle with a \sim 45% efficiency, the energy losses are around 55%. Furthermore, efficiency is even lower due to the losses in transportation.

One way to reduce the CO₂ emissions from the new membrane reactor technology is by the substitution of the power source with a fully renewable resource or by nuclear power. Thus, when the network is fully renewable, the CMS membrane reactor with process heat from Joule heating becomes an interesting alternative for electrifying the propylene production and reduce the CO₂ emissions by up to 20%. A more detailed breakdown of the CO₂ emissions is given from **Figure S27-29**. The most relevant comparison can be observed in **Figure S29**, where the emissions generated by power dramatically drop in the case of renewable energy sources and nuclear energy. Another way to reduce the emissions is by having a low pinch in the heat integration of the sweep stream's recycled steam. However, there are also limitations in the implementation of this solution since the ratio of steam is high and having only a pinch of 3 °C results in a heat exchanger area of 162,747 m², which requires 8 heat exchangers of 20,000 m² (maximum size of commercial heat exchangers) and another of 2,747 m². In the case of 5 °C of pinch, the area is still significant, 103,908 m²; but it is like the one with a higher pinch, for 10 °C is 51,834 m². Above 5 °C, the heat exchanger area is governed by the mass flowrate.

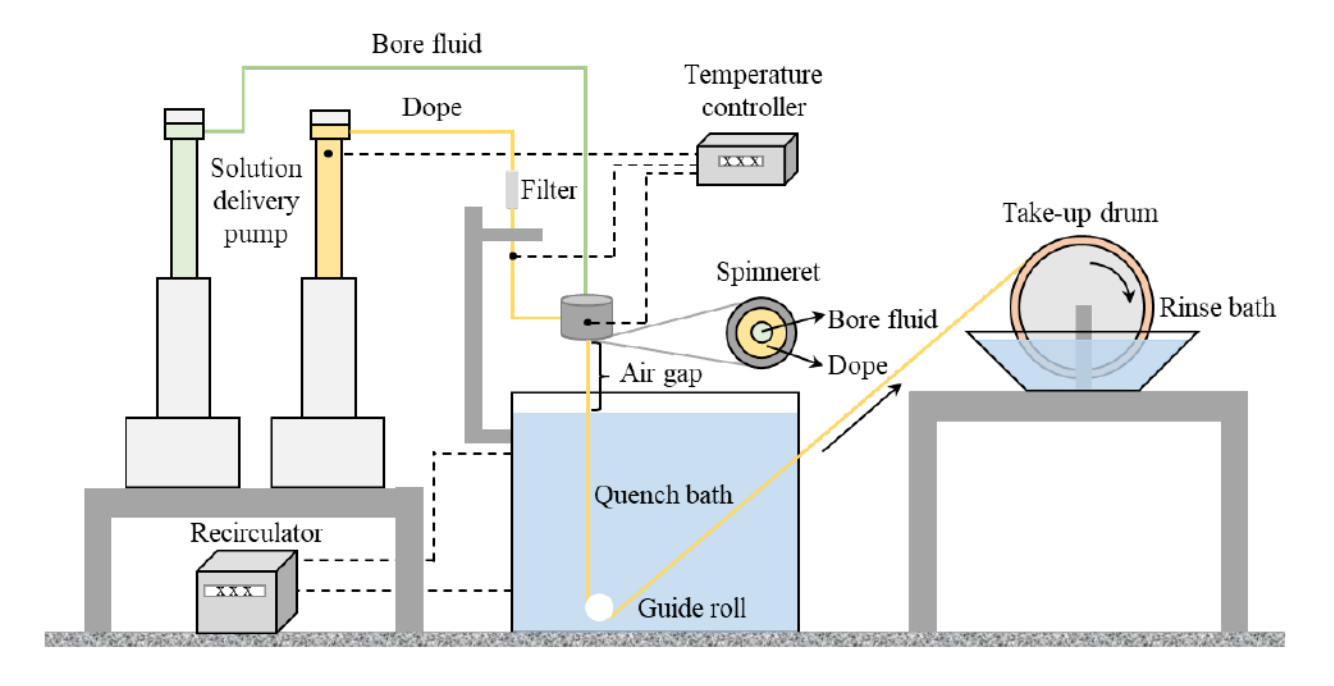


Figure S1. Schematic illustration of the dry-jet/wet-quench spinning process for fabrication of the Matrimid® polymer hollow fibers.

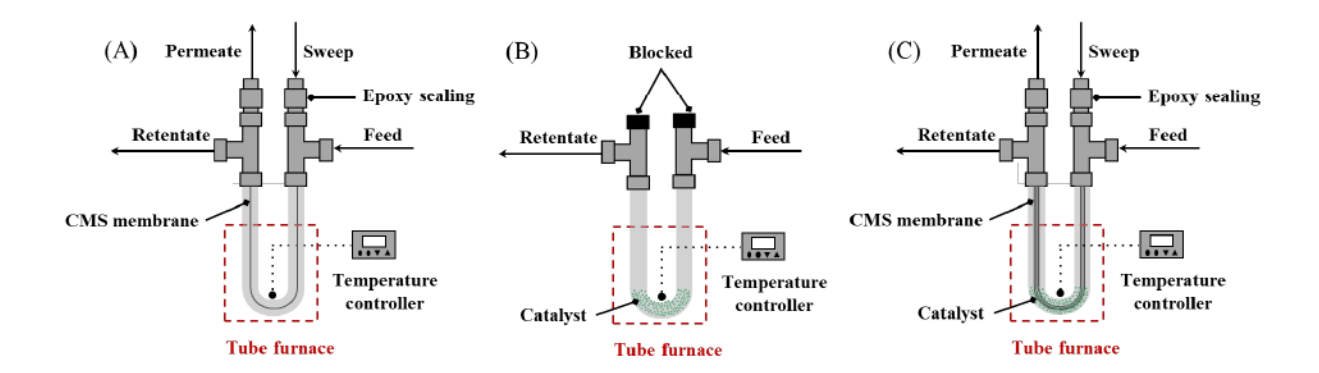


Figure S2. Schematics of membrane module (A), packed bed reactor (B), and membrane reactor module (C) that are used in the reactor rig system for membrane separation, catalyst activation, and membrane reactor performance tests.

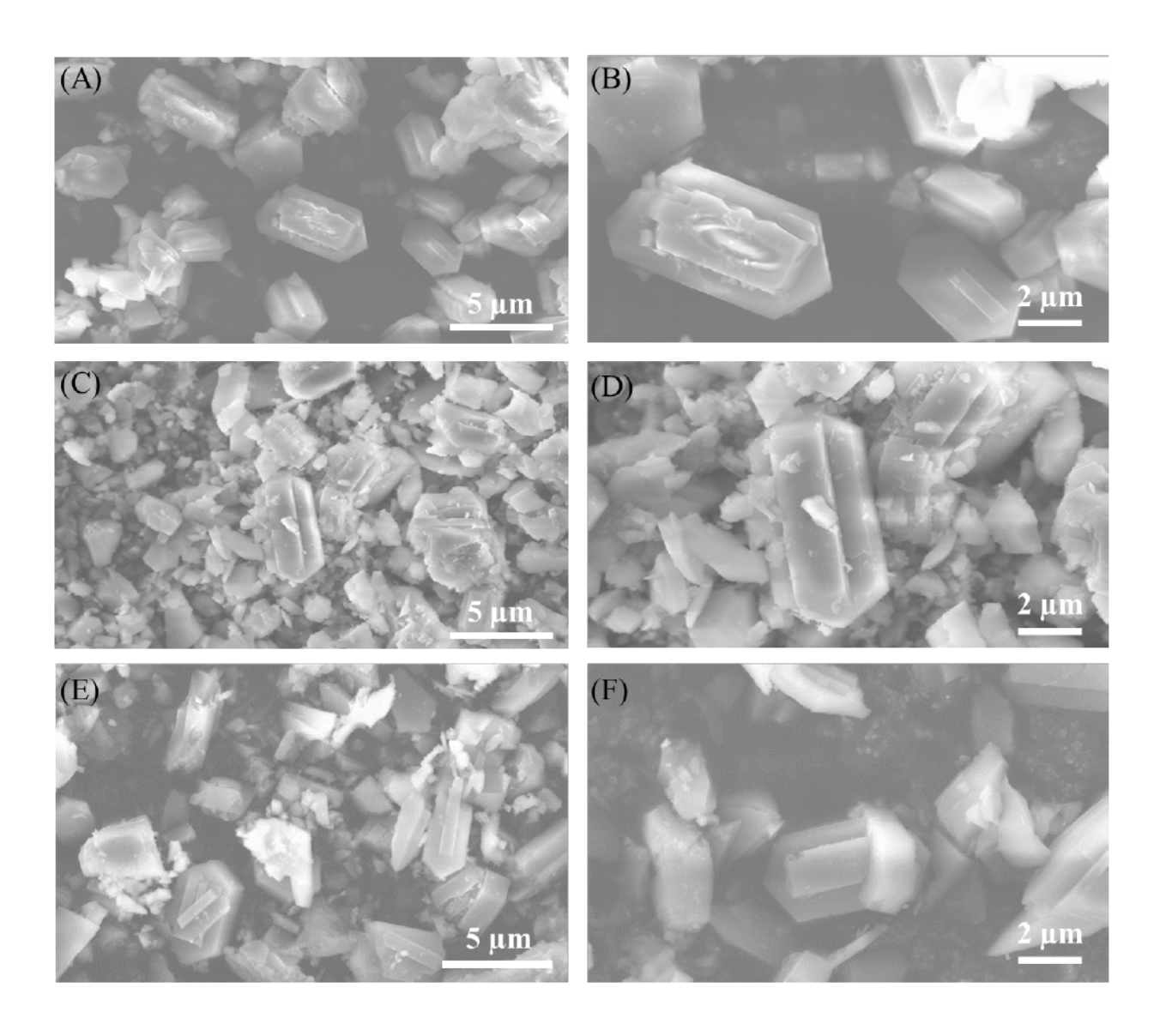


Figure S3. SEM images showing morphologies of as-synthesized (A)-(B), pre-reduced (C)-(D), and spent (MR, 110 hrs TOS) (E)-(F) Pt-Zn/S1 catalyst for the PDH reaction.

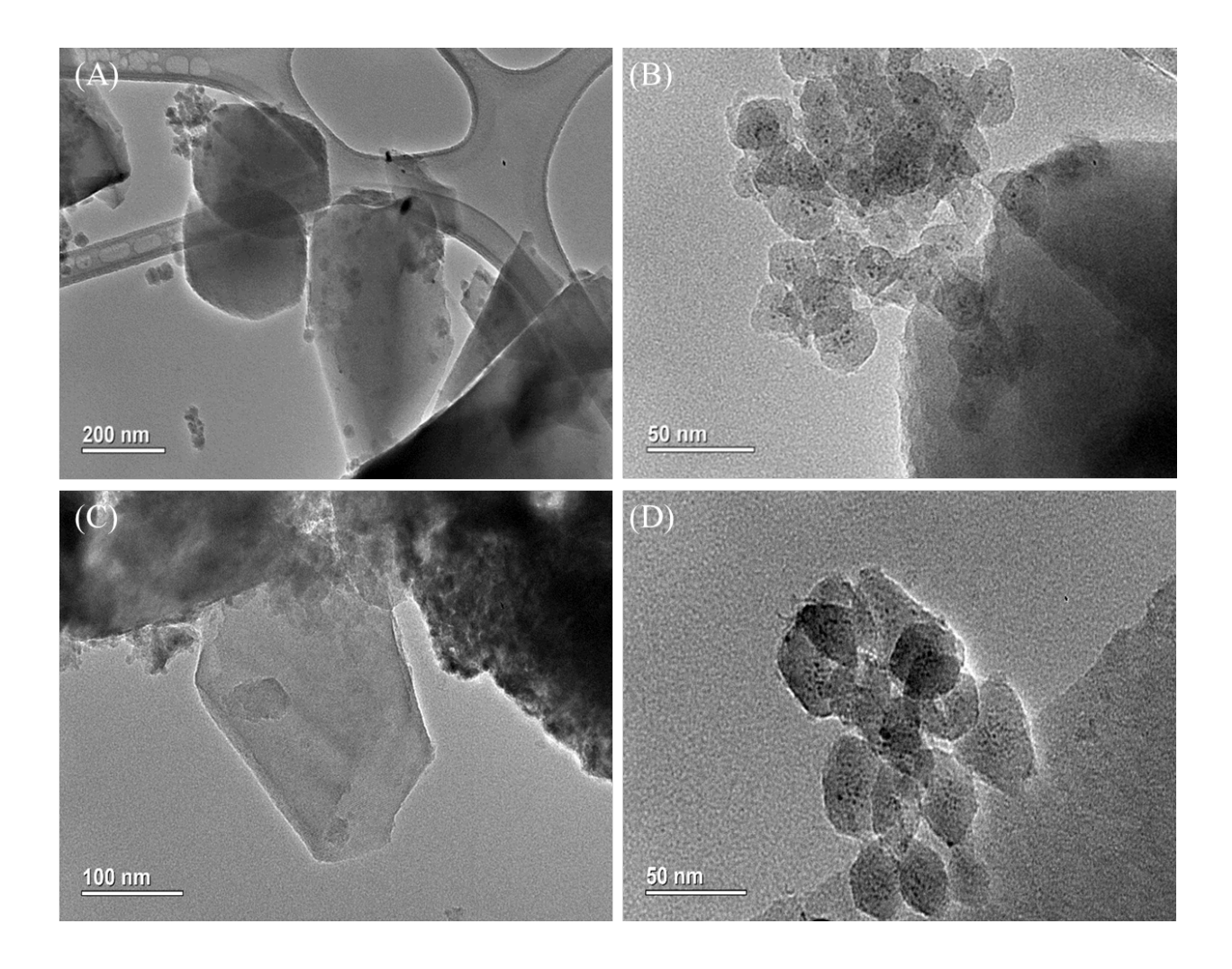


Figure S4. TEM images of pre-reduced (A)-(B) and spent (C)-(D) (MR, 110 hrs TOS) Pt-Zn/S1 catalyst under low and high magnifications, showing morphologies of the particles (A)(C) and metal species in the particles (B)(D), respectively.

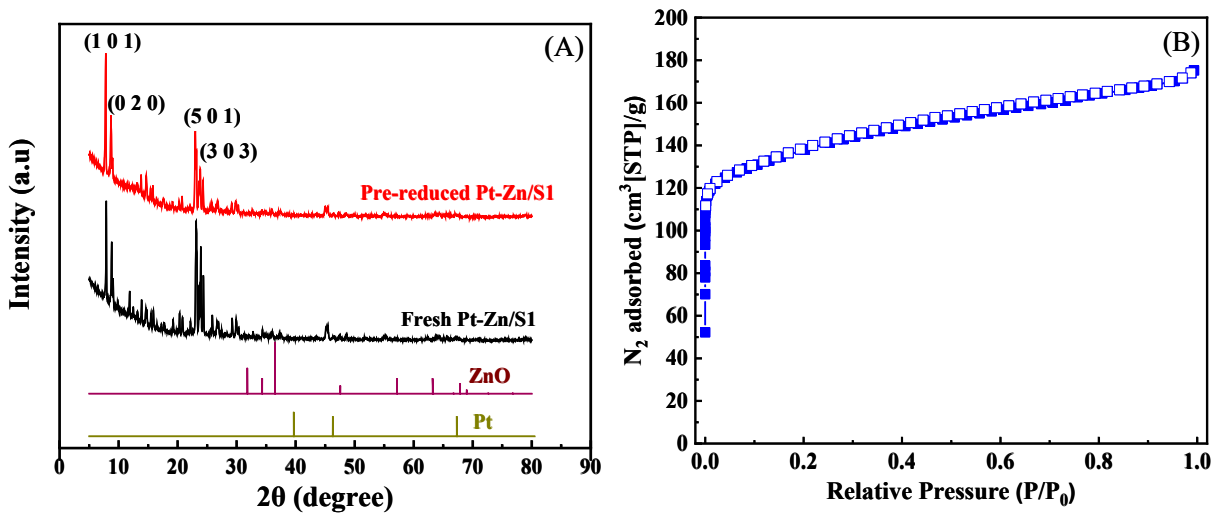


Figure S5. (A) XRD patterns of as-prepared and pre-reduced Pt-Zn/S1 catalyst samples. (XRD patterns of Pt and ZnO are included for comparison purpose.) (B) N₂ adsorption/desorption isotherm of the pre-reduced Pt-Zn/S1 catalyst.

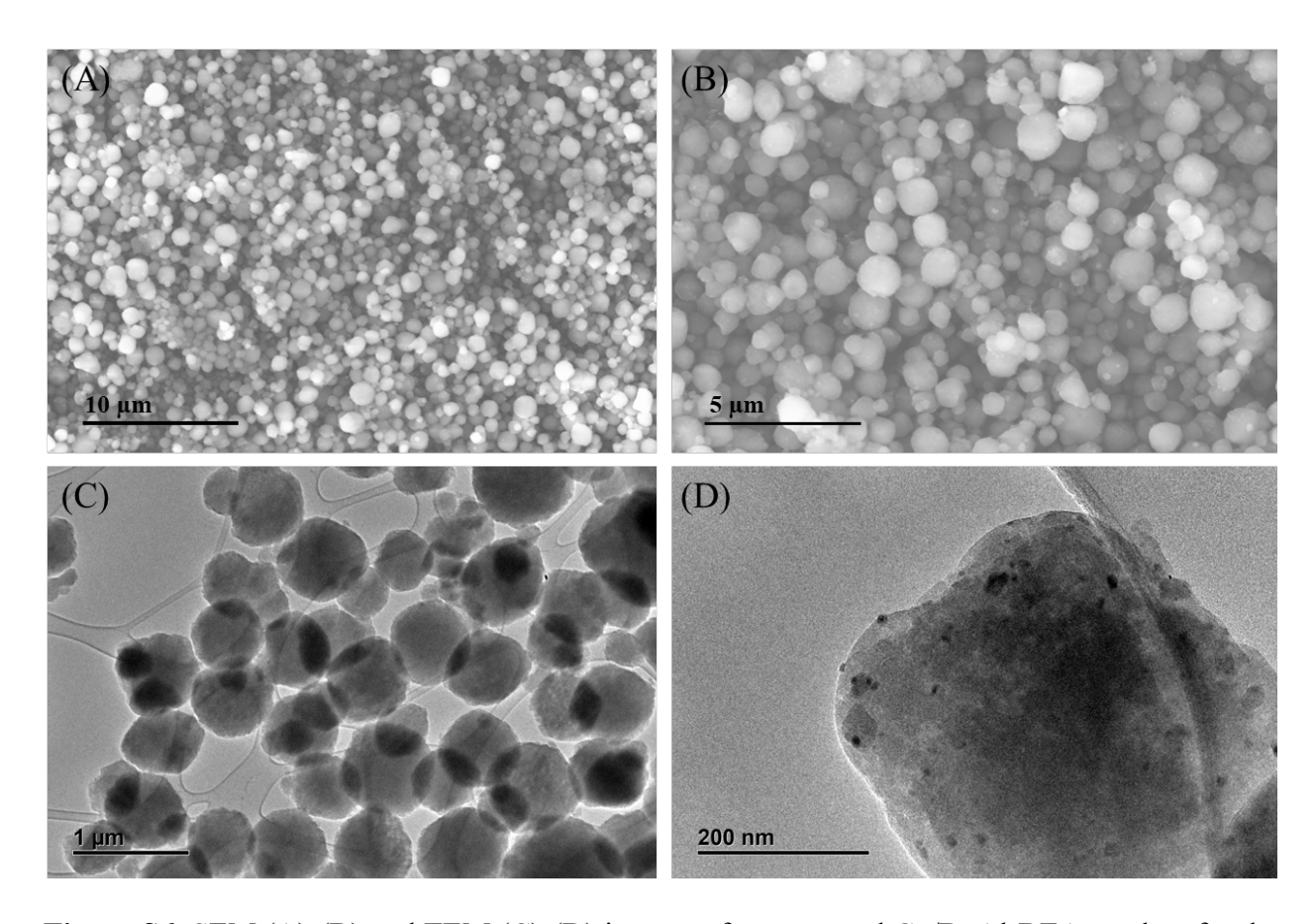


Figure S6. SEM (A)-(B) and TEM (C)-(D) images of as-prepared Co/DeAl-BEA catalyst for the EDH reaction.

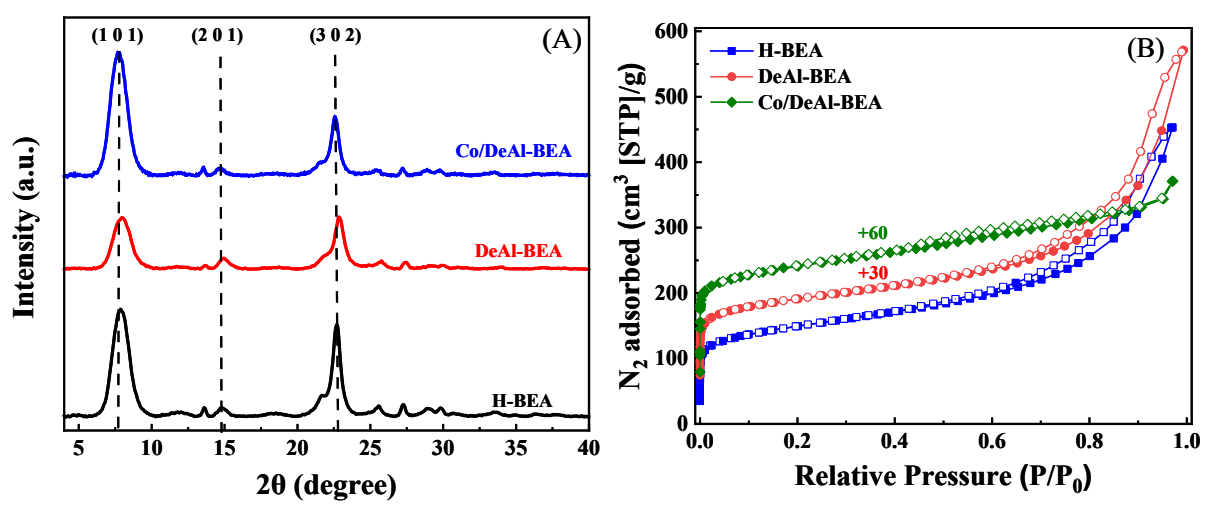


Figure S7. XRD patterns (A) and N₂ adsorption/desorption isotherms (B) of parent H-BEA, DeAl-BEA and as prepared Co/DeAl-BEA samples.

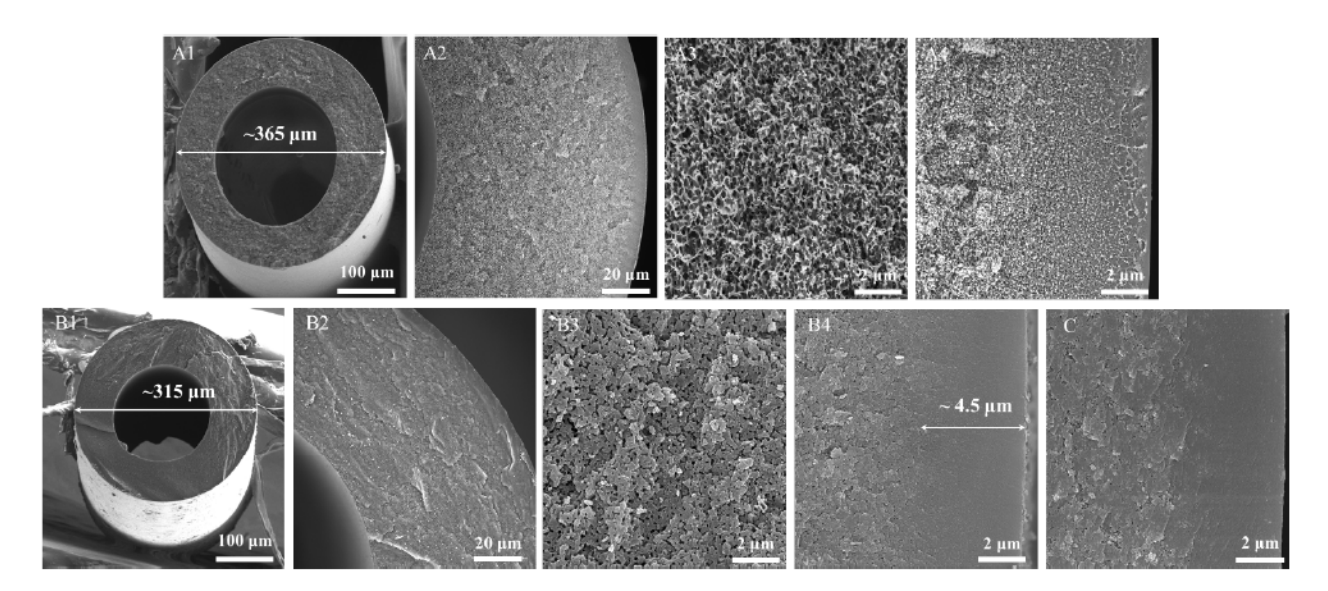


Figure S8. SEM images of Matrimid® precursor hollow fiber membranes (A), Matrimid®-derived CMS hollow fiber assymetric membranes (B) and spent CMS hollow fiber membrane (MR, 110 hrs TOS) (C) (A1 & B1: hollow fiber overview; A2 & B2: hollow fiber wall; A3 & B3: hollow fiber substrate; A4 & B4&C: hollow fiber cross-section near shell side.)

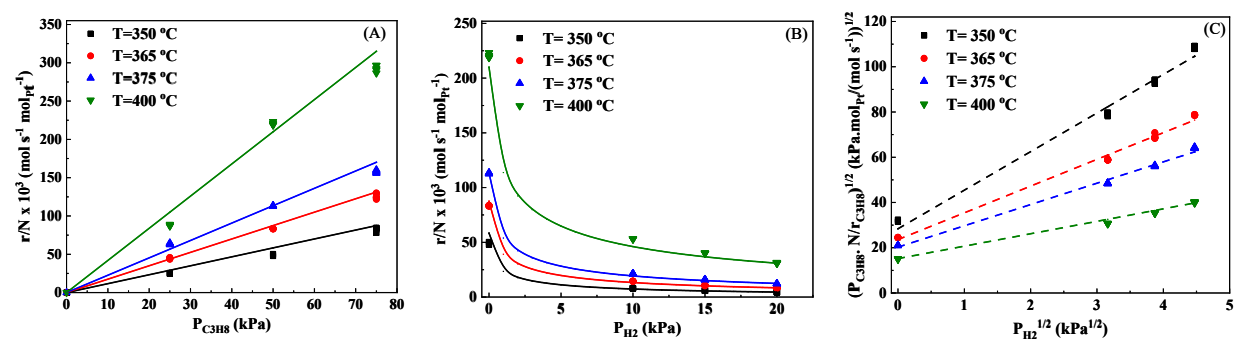


Figure S9. Measured propane reaction rate as a function of propane pressure (A) and hydrogen pressure ($p_{C_3H_8}$ =50 kPa) (B) in PDH over Pt-Zn/S1 catalyst. (C) shows the linearized plots for kinetics data in (B) based on Eq. S35. The solid lines in (A) and (B) present predictions from determined rate equation (i.e., Eq. S33).

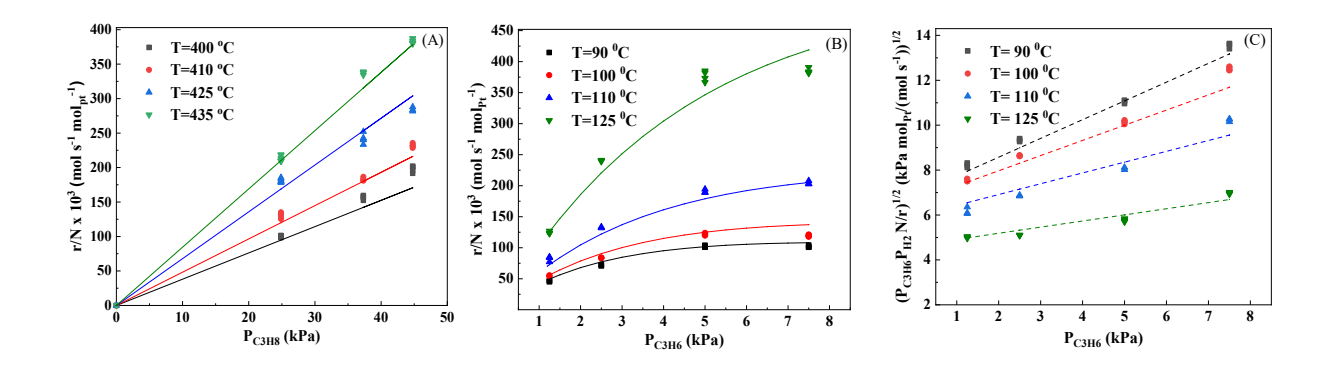


Figure S10. (A) Measured propane reaction rate as a function of propane pressure in the presence of propylene ($p_{C_3H_6}$ =2.5 kPa). (B) Measured reaction rate of hydrogenation of propylene as a function of propylene pressure in the presence of hydrogen (p_{H_2} =2.5 kPa). (C) shows the linearized plots for kinetics data in (B) based on Eq. S37. The solid lines in (A) and (B) present predictions from determined rate equation (i.e., Eq. S33).

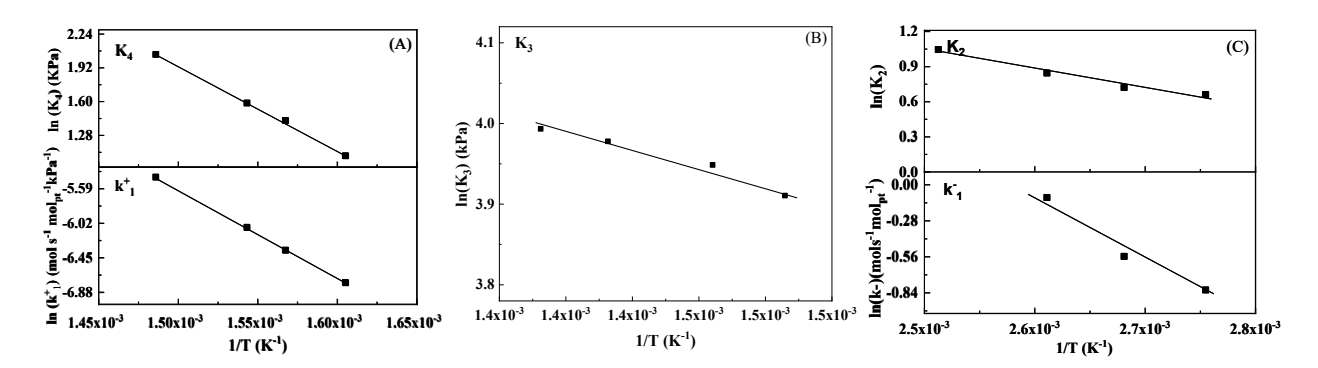


Figure S11. Measured (A) forward rate constant and H_2 desorption constant $(k_1^+ \text{ and } K_4)$ and (B) C_3H_6 desorption constant (K_3) (C) backward rate constant and surface reaction equilibrium constants (k_1^-, k_2) in PDH over Pt-Zn/S1 catalyst as a function of the inverse temperature.

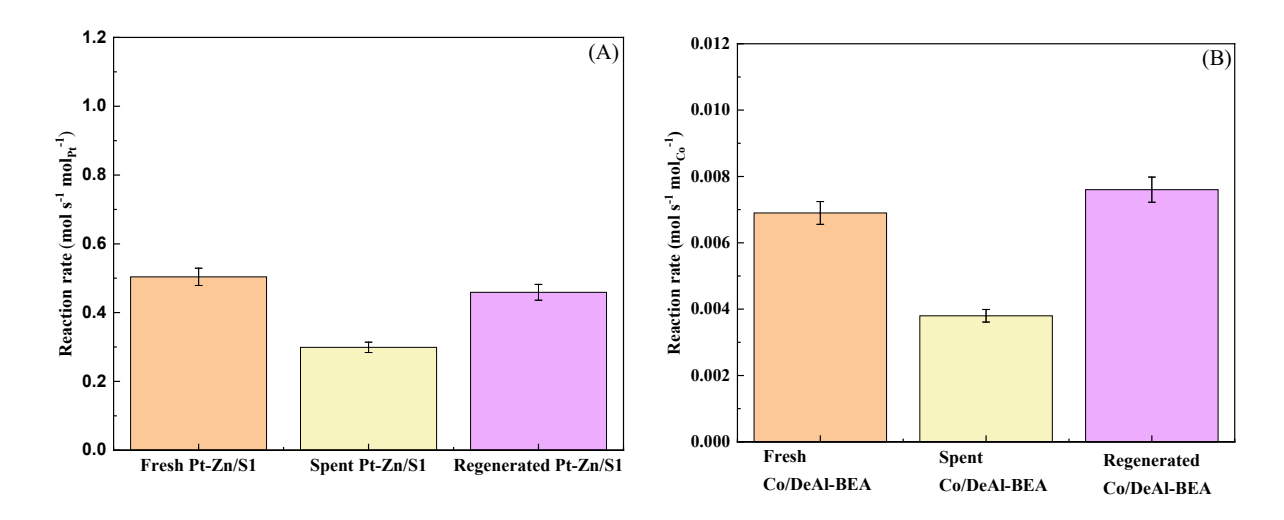


Figure S12. (A) Reaction rates of fresh, spent (after 112 h test in MR) and regenerated Pt-Zn/S1 catalysts. (Reaction condition: temperature: 450 °C, WSHV= 51.53 h⁻¹, 50% C₃H₈/50% Ar) (B) Reaction rates of fresh, spent (after 110 h test in MR) and regenerated Co/DeAl-BEA catalysts. (Reaction condition: temperature: 500°C, WSHV= 21.47 h⁻¹, 50% C₂H₆/50% Ar.)

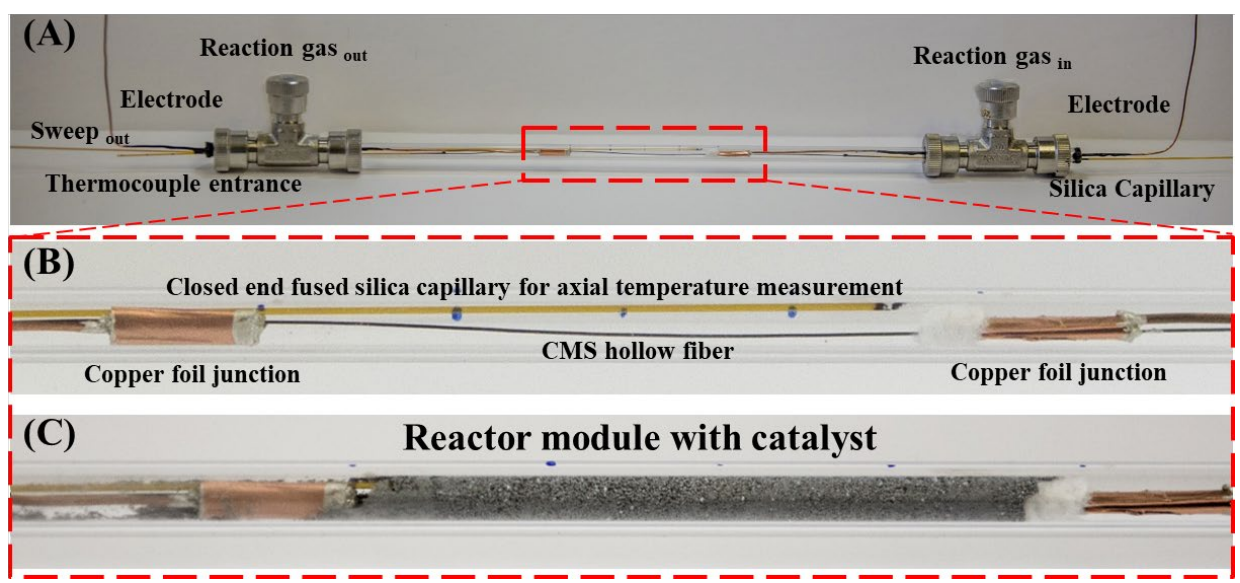


Figure S13. Digital images of the CMS membrane reactor with process heat from Joule heating. (A) Entire reactor module without catalyst loading, (B) A close view of CMS Fiber and thermocouple layout in the module in (A), and (C) A close view of catalyst bed in the module.

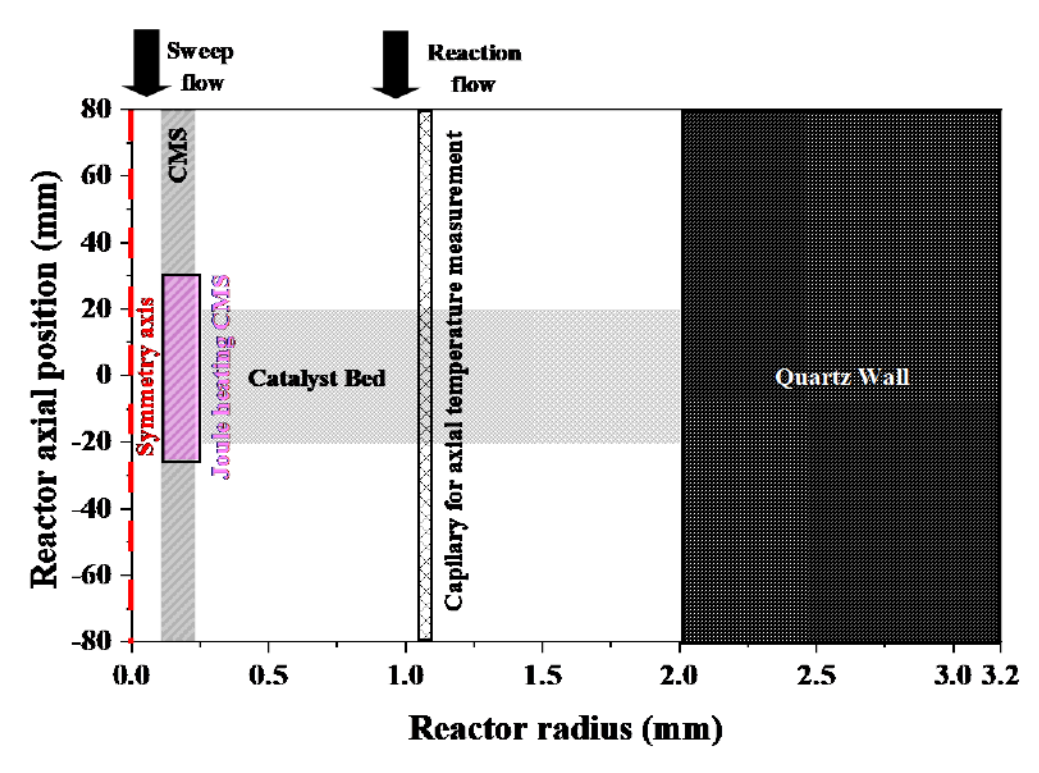


Figure S14. 2D axisymmetric geometry of joule heating membrane reactor cross-section. (Axial position 0 is the center of the reactor along the reactor and Radial position 0.0 is the center of the CMS hollow fiber.)

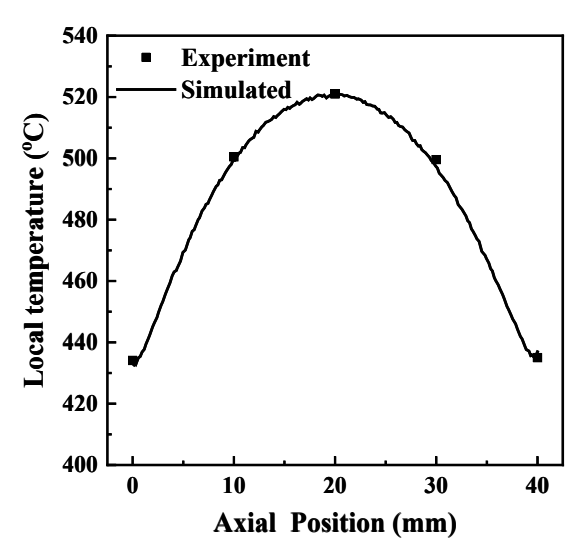


Figure S15. Simulated and experimentally measured axial temperature profile of catalyst bed at 1.08 mm radial position. Modeled reactor parameters: MR loaded with Pt-Zn/S1 catalyst, 10 mL min⁻¹ sweep gas flow rate, WSHV= 1.33 h⁻¹ (50 vol% C_3H_8 balanced with Ar), number of CMS fiber = 1.

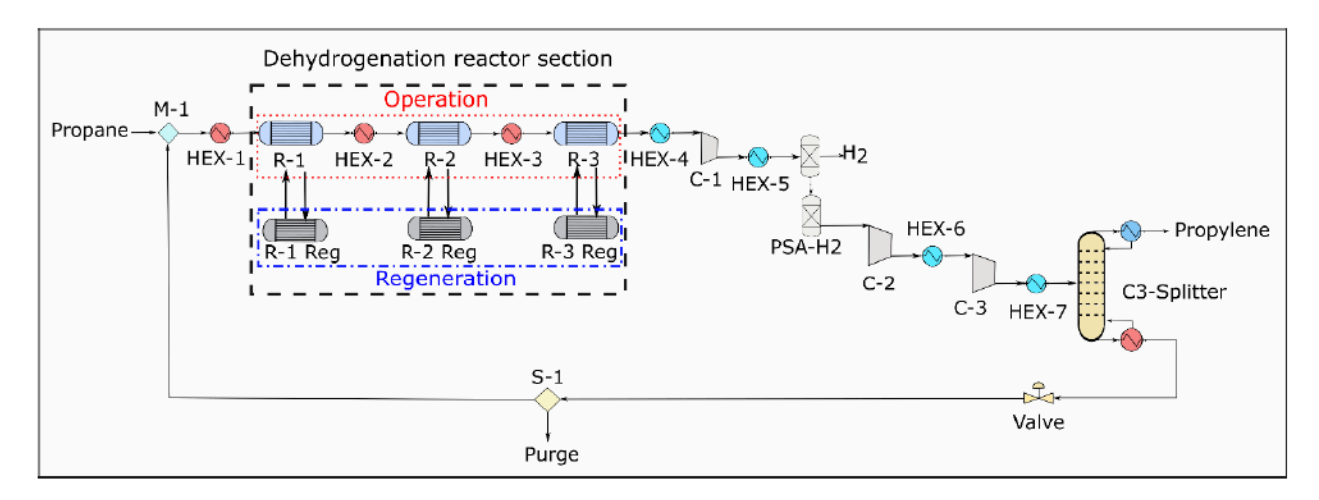


Figure S16. Flow diagram of Catofin process to produce propylene by propane dehydrogenation.

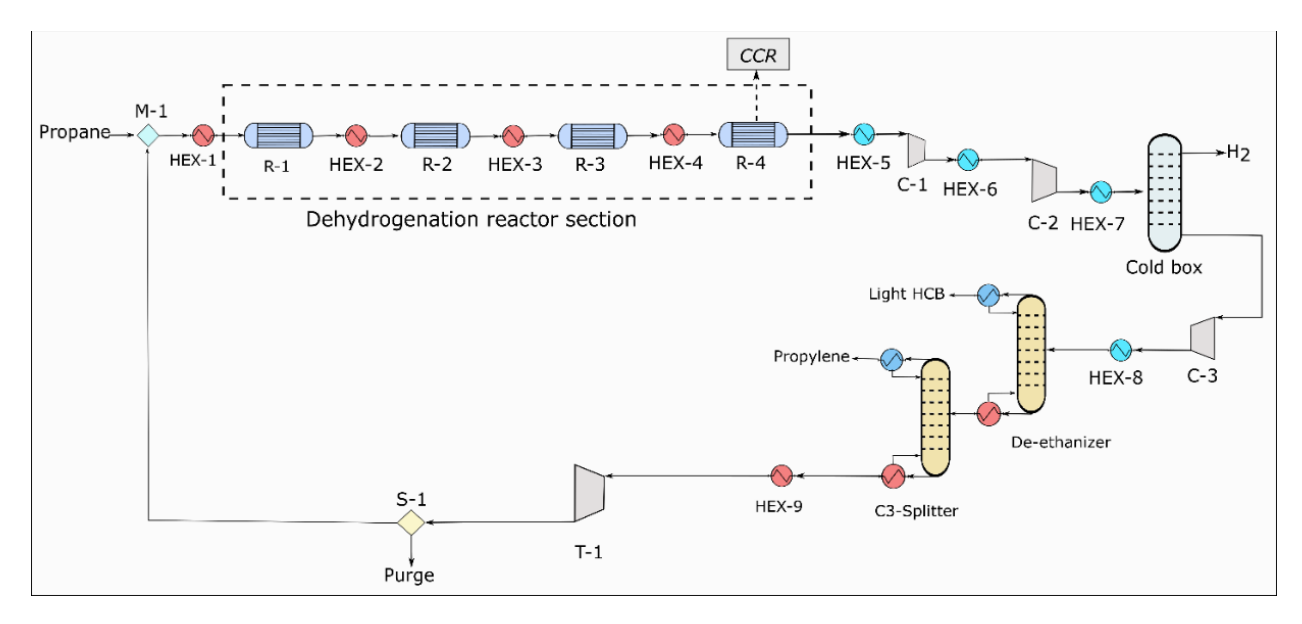


Figure S17. Flow diagram of PDH in Oleflex process to produce propylene by propane dehydrogenation.

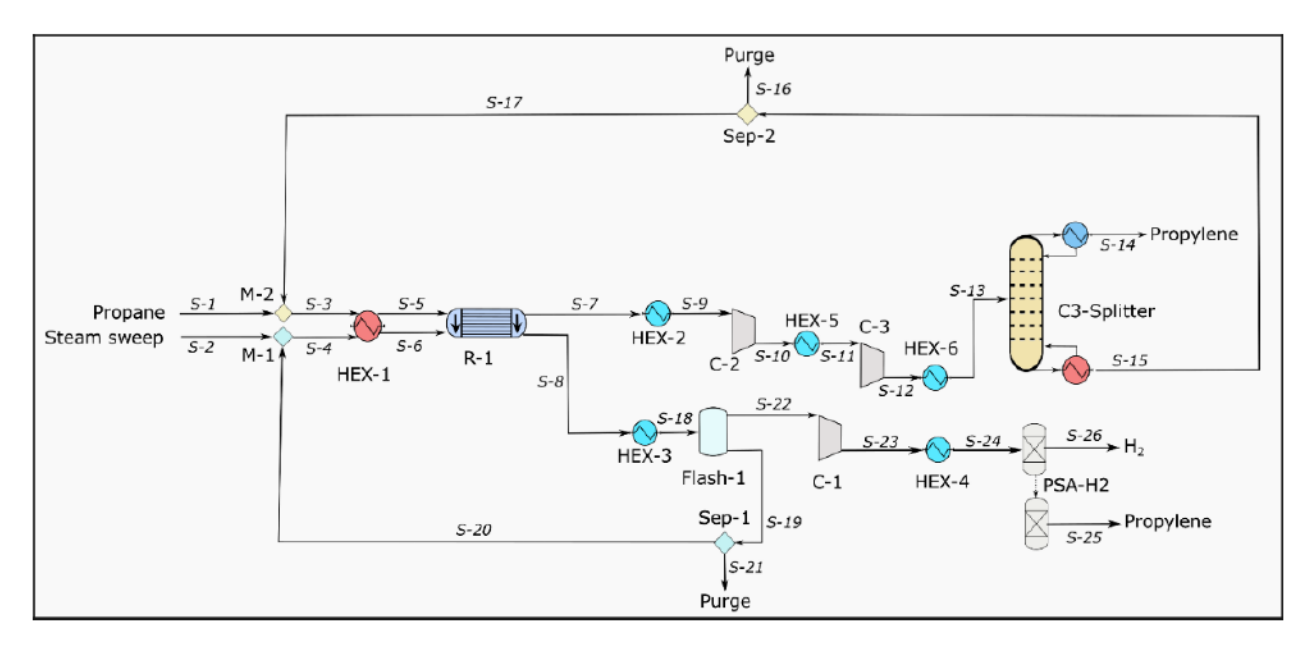


Figure S18. Flow diagram of PDH in the designed CMS membrane reactor to produce propylene from propane.

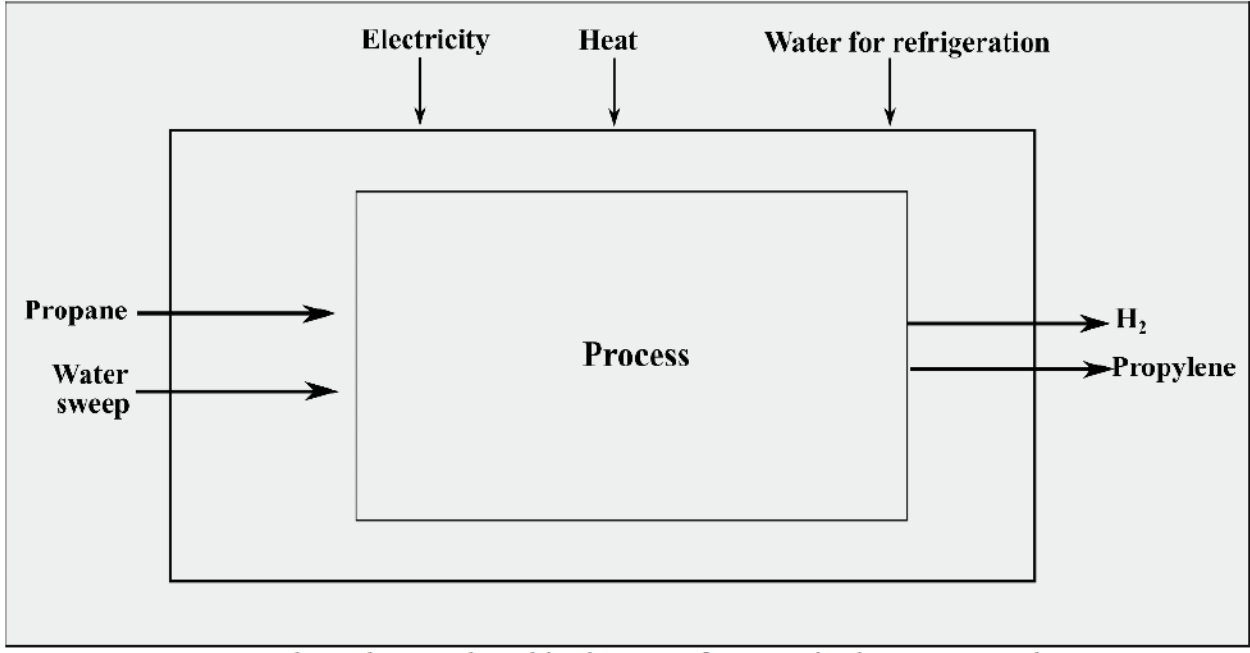


Figure S19. System's boundary analyzed in the LCA for PDH in the CMS membrane reactor.

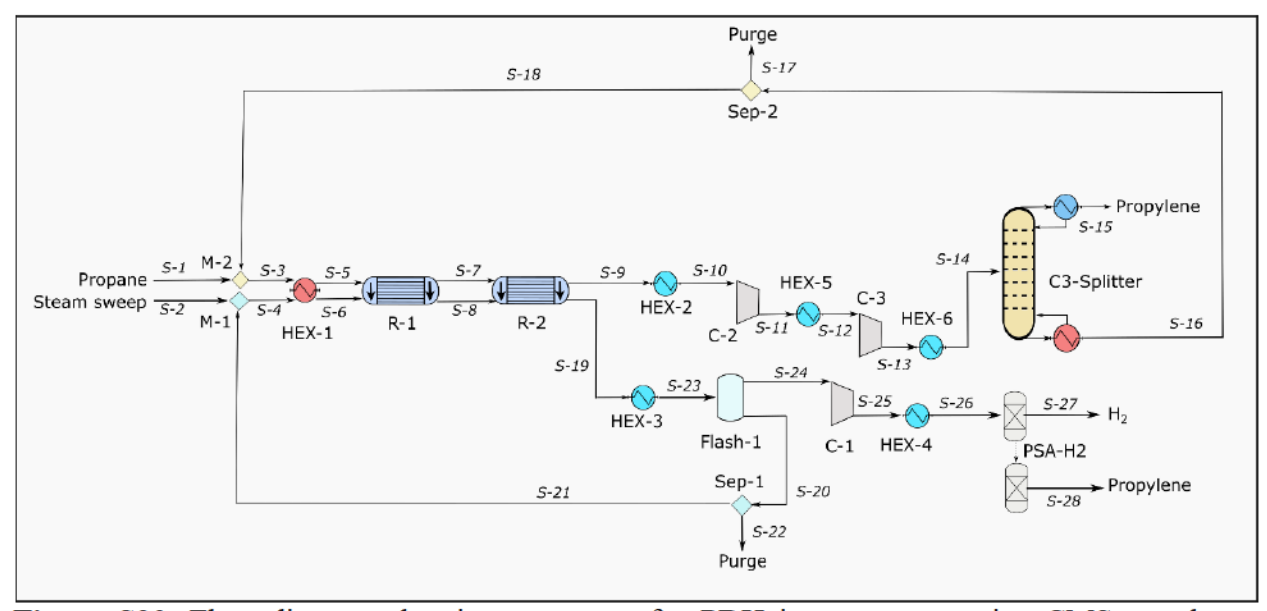


Figure S20. Flow diagram showing a process for PDH in two consecutive CMS membrane reactors.

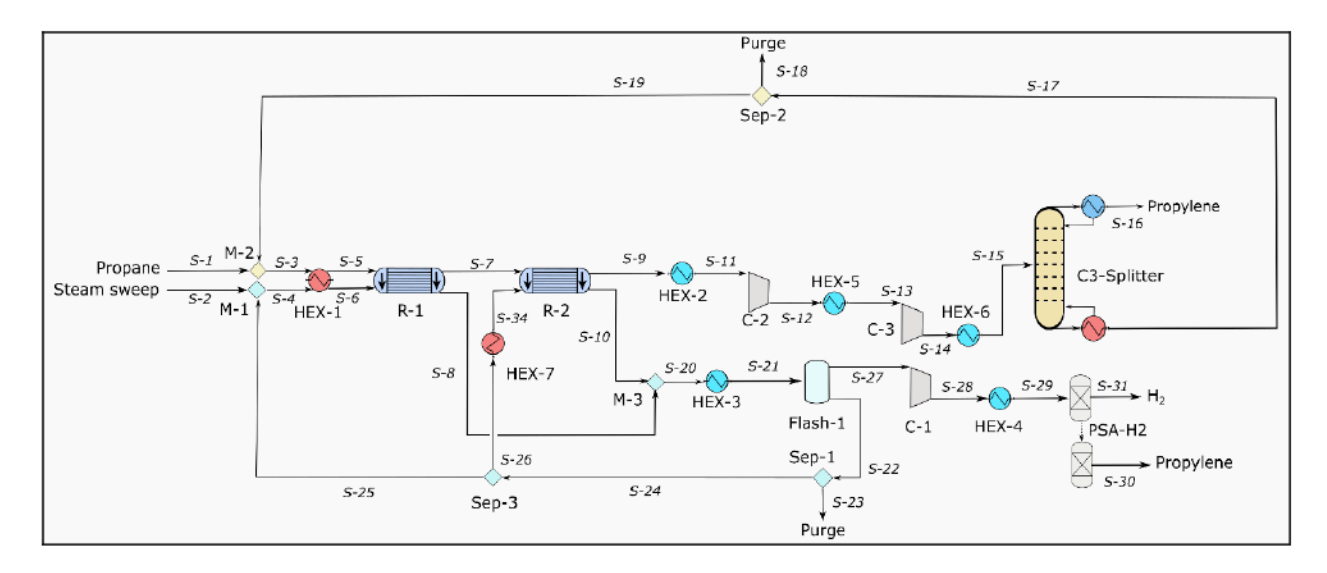


Figure S21. Flow diagram showing a process for PDH in the CMS membrane reactor split in 2 parts (R-1 and R-2) with intermediate fresh purge of sweep steam.

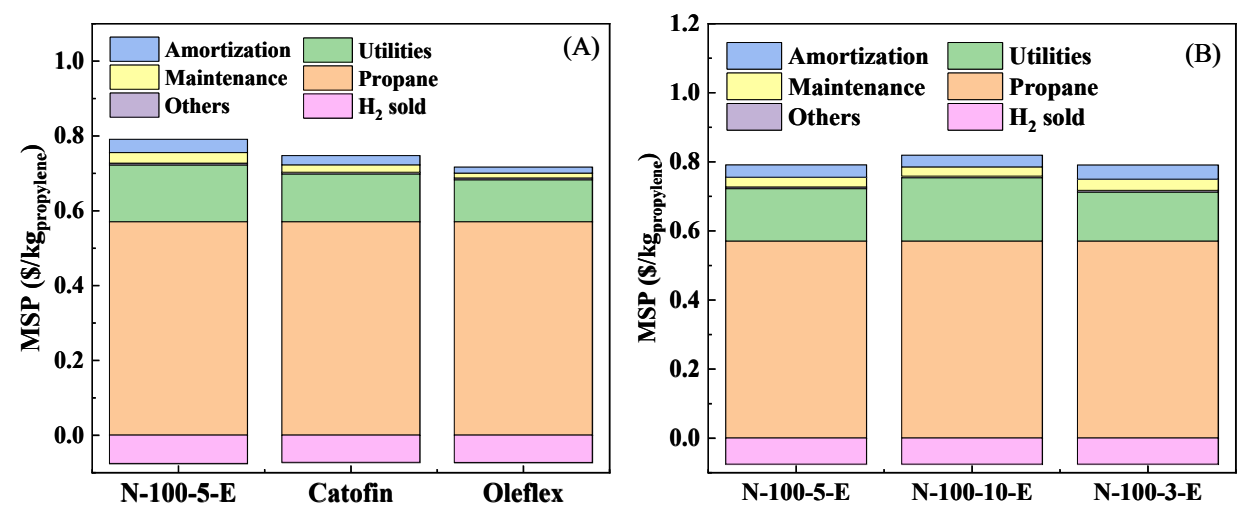


Figure S22. (A) Comparison of the contributions to MSP for PDH in CMS membrane reactor and State-of-the-art (Catofin and Oleflex) processes and (B) breakdown of cost contributors with different pinch temperature in the heat integration of the sweep stream for the process with the CMS membrane reactor. (N-100-5-E is used as the base case in sensitivity analysis of the simulated processes.) (N-100-5-E corresponds to the "grid" case in Fig. 4E-F.)

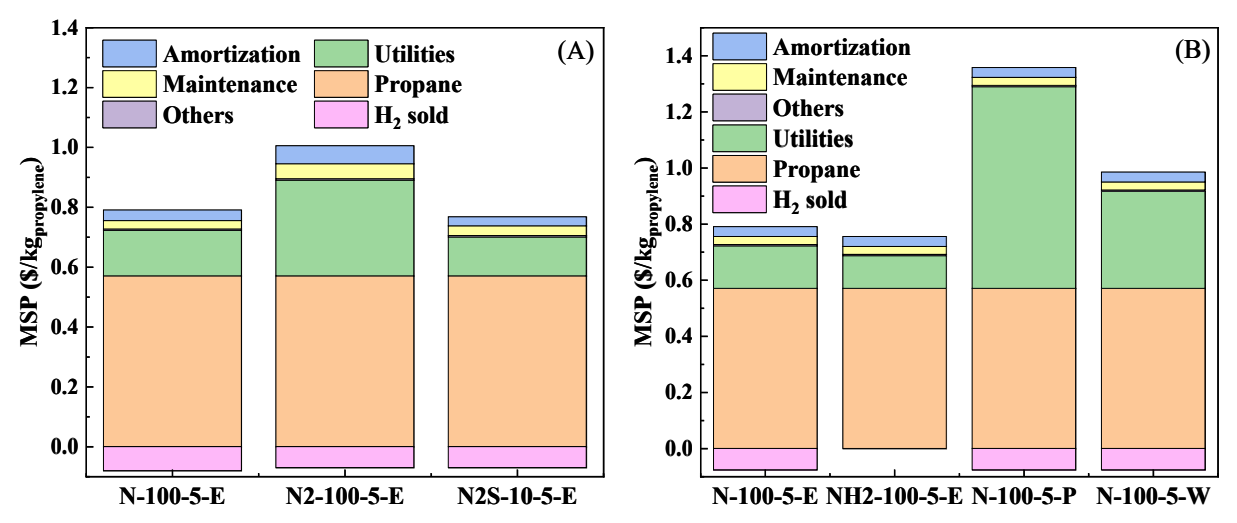


Figure S23. Breakdown of (A) cost contributors with different process alternatives and (B) breakdown of cost contributors with different energy sources for the CMS membrane reactor. (N-100-5-E corresponds to the "grid" case in Fig. 4E-F, NH2-100-5-E corresponds to the "grid+H₂" case in Fig. 4E-F, N-100-5-P corresponds to the "solar" case in Fig. 4E-F, and N-100-5-W corresponds to the "wind" case in Fig. 4E-F.)

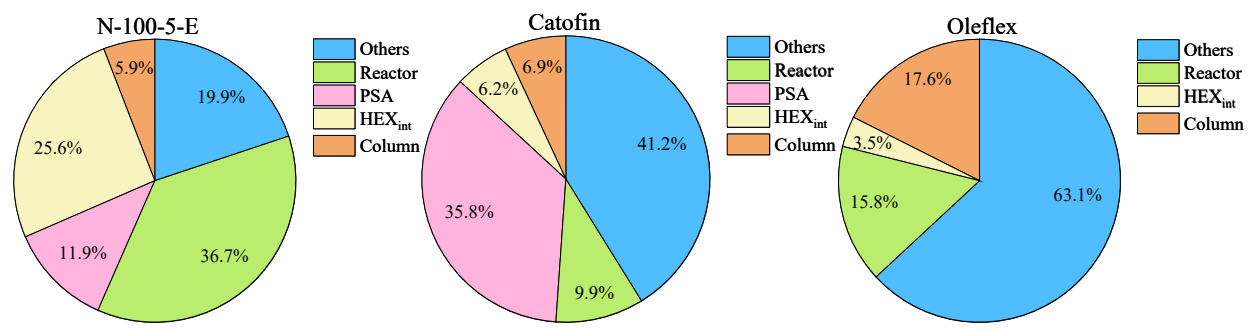


Figure S24. Breakdown of the CAPEX for the three processes (PDH in CMS membrane reactor and state-of-the-art (Catofin and Oleflex)) studied. (N-100-5-E corresponds to the "grid" case in Fig. 4E-F.)

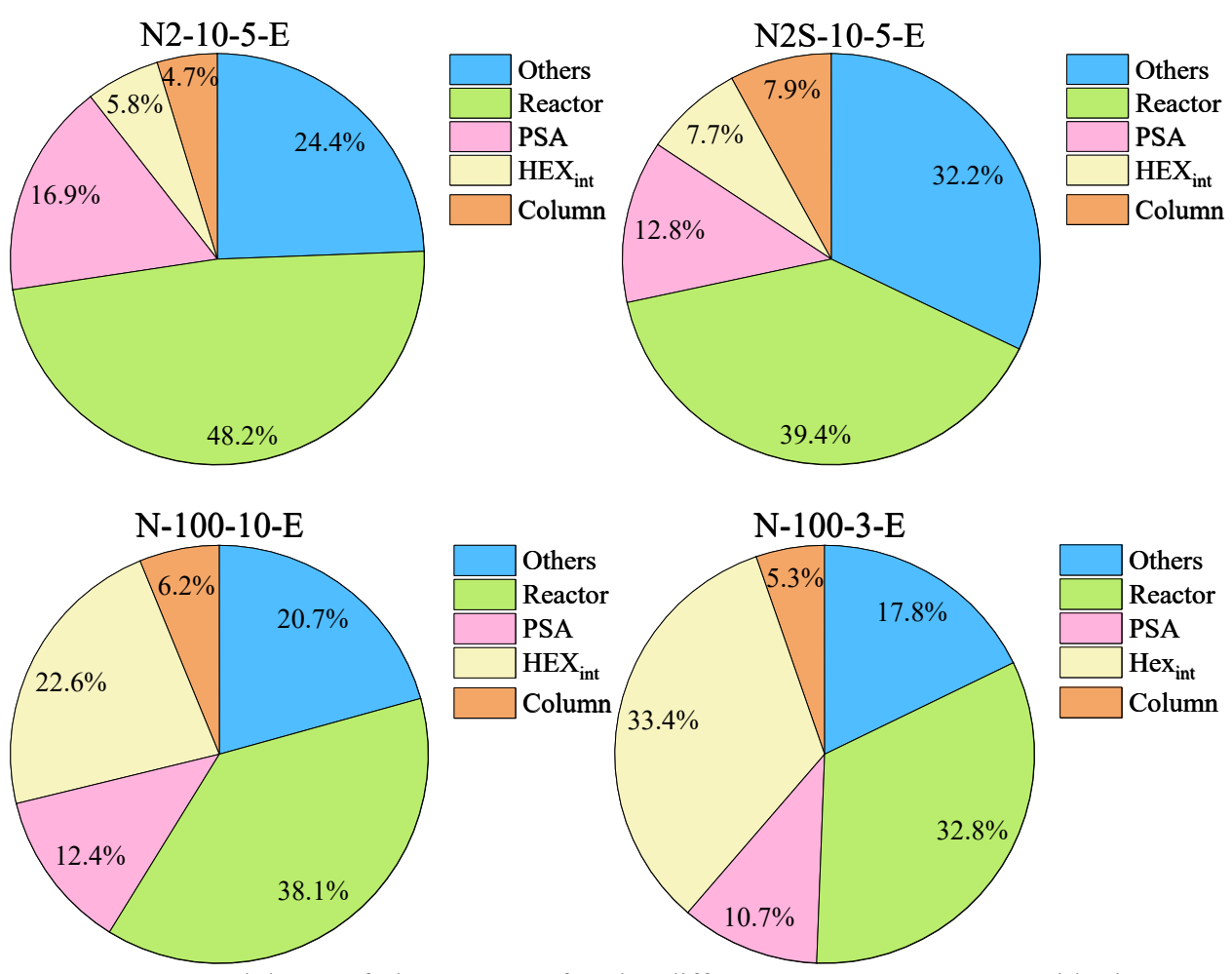


Figure S25. Breakdown of the CAPEX for the different process structures with the CMS membrane reactor and different temperatures in the pinch of the heat exchanger.

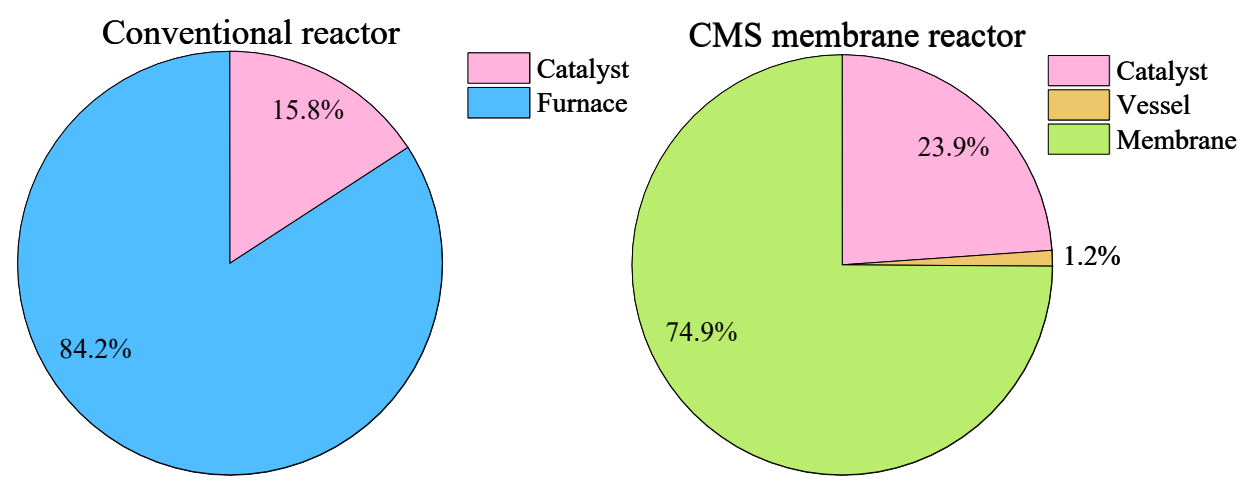


Figure S26. Breakdown of the CAPEX in the conventional PDH reactor versus the CMS membrane reactor in the present study.

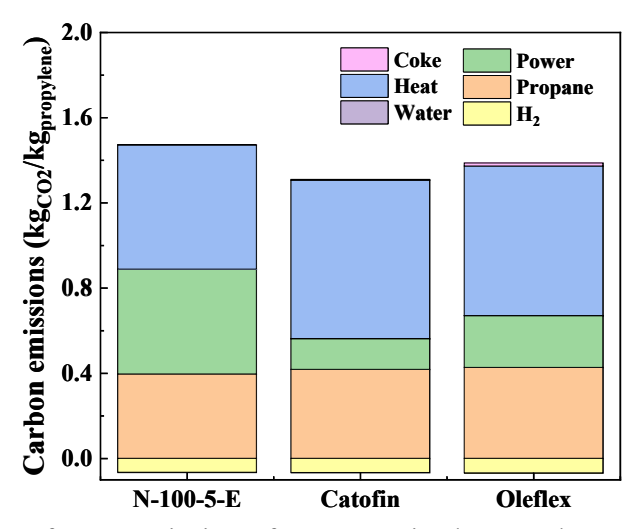


Figure S27. Breakdown of CO₂ emissions from PDH in the membrane reactor and the state-of-the-art processes. (N-100-5-E corresponds to the "grid" case in Fig. 4E-F.)

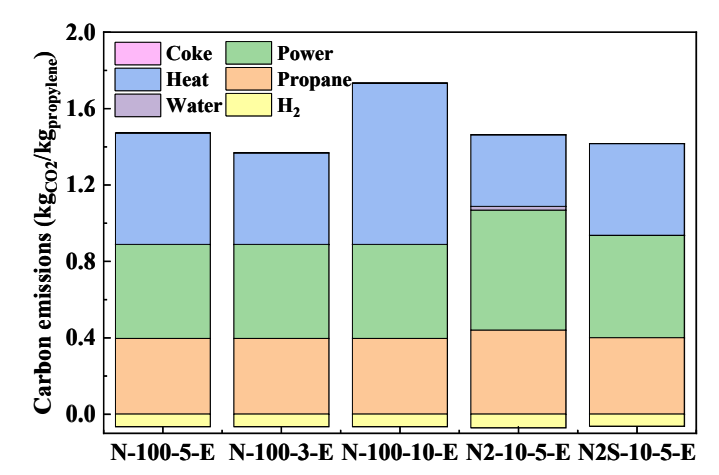


Figure S28. Breakdown of CO₂ emissions for different process alternatives with the CMS membrane reactor and pinch temperature in the sweep stream. (N-100-5-E corresponds to the "grid" case in Fig. 4E-F.)

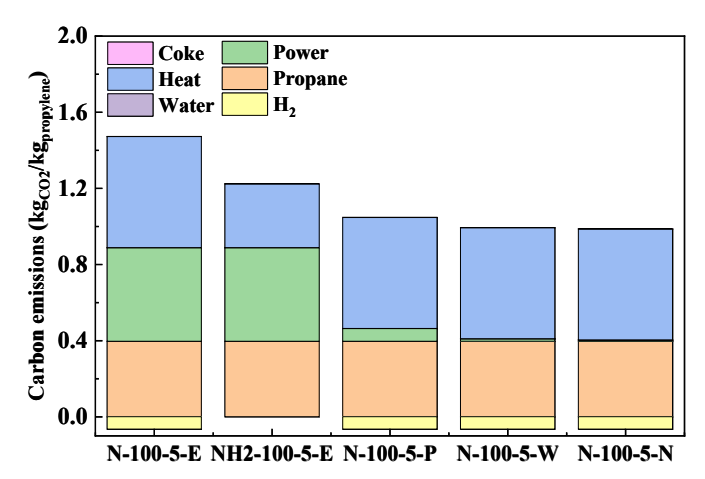


Figure S29. Breakdown of CO₂ emissions from PDH in membrane reactor with process heat from different energy sources. (N-100-5-E corresponds to the "grid" case in Fig. 4E-F, NH2-100-5-E corresponds to the "grid+H₂" in Fig. 4E-F, N-100-5-P corresponds to the "solar" case in Fig. 4E-F, N-100-5-W corresponds to the "wind" case in Fig. 4E-F, N-100-5-N corresponds to the "nuclear" case in Fig. 4F.)

Table S1. Spinning dope compositions of Matrimid® precursor hollow fibers⁸⁷.

Component	wt%
Matrimid® 5218	26.2
N-Methyl-pyrrolidone (NMP)	53.0
Tetrahydrofuran (THF)	5.9
Ethanol (EtOH)	14.9

Table S2. Spinning parameters of Matrimid® precursor hollow fibers.

Spinning parameter	Value
Spinning temperature (°C)	60
Quench bath temperature (°C)	50
Dope/bore fluid flow rate (mL·h ⁻¹)	180/60
Bore fluid composition (wt%)	90/10 (NMP/DI water)
Air gap height (cm)	10
Fiber take-up rate (m·min ⁻¹)	20

Table S3. Thermodynamic data at STP condition⁷ for equilibrium conversion calculations for propane and ethane dehydrogenation reactions.

Cas	$\Delta H_{\mathrm{f}}^{0}$	S_{f}^{0}	A	В	С	D
Gas	(kJ·mol ⁻¹)	(J·mol ⁻¹ ·K ⁻¹)	(J·mol ⁻¹ ·K ⁻¹)	(J·mol ⁻¹ ·K ⁻²)	$(J \cdot mol^{-1} \cdot K^{-3})$	(J·mol ⁻¹ ·K ⁻⁴)
C ₂ H ₆	-83.82	229.60	5.41	0.18	-6.94×10 ⁻⁵	8.71×10 ⁻⁹
C ₂ H ₄	52.51	219.32	3.81	0.16	-8.35×10 ⁻⁵	1.76×10 ⁻⁸
C ₃ H ₈	-104.68	269.91	-4.22	0.31	-1.59×10 ⁻⁴	3.22×10 ⁻⁸
C ₃ H ₆	19.71	266.90	3.71	0.23	-1.16×10 ⁻⁴	2.21×10 ⁻⁸
H ₂	0.00	131.00	27.14	0.01	-1.38×10 ⁻⁵	7.65×10 ⁻⁹

Table S4. Composition and porosity characteristics of catalyst materials.

	Composition			Textural property			
Sample	Si/Al ratio	Pt (wt%)	Zn (wt%)	Co (wt%)	Surface area ^b $(m^2 \cdot g^{-1})$	Total pore vol. ^c (cm ³ ·g ⁻¹)	Micropore vol. ^d (cm ³ ·g ⁻¹)
Pt-Zn/S1 ^a	3630	0.49	1.27	-	526	0.26	0.17
H-BEA	19	-	-	-	615	0.46	0.18
DeAl-BEA	2830	-	-	-	681	0.46	0.18
Co/DeAl- BEA	2830	-	-	3.04	663	0.44	0.17

^a Sample was pre-reduced, prior to the N_2 isotherm measurement. ^b Determined by Brunauer-Emmett-Teller (BET) method. ^c Total pore volume determined at the relative pressure of $p/p_0 = 0.95$. ^d Micropore volume determined by t-plot method.

Table S5. Experiments conducted for determination of kinetics and thermodynamic parameters in rate equation of PDH over Pt-Zn/S1 catalyst.

Experiment	Forward reaction				Backward reaction		
#	T	$p_{C_3H_8}$	$p_{ m H_2}$	$p_{C_3H_6}$	T	$p_{ m H_2}$	$p_{C_3H_6}$
	(°C)	(kPa)	(kPa)	(kPa)	(°C)	(kPa)	(kPa)
Exp. 1	350-400	25-75	0	0	-	-	-
Exp. 2	350-400	50	0-20	0	-	-	-
Exp. 3	400-435	25-45	0	2.5	-	-	-
Exp. 4	-	-	-	-	90-125	2.5	1.25-7.5

Table S6. Rate constant of forward reaction in dissociative propane adsorption (k_1^+) and desorption equilibrium constant of hydrogen species from the catalyst (K_4) in PDH.

Kinetic parameters	Temperature (°C)					
Kinetic parameters	350	365	375	400		
k_1^{+a} $(\text{mol} \cdot \text{s}^{-1} \cdot \text{mol}_{\text{Pt}}^{-1} \cdot \text{kPa}^{-1})$	1.079×10 ⁻³	1.679×10 ⁻³	2.187×10 ⁻³	4.003×10 ⁻³		
k_1^{+b} $(\text{mol}\cdot\text{s}^{-1}\cdot\text{mol}_{\text{Pt}}^{-1}\cdot\text{kPa}^{-1})$	1.242×10 ⁻³	1.797×10 ⁻³	2.431×10 ⁻³	4.333×10 ⁻³		
Avg k_1^+ $(\text{mol} \cdot \text{s}^{-1} \cdot \text{mol}_{P_t}^{-1} \cdot \text{kPa}^{-1})$	1.160×10 ⁻³	1.738×10 ⁻³	2.309×10 ⁻³	4.317×10 ⁻³		
K ₄ (kPa)	2.963	4.119	4.882	7.937		

^a Determined from Eq. S34 and Exp. 1. ^b Determined from Eq. S35 and Exp. 2. ^c Calculated by averaging k₁⁺ values from both Exp. 1 and Exp. 2.

Table S7. Rate constant of forward reaction in dissociative propane adsorption (k_1^+) extrapolated to higher temperatures and desorption equilibrium constant of propylene species from the catalyst (K_3) in PDH.

Kinetic parameters	Temperature (°C)					
Kinetic parameters	400	410	425	435		
$Avg k_1$ $(mol \cdot s^{-1} \cdot mol_{Pt}^{-1} \cdot kPa^{-1})$	4.119×10 ⁻³	5.304×10 ⁻³	7.437×10 ⁻³	9.243×10 ⁻³		
K ₃ (kPa)	49.927	51.862	53.406	54.239		

^a Calculated using the Arrhenius equation that was generated from the fitting of the average k₁⁺ in Table S6.

Table S8. Rate constant of backward reaction in dissociative propane adsorption (k_1^-) and reaction equilibrium constant (K_2) of Step (2) in proposed mechanism in PDH.

Kinetic parameters	Temperature (°C)					
Kinetic parameters	90	100	110	125		
K ₄ ^a (kPa)	3.156×10 ⁻⁴	5.684×10 ⁻⁴	9.929×10 ⁻⁴	2.174×10 ⁻³		
K ₃ ^a (kPa)	12.441	13.490	14.476	16.243		
	5.883×10 ⁻³	9.660×10 ⁻³	1.352×10 ⁻²	1.766×10 ⁻²		
K ₂ (dimensionless)	0.661	0.722	0.846	1.046		
k_{1}^{-} $(\text{mol} \cdot \text{s}^{-1} \cdot \text{mol}_{\text{pt}}^{-1})$	0.442	0.573	0.905	2.092		

^a Determined by the Van's Hoff Equations obtained from the fitting of the K₃ and K₄ measured from the Exps. 2 and 3 and data in Tables S6 and S7.

Table S9. Summary of activation energy and pre-exponential factor, and adsorption energy and pre-exponential factor for PDH over the Pt-Zn/S1 catalyst.

Kinetic parameters	ko ^a	Ea (kJ·mol ⁻¹)	K ₀ ^b	ΔH (kJ·mol ⁻¹)
$\begin{array}{c} k_1^+ \\ (\text{mol} \cdot \text{s}^{\text{-l}} \cdot \text{mol}_{\text{Pt}}^{\text{-l}} \cdot \text{kPa}^{\text{-l}}) \end{array}$	3.585×10 ⁴	89.301	-	-
$k_1^ (\text{mol} \cdot \text{s}^{-1} \cdot \text{mol}_{\text{Pt}}^{-1})$	5.43×10 ⁴	35.317	-	-
K ₂ (dimensionless)	-	-	1.586×10^2	16.584
K ₃ (kPa)	-	-	2.575×10 ²	9.145
K ₄ (kPa)	-	-	1.076×10 ⁶	66.245

^a Refer to k₁⁺ and k₁⁻ for units of k₀; ^b Refer to K₂, K₃ and K₄ for units of K₀.

 Table S10.
 Experimental studies of non-oxidative propane dehydrogenation membrane reactors.

Membrane material (geometry)	Catalyst	Feed Composition (vol%)	T (°C)	Equil. Conv. (%)	C ₃ H ₈ Conv. (%)	C ₃ H ₆ Sel. (%)	C ₃ H ₆ Yield (%)	Conv./Equil. Conv.	Stability (h)	Ref.
CMS (hollow fiber)	Pt-Zn/S1	50%C ₃ H ₈ /50%Ar	450	12.4	36.6	95.3	34.9	2.95	112.5	This work
Pd-Ag/vycor glass (tubular)	Pt/Al ₂ O ₃	50%C ₃ H ₈ /50%N ₂	400	5.3	21.0	-	-	4.00	-	19
Pd/Al ₂ O ₃ (tubular)	Pt/Al ₂ O ₃	50%C ₃ H ₈ /50%N ₂	570	40.0	47.0	-	-	1.18	-	19
Pd-silica/ Al ₂ O ₃ (tubular)	Pt/Al ₂ O ₃	50%C ₃ H ₈ /50%N ₂	437- 463	-	11.0- 19.0	-	-	-	-	19
Pd-Ag/Al ₂ O ₃ (tubular)	Pt/Al ₂ O ₃	50%C ₃ H ₈ /50%N ₂	437- 468	-	12.0- 27.5	>97.0	17.9- 39.8	-	-	19
Pd-Ag/Al ₂ O ₃ (tubular)	Cr ₂ O ₃ /Al ₂ O ₃	100% C ₃ H ₈	500	18.0	-	85.0- 95.0	36.0	2.10-2.35	7.0	20
Pd/ Al ₂ O ₃ (tubular)	-	C ₃ H ₈ , H ₂ , N ₂ mixture	560	30.2	35.4	-	26.1	1.17	1.0-2.0	21
Pd stainless steel (tubular)	-	C ₃ H ₈ , H ₂ , N ₂ mixture	560	30.2	42.0	-	-	1.39	1.0-2.0	21
Pd-Ag alloy (tubular)	Pt-Sn/ Al ₂ O ₃ /silica	100% C ₃ H ₈	550	24.0	34.0	79.0	26.9	1.42	1.7	22
Pd-Ag alloy (tubular)	Pt-Sn/ Al ₂ O ₃ /silica	100% C ₃ H ₈	550	23.0	30.0	94.0	10.2	1.30	16.7	23
Pd/Al ₂ O ₃ (tubular)	Pt-K-Sn/ Al ₂ O ₃	20%C ₃ H ₈ /80%N ₂	350- 550	3.6- 34.2	11.0- 72.0	94.5- 72.0	10.4- 52.8	2.10-3.06	-	24
Pd-Ag/Al ₂ O ₃ (hollow fiber)	Pt/Al ₂ O ₃	5%C ₃ H ₈ /4.5%H ₂ / 90.5%N ₂	450	22.0	42.1	-	-	1.91	0.8	25
Pd/Al ₂ O ₃ (hollow fiber)	Pt/SBA-15	5%C ₃ H ₈ /4.5%H ₂ / 90.5%N ₂	500	-	48.7	18.0	8.8	-	2.0	26
Pd-Ag foil (disk)	Cr ₂ O ₃ /Al ₂ O ₃	100% C ₃ H ₈	520	-	35.0	-	-	-	2.0	27
Pd/Al ₂ O ₃ (hollow fiber)	Pt-Sn/ MgAl ₂ O ₄	100% C ₃ H ₈	500	30.2	17.7	90.3	16.0	0.59	1.7	15

Table S10. Experimental studies of non-oxidative propane dehydrogenation membrane reactors. (Continued)

Membrane material (geometry)	Catalyst	Feed Composition (vol%)	T (°C)	Equil. Conv. (%)	C ₃ H ₈ Conv. (%)	C ₃ H ₆ Sel. (%)	C ₃ H ₆ Yield (%)	Conv./Equil. Conv.	Stability (h)	Ref.
Pd-Ag/stainless steel (tubular)	Pt-Sn/ MgAl ₂ O ₄	50%C ₃ H ₈ /50%Ar	575	49.7	33.0	78.0	25.5	0.66	2.0	28
Pd-Ag alloy (tubular)	Supported Pt	$100\% \ C_3H_8$	525	24.0	-	-	40.0	-	2.0	29
SAPO-34/Al ₂ O ₃ (tubular)	Na ₂ O- Cr ₂ O ₃ /Al ₂ O ₃	$100\% \ C_3H_8$	600	48.0	75.0	77.0	58.0	1.56	16.0	17
LTA-coated Pd/ Al ₂ O ₃ (hollow fiber)	Cr/Al ₂ O ₃	$30\%C_3H_8/70\%N_2$	600	66.6	47.0	93.0	43.7	0.71	0.3	30
Hybrid MFI-Pt/ Al ₂ O ₃ (disk)	Pt cluster	100% C ₃ H ₈	600	48.0	23.0	32.5	7.2	0.48	5.0	18
Silicate/Al ₂ O ₃ (disk)	Pt/Al ₂ O ₃	$100\% C_3H_8$	600 (5 atm)	23.0	49.0	97.0	47.0	2.13	12.0	16
Silica/Al ₂ O ₃ (tubular)	Pt/aluminosili cate	100% C ₃ H ₈	550	32.0	40.8	>97.0	39.6	1.27	-	31
Silica/Al ₂ O ₃ (tubular)	Cr ₂ O ₃ /Al ₂ O ₃	100% C ₃ H ₈	500	18.0	23.8	89.0	21.2	1.32	8.0	32
Silica/Al ₂ O ₃ (tubular)	Cr ₂ O ₃ /Al ₂ O ₃	$100\% C_3H_8$	535	27.1	32.0- 34.0	85.0- 90.0	27.2- 30.6	1.22	10.0	33
Silica/Al ₂ O ₃ (tubular)	Cr ₂ O ₃ /Al ₂ O ₃	$33.3\%C_3H_8/66.7\%N_2$	535	40.0	49.0	75.0	36.8	1.23	5.8	34
Silica/Al ₂ O ₃ (tubular)	Pt-Sn/Al ₂ O ₃	$60\%C_3H_8/40\%N_2$	500	22.0	27.5	80.0	22.0	1.25	4.2	34
Silica/Al ₂ O ₃ (tubular)	Pt/Al ₂ O ₃	$100\% C_3H_8$	600	48.0	53.0	68.5	40.8	1.10	4.2	35
Al ₂ O ₃ (tubular)	Cr ₂ O ₃ /Al ₂ O ₃	100% C ₃ H ₈	575	-	58.7	90.0	52.8	1.45	2.0	36
Al ₂ O ₃ (tubular)	Pt-Mg/ Al ₂ O ₃	66.6%C ₃ H ₈ / 16.7%C ₃ H ₆ /16.7%H ₂	520-600	1.8- 34.0	3.5- 70.0	95.0- 73.0	3.5- 52.2	1.94-2.06	-	37
Al ₂ O ₃ (tubular)	Pt-Mg/ Al ₂ O ₃	80%C ₃ H ₈ /20%N ₂	480-625	8.0- 78.0	10.0- 90.0	99.0- 68.0	9.9- 61.2	1.15-1.25	-	38

Table S10. Experimental studies of non-oxidative propane dehydrogenation membrane reactors. (Continued)

Membrane material (geometry)	Catalyst	Feed Composition (vol%)	T (°C)	Equil. Conv. (%)	C ₃ H ₈ Conv. (%)	C ₃ H ₆ Sel. (%)	C ₃ H ₆ Yield (%)	Conv./Equil. Conv.	Stability (h)	Ref.
Mo/Al ₂ O ₃ (tubular)	Mo	80%C ₃ H ₈ /20%N ₂	600	45.0	28.0	62.0	17.4	0.62	-	39
Mo/carbon (tubular)	Mo	80%C ₃ H ₈ /20%N ₂	600	45.0	40.0	74.0	29.6	0.89	-	39
Ni/Al ₂ O ₃ (tubular)	Pt/Al ₂ O ₃	20%C ₃ H ₈ /20%H ₂ / 60%N ₂	500	-	40.8	63.7	26.0	-	1.0	40

Table S11. Experimental studies for non-oxidative ethane dehydrogenation membrane reactors.

Membrane material (geometry)	Catalyst	Feed Composition (vol%)	T (°C)	Equil. Conv. (%)	C ₂ H ₆ Conv. (%)	C ₂ H ₄ Sel. (%)	C ₂ H ₄ Yield (%)	Conv./Equil. Conv.	Stability (h)	Ref.
CMS (hollow fiber)	Co/BEA	50%C ₂ H ₆ /50%Ar	500	6.7	16.5	81.3	13.5	2.46	110.2	This work
Pd-Ag/vycor glass (tubular)	Pd/Al ₂ O ₃	$50\%C_2H_6/50\%N_2$	387	2.2	18.0	-	-	8.18	-	41
Ceramic Al ₂ O ₃ (tubular)	Pt/Al ₂ O ₃	-	500	2.0	12.0	>96.0	11.5	6.00	-	42
Ceramic Al ₂ O ₃ (tubular)	Pt/Al ₂ O ₃	-	600	45.0	22.0	>96.0	43.2	2.05		42
Al ₂ O ₃ (tubular)	Pt/Al ₂ O ₃	90%C ₂ H ₆ /10%Ar	500	2.0	4.0	99.0	10.1	2.00	-	43
Al ₂ O ₃ (tubular)	Pt/Al ₂ O ₃	90%C ₂ H ₆ /10%Ar	550	8.5	16.0	99.0	15.8	1.88	-	43
Al ₂ O ₃ (tubular)	Pt/Al ₂ O ₃	90%C ₂ H ₆ /10%Ar	600	18.0	35.0	99.0	34.7	1.94	-	43
Mordenite zeolite (disk)	Pt-Sn/Al ₂ O ₃	100% C ₂ H ₆	500	4.9	5.2	94.0	4.9	1.06	2.0	44
Mordenite zeolite (disk)	Pt-Sn/Al ₂ O ₃	100% C ₂ H ₆	550	9.2	10.5	93.7	9.8	1.14	-	44
MFI zeolite/Al ₂ O ₃ (disk)	Pt/Al ₂ O ₃	100% C ₂ H ₆	500	4.5	15.0	79.0	11.9	3.33	-	45
MFI zeolite/Al ₂ O ₃ (disk)	Pt/Al ₂ O ₃	100% C ₂ H ₆	550	8.0	20.0	85	17.0	2.50		45
MFI zeolite/Al ₂ O ₃ (disk)	Pt/Al ₂ O ₃	100% C ₂ H ₆	600	14.5	25	90	22.6	1.72		45
Pd/ Nb-Ta alloy tube (tubular)	Re/HZSM-5	100% C ₂ H ₆	520	6.0	18.3	47.7	8.7	3.05	4.0	46
Silica/Al ₂ O ₃ (tubular)	Cr/ZSM-5	20%C ₂ H ₆ /80%Ar	450	4.0	4.0	99.0	3.9	1.00	-	47
Silica/Al ₂ O ₃ (tubular)	Cr/ZSM-5	20%C ₂ H ₆ /80%Ar	500	10.0	10.0	99.0	9.0	1.00		47

Table S11. Experimental studies for non-oxidative ethane dehydrogenation membrane reactors (continued).

Membrane material (geometry)	Catalyst	Feed Composition (vol%)	T (°C)	Equil. Conv. (%)	C ₂ H ₆ Conv. (%)	C ₂ H ₄ Sel. (%)	C ₂ H ₄ Yield (%)	Conv./Equil. Conv.	Stability (h)	Ref.
Silica/Al ₂ O ₃ (tubular)	Cr/ZSM-5	20%C ₂ H ₆ /80%Ar	550	19.4	25.0	99.0	24.8	1.28	-	47
Silica/Al ₂ O ₃ (tubular)	Cr ₂ O ₃ /Al ₂ O ₃	$20\%C_2H_6/80\%N_2$	555	18.0	18.0	87.0	15.7	1.00	2.2	48
Silica/Al ₂ O ₃ (tubular)	Cr ₂ O ₃ /Al ₂ O ₃	$20\%C_2H_6/80\%N_2$	600	31.0	28.0	83.0	23.2	0.90	-	48
Al ₂ O ₃ (tubular)	Pd/Al ₂ O ₃	10% ethane, 5% H ₂ , 85% Ar	500	4.0	7.5	-	-	1.88	-	49
Al ₂ O ₃ (tubular)	Pt/Al ₂ O ₃	10% ethane, 5% H ₂ , 85% Ar	525	7.0	12.5	-	-	1.79	-	49
Al ₂ O ₃ (tubular)	Pt/Al ₂ O ₃	10% ethane, 5% H ₂ , 85% Ar	550	12.0	16.5	-	-	1.38	-	49

Table S12. CMS membrane reactor characteristics used in the process model. Values are for a reference of 1 kiloton per year (1 kt/y or 0.72 mol/s) of propane processed in the reactor.

Characteristics in CMS membrane reactor	Value
Conversion (%)	45.6
Mass of catalyst (kg)	67.5
Membrane area (m ²)	5800

Table S13. Estimation for catalyst cost for PDH in the CMS membrane reactor.

Reagent	Price (\$/kg)	Reference
PtCl ₂	5000	73
Ethylenediamine	4.39	default in CatCost tool ⁶⁵
ТРАОН	25	74
TEOS	5	75
Zn(acac)·2H ₂ O	150	76

Table S14. Values for the temperatures of heat and cold streams for energy integration.

Temperature in stream	Value (°C)
$T_{inHEX1} = T_{c in}$	25
T _{c out}	$\frac{Q_{int}}{\overline{c_{p_{cold}}} \cdot F_{tot cold}} + T_{c in}$
T _{h in} =T _{reaction out}	450
$T_{\text{h out}} = T_{\text{c in}} + \Delta T_{\text{pinch}}$	30

Table S15. Summary of characteristics of reactors in process shown in Figure S20.

Characteristics	Reactor1a	Reactor2 ^a	
Cumulative conversion (%)	31	48.1	
Mass of catalyst (kg)	67.5	67.5	
Membrane area (m ²)	5800	5800	

^a Steam/propane flow rate ratio is 10. A reference of 1 kt/y (or 0.72 mol/s) of propane processed in the reactor.

Table S16. Summary of reactor characteristics in Figure S21.

Characteristics	Reactor1a	Reactor2 ^a
Cumulative conversion (%)	24.0	37.4
Mass of catalyst (kg)	33.75	33.75
Membrane area (m ²)	2900	2900

^a Steam/propane flow rate ratio is 10 and mass is equivalent to single reactor. A reference of 1 kt/y or 0.72 mol/s of propane processed in the reactor.

Table S17. Summary of case studies and acronyms for identifying all the cases.

ACRONYM	Process	Steam/Propane flow rate ratio	Pinch T (°C)	Electricity source
Catofin	Catofin	-	5	Electricity (only compressors)
Oleflex	Oleflex	-	5	Electricity (only compressors)
N-100-5-E ^a	New	100	5	Electricity
N2-10-5-E	2 reactors	10	5	Electricity
N-100-10-E	New	100	10	Electricity
N-100-3-E	New	100	3	Electricity
N2S-10-5-E	Split in 2 steps	10	5	Electricity
NH2-100-5-E ^b	Integration with H ₂	100	5	Electricity
N-100-5-P ^c	New	100	5	Photovoltaic
N-100-5-W ^d	New	100	5	Wind power
N-100-5-N ^e	New	100	5	Nuclear

^a corresponds to the "grid" case in Fig. 4E-F. ^b corresponds to the "grid+H₂" case in Fig. 4E-F. ^c corresponds to the "solar" case in Fig. 4E-F. ^d corresponds to the "wind" case in Fig. 4E-F. ^e corresponds to the "nuclear" case in Fig. 4F.

Table S18. Summary of the plant's MSP of propylene and the CAPEX for different alternatives in all case studies for PDH.

ACRONYM	MSP of Propylene (\$/kg)	CAPEX plant (MM\$)
Catofin	0.6744	176
Oleflex	0.6558	112
N-100-5-E ^a	0.7152	286
N2-10-5-E	0.9396	377
N-100-10-E	0.7432	275
N-100-3-E	0.7147	320
N2S-10-5-E	0.6981	266
NH2-100-5-E ^b *	0.7557	286
N-100-5-P ^c *	1.2825	286
N-100-5-W ^d *	0.9097	286
N-100-5-N e*	0.7152	286

^a corresponds to the "grid" case in Fig. 4E-F. ^b corresponds to the "grid+H₂" case in Fig. 4E-F. ^c corresponds to the "solar" case in Fig. 4E-F. ^d corresponds to the "wind" case in Fig. 4E-F. ^e corresponds to the "nuclear" case in Fig. 4F. *For cases where alternative sources are considered for energy, and the CAPEX is associated to an external supplier.

Table S19. Energy requirements per section of the PDH process in CMS membrane reactor and the state-of-the-art processes.

Section	CMS membrane reactor	Catofin	Oleflex
Depropanizer (cal/s)	1.61×10^7	1.86×10^7	1.62×10^7
Others (cal/s)	1.36×10 ⁷	1.01×10 ⁷	1.03×10^7
Total heat (cal/s)	2.97×10^{7}	2.87×10^7	2.65×10^7
Electricity for compressors (kW)	10687	14981	16053

Table S20. Emissions of different process alternatives.

Indicator ^a	N-100-5-E ^b	Catofin	Oleflex	N2-100-5-E	2S-100-5-E
Acid.	0.185	0.158	0.160	0.205	0.187
Ecotox.	0.244	0.231	0.233	0.271	0.244
Eutroph.	3.37×10 ⁻⁵	2.53×10 ⁻⁵	2.33×10 ⁻⁵	3.70×10 ⁻⁵	3.74×10 ⁻⁵
GW	1.407	1.244	1.319	1.392	1.353
Ozone Dep.	1.20×10 ⁻⁸	5.70×10 ⁻⁹	7.23×10 ⁻¹⁰	-3.91×10 ⁻⁹	7.88×10 ⁻⁹
Photox.	9.14×10 ⁻⁴	7.60×10 ⁻⁴	7.50×10 ⁻⁴	9.63×10 ⁻⁴	9.01×10 ⁻⁴

^a Acid. corresponds to the acidification potential in (mols of H⁺ Eq./kg_{lubricant}), Ecotox. corresponds to the ecotoxicity potential in (kg 2,4-D Eq. /kg_{lubricant}) Eutroph. corresponds to the eutrophication potential in (kgN/kg_{lubricant}), GW corresponds to the global warming potential in (kg CO₂ Eq. /kg_{lubricant}), Ozone Dep. corresponds to the ozone depletion in (kg CFC-11-Eq/ kg_{lubricant}), Photox. corresponds to the photochemical oxidation potential in (kg NO_x-Eq./ kg_{lubricant}). ^b corresponds to the "grid" case in Fig. 4E-F.

Table S21. Effect of the pinch temperature in the integration of the Sweep stream in the membrane reactor on the CO_2 emissions.

Indicator	N-100-5-E ^a	N-100-3-E	N-100-10-E
Acid.	0.185	0.179	0.198
Ecotox.	0.244	0.237	0.260
Eutroph.	3.37×10 ⁻⁵	2.94×10 ⁻⁵	4.44×10 ⁻⁵
GW	1.407	1.302	1.667
Ozone Dep.	1.20×10 ⁻⁸	2.43×10 ⁻⁹	3.60×10 ⁻⁸
Photox.	9.14×10 ⁻⁴	8.55×10 ⁻⁴	1.06×10 ⁻³

^a corresponds to the "grid" case in Fig. 4E-F.

Table S22. Effect of the electricity source on CO₂ emissions from PDH in the membrane reactor.

Indicator	N-100-5-E ^a	NH2-100-5-E ^b	N-100-5-P ^c	N-100-5-W ^d	N-100-5-N ^e
Acid.	0.185	0.206	0.156	0.139	0.138
Ecotox.	0.244	0.246	0.274	0.220	0.308
Eutroph.	3.37×10 ⁻⁵	1.49×10 ⁻⁴	4.28×10 ⁻⁵	1.64×10 ⁻⁵	1.58×10 ⁻⁵
GW	1.407	1.224	1.059	1.005	0.999
Ozone Dep.	1.20×10 ⁻⁸	6.60×10 ⁻⁸	-4.15×10 ⁻⁹	-1.11×10 ⁻⁸	-1.13×10 ⁻⁸
Photox.	9.14×10 ⁻⁴	9.94×10 ⁻⁴	7.73×10 ⁻⁴	6.35×10 ⁻⁴	6.30×10 ⁻⁴

^a corresponds to the "grid" case in Fig. 4E-F. ^b corresponds to the "grid+H₂" case in Fig. 4E-F. ^c corresponds to the "solar" case in Fig. 4E-F. ^d corresponds to the "wind" case in Fig. 4E-F. ^e corresponds to the "nuclear" caes in Fig. 4F.

Table S23. Comparison of CO₂ emissions from PDH in the membrane reactor versus the Catofin process.

Case	Change in CO ₂ emissions vs Catofin (%)		
Catofin	-		
Oleflex	6.03		
N-100-5-E ^a	13.09		
N2-10-5-E	11.89		
N-100-10-E	34.04		
N-100-3-E	4.72		
N2S-10-5-E	8.79		
NH2-100-5-E ^b	-1.61		
N-100-5-P ^c	-14.87		
N-100-5-W ^d	-19.18		
N-100-5-N ^e	-19.69		

^a corresponds to the "grid" case in Fig. 4E-F. ^b corresponds to the "grid+H₂" case in Fig. 4E-F. ^c corresponds to the "solar" case in Fig. 4E-F. ^d corresponds to the "wind" case in Fig. 4E-F. ^e corresponds to the "nuclear" case in Fig. 4F.

References:

- 1. Harris, J.W., Cordon, M.J., Di Iorio, J.R., Vega-Vila, J.C., Ribeiro, F.H., and Gounder, R. (2016). Titration and quantification of open and closed Lewis acid sites in Sn-Beta zeolites that catalyze glucose isomerization. Journal of Catalysis 335, 141-154. https://doi.org/10.1016/j.jcat.2015.12.024.
- 2. Vu, D.Q., Koros, W.J., and Miller, S.J. (2002). High Pressure CO2/CH4 Separation Using Carbon Molecular Sieve Hollow Fiber Membranes. Industrial & Engineering Chemistry Research *41*, 367-380. 10.1021/ie010119w.
- 3. Koros, W.J., and Fleming, G.K. (1993). Membrane-based gas separation. Journal of Membrane Science 83, 1-80. https://doi.org/10.1016/0376-7388(93)80013-N.
- 4. Ma, Y., Zhang, F., Yang, S., and Lively, R.P. (2018). Evidence for entropic diffusion selection of xylene isomers in carbon molecular sieve membranes. Journal of Membrane Science *564*, 404-414. https://doi.org/10.1016/j.memsci.2018.07.040.
- 5. Sattler, J.J.H.B., Ruiz-Martinez, J., Santillan-Jimenez, E., and Weckhuysen, B.M. (2014). Catalytic Dehydrogenation of Light Alkanes on Metals and Metal Oxides. Chemical Reviews *114*, 10613-10653. 10.1021/cr5002436.
- 6. Motagamwala, A.H., Almallahi, R., Wortman, J., Igenegbai, V.O., and Linic, S. (2021). Stable and selective catalysts for propane dehydrogenation operating at thermodynamic limit. Science *373*, 217-222. 10.1126/science.abg7894.
- 7. Murphy, R.M. (2007). Introduction to chemical processes: principles, analysis, synthesis (McGraw-Hill Higher Education).
- 8. Treacy, M.M.J., and Higgins, J.B. (2007). Collection of Simulated XRD Powder Patterns for Zeolites Fifth (5th) Revised Edition (Elsevier Science).
- 9. Camblor, M.A., Corma, A., and Pérez-Pariente, J. (1993). Synthesis of titanoaluminosilicates isomorphous to zeolite Beta, active as oxidation catalysts. Zeolites *13*, 82-87. https://doi.org/10.1016/0144-2449(93)90064-A.
- 10. Sudhakar Reddy, J., and Sayari, A. (1995). A simple method for the preparation of active Ti beta zeolite catalysts. In Studies in Surface Science and Catalysis, H.K. Beyer, H.G. Karge, I. Kiricsi, and J.B. Nagy, eds. (Elsevier), pp. 309-316. https://doi.org/10.1016/S0167-2991(06)81237-1.
- 11. Li, Q., Sui, Z., Zhou, X., and Chen, D. (2011). Kinetics of propane dehydrogenation over Pt–Sn/Al2O3 catalyst. Applied Catalysis A: General 398, 18-26. https://doi.org/10.1016/j.apcata.2011.01.039.
- 12. Gómez-Quero, S., Tsoufis, T., Rudolf, P., Makkee, M., Kapteijn, F., and Rothenberg, G. (2013). Kinetics of propane dehydrogenation over Pt–Sn/Al2O3. Catalysis Science & Technology *3*, 962-971. 10.1039/C2CY20488F.
- 13. Sheintuch, M., Liron, O., Ricca, A., and Palma, V. (2016). Propane dehydrogenation kinetics on supported Pt catalyst. Applied Catalysis A: General 516, 17-29. https://doi.org/10.1016/j.apcata.2016.02.009.
- 14. Virnovskaia, A., Rytter, E., and Olsbye, U. (2008). Kinetic and Isotopic Study of Ethane Dehydrogenation over a Semicommercial Pt,Sn/Mg(Al)O Catalyst. Industrial & Engineering Chemistry Research 47, 7167-7177. 10.1021/ie800361a.
- 15. Medrano, J.A., Julián, I., García-García, F.R., Li, K., Herguido, J., and Menéndez, M. (2013). Two-Zone Fluidized Bed Reactor (TZFBR) with Palladium Membrane for Catalytic Propane Dehydrogenation: Experimental Performance Assessment. Industrial & Engineering Chemistry Research *52*, 3723-3731. 10.1021/ie303185p.
- 16. Dangwal, S., Ronte, A., Mahmodi, G., Zarrintaj, P., Lee, J.S., Saeb, M.R., Gappa-Fahlenkamp, H., and Kim, S.-J. (2021). Propane Dehydrogenation Reaction in a High-Pressure Zeolite Membrane Reactor. Energy & Fuels *35*, 19362-19373. 10.1021/acs.energyfuels.1c02473.

- 17. Kim, S.-J., Liu, Y., Moore, J.S., Dixit, R.S., Pendergast, J.G., Jr., Sholl, D., Jones, C.W., and Nair, S. (2016). Thin Hydrogen-Selective SAPO-34 Zeolite Membranes for Enhanced Conversion and Selectivity in Propane Dehydrogenation Membrane Reactors. Chemistry of Materials *28*, 4397-4402. 10.1021/acs.chemmater.6b01458.
- 18. Kim, S.-J., Tan, S., Taborga Claure, M., Briones Gil, L., More, K.L., Liu, Y., Moore, J.S., Dixit, R.S., Pendergast, J.G., Jr., Sholl, D.S., et al. (2016). One-Step Synthesis of Zeolite Membranes Containing Catalytic Metal Nanoclusters. ACS Applied Materials & Interfaces 8, 24671-24681. 10.1021/acsami.6b06576.
- 19. Yildirim, Y., Gobina, E., and Hughes, R. (1997). An experimental evaluation of high-temperature composite membrane systems for propane dehydrogenation. Journal of Membrane Science *135*, 107-115. https://doi.org/10.1016/S0376-7388(97)00133-6.
- Weyten, H., Luyten, J., Keizer, K., Willems, L., and Leysen, R. (2000). Membrane performance: the key issues for dehydrogenation reactions in a catalytic membrane reactor. Catalysis Today *56*, 3-11. https://doi.org/10.1016/S0920-5861(99)00257-6.
- 21. Quicker, P., Höllein, V., and Dittmeyer, R. (2000). Catalytic dehydrogenation of hydrocarbons in palladium composite membrane reactors. Catalysis Today *56*, 21-34. https://doi.org/10.1016/S0920-5861(99)00259-X.
- 22. Wolfrath, O., Kiwi-Minsker, L., and Renken, A. (2001). Novel Membrane Reactor with Filamentous Catalytic Bed for Propane Dehydrogenation. Industrial & Engineering Chemistry Research 40, 5234-5239. 10.1021/ie001077z.
- 23. Kiwi-Minsker, L., Wolfrath, O., and Renken, A. (2002). Membrane reactor microstructured by filamentous catalyst. Chemical Engineering Science *57*, 4947-4953. https://doi.org/10.1016/S0009-2509(02)00294-4.
- 24. Chang, J.-S., Roh, H.-S., Park, M.S., and Park, S.-E. (2002). Propane dehydrogenation over a hydrogen permselective membrane reactor. BULLETIN-KOREAN CHEMICAL SOCIETY *23*, 674-678. https://doi.org/10.5012/bkcs.2002.23.5.674.
- Wu, Z., Hatim, I.M., Kingsbury, B.F., Gbenedio, E., and Li, K. (2009). A novel inorganic hollow fiber membrane reactor for catalytic dehydrogenation of propane. AIChE journal *55*, 2389-2398. https://doi.org/10.1002/aic.11864.
- 26. Gbenedio, E., Wu, Z., Hatim, I., Kingsbury, B.F.K., and Li, K. (2010). A multifunctional Pd/alumina hollow fibre membrane reactor for propane dehydrogenation. Catalysis Today *156*, 93-99. https://doi.org/10.1016/j.cattod.2010.04.044.
- 27. Didenko, L.P., Savchenko, V.I., Sementsova, L.A., Chizhov, P.E., and Bykov, L.A. (2013). Dehydrogenation of propane in a combined membrane reactor with hydrogen-permeable palladium module. Petroleum Chemistry *53*, 27-32. 10.1134/S0965544113010039.
- 28. Medrano, J.-A., Julián, I., Herguido, J., and Menéndez, M. (2013). Pd-Ag Membrane Coupled to a Two-Zone Fluidized Bed Reactor (TZFBR) for Propane Dehydrogenation on a Pt-Sn/MgAl2O4 Catalyst. Membranes *3*, 69-86. 10.3390/membranes3020069.
- 29. Sheintuch, M., and Dessau, R.M. (1996). Observations, modeling and optimization of yield, selectivity and activity during dehydrogenation of isobutane and propane in a Pd membrane reactor. Chemical Engineering Science *51*, 535-547. https://doi.org/10.1016/0009-2509(95)00285-5.
- 30. Pati, S., Dewangan, N., Wang, Z., Jangam, A., and Kawi, S. (2020). Nanoporous Zeolite-A Sheltered Pd-Hollow Fiber Catalytic Membrane Reactor for Propane Dehydrogenation. ACS Applied Nano Materials *3*, 6675-6683. 10.1021/acsanm.0c01131.
- 31. Collins, J.P., Schwartz, R.W., Sehgal, R., Ward, T.L., Brinker, C.J., Hagen, G.P., and Udovich, C.A. (1996). Catalytic Dehydrogenation of Propane in Hydrogen Permselective Membrane Reactors. Industrial & Engineering Chemistry Research *35*, 4398-4405. 10.1021/ie960133m.
- Weyten, H., Keizer, K., Kinoo, A., Luyten, J., and Leysen, R. (1997). Dehydrogenation of propane using a packed-bed catalytic membrane reactor. AIChE journal *43*, 1819-1827. https://doi.org/10.1002/aic.690430717.

- 33. Schäfer, R., Noack, M., Kölsch, P., Thomas, S., Seidel-Morgenstern, A., and Caro, J. (2001). Development of a H2-selective SiO2-membrane for the catalytic dehydrogenation of propane. Separation and Purification Technology 25, 3-9. https://doi.org/10.1016/S1383-5866(01)00085-5.
- 34. Schäfer, R., Noack, M., Kölsch, P., Stöhr, M., and Caro, J. (2003). Comparison of different catalysts in the membrane-supported dehydrogenation of propane. Catalysis Today 82, 15-23. https://doi.org/10.1016/S0920-5861(03)00198-6.
- 35. Ishii, K., Nagataki, Y., Yoshiura, J., Saito, Y., Nagataki, T., and Nomura, M. (2021). Development of Hydrogen Permselective Membranes for Propylene Production. JOURNAL OF CHEMICAL ENGINEERING OF JAPAN *54*, 260-265. 10.1252/jcej.20we082.
- 36. Bitter, J. (1986). Process and apparatus for the dehydrogenation of organic compounds. UK Patent Application.
- Ziaka, Z.D., Minet, R.G., and Tsotsis, T.T. (1993). A high temperature catalytic membrane reactor for propane dehydrogenation. Journal of Membrane Science 77, 221-232. https://doi.org/10.1016/0376-7388(93)85071-4.
- 38. Ziaka, Z., Minet, R., and Tsotsis, T. (1993). Propane dehydrogenation in a packed-bed membrane reactor. AIChE Journal (American Institute of Chemical Engineers);(United States) 39. https://doi.org/10.1002/aic.690390317.
- 39. Bobrov, V.S., Digurov, N.G., and Skudin, V.V. (2005). Propane dehydrogenation using catalytic membrane. Journal of Membrane Science 253, 233-242. https://doi.org/10.1016/j.memsci.2004.11.037.
- 40. Amer, J., Burgard, M., and Ernst, B. (2009). High resistance to coking of a hydrogen selective nickel membrane implemented in a membrane reactor for the catalytic dehydrogenation of propane. pp. 129-130.
- 41. Gobina, E., and Hughes, R. (1994). Ethane dehydrogenation using a high-temperature catalytic membrane reactor. Journal of Membrane Science 90, 11-19. https://doi.org/10.1016/0376-7388(94)80030-8.
- 42. Champagnie, A.M., Tsotsis, T.T., Minet, R.G., and Webster, A.I. (1990). A high temperature catalytic membrane reactor for ethane dehydrogenation. Chemical Engineering Science 45, 2423-2429. https://doi.org/10.1016/0009-2509(90)80124-W.
- 43. Champagnie, A.M., Tsotsis, T.T., Minet, R.G., and Wagner, E. (1992). The study of ethane dehydrogenation in a catalytic membrane reactor. Journal of Catalysis *134*, 713-730. https://doi.org/10.1016/0021-9517(92)90355-L.
- 44. Avila, A.M., Yu, Z., Fazli, S., Sawada, J.A., and Kuznicki, S.M. (2014). Hydrogen-selective natural mordenite in a membrane reactor for ethane dehydrogenation. Microporous and Mesoporous Materials *190*, 301-308. https://doi.org/10.1016/j.micromeso.2014.02.024.
- 45. Dangwal, S., Liu, R., and Kim, S.-J. (2017). High-temperature ethane dehydrogenation in microporous zeolite membrane reactor: Effect of operating conditions. Chemical Engineering Journal *328*, 862-872. https://doi.org/10.1016/j.cej.2017.07.108.
- 46. Wang, L., Murata, K., and Inaba, M. (2003). Production of pure hydrogen and more valuable hydrocarbons from ethane on a novel highly active catalyst system with a Pd-based membrane reactor. Catalysis Today 82, 99-104. https://doi.org/10.1016/S0920-5861(03)00207-4.
- 47. Ahn, S.-J., Yun, G.-N., Takagaki, A., Kikuchi, R., and Oyama, S.T. (2018). Effects of pressure, contact time, permeance, and selectivity in membrane reactors: The case of the dehydrogenation of ethane. Separation and Purification Technology 194, 197-206. https://doi.org/10.1016/j.seppur.2017.11.037.
- 48. Galuszka, J., Giddings, T., and Clelland, I. (2009). Catalytic Dehydrogenation of Ethane in Hydrogen Membrane Reactor. In Inorganic Membranes for Energy and Environmental Applications, A.C. Bose, ed. (Springer New York), pp. 299-311. 10.1007/978-0-387-34526-0_17.

- 49. Szegner, J., Yeung, K.L., and Varma, A. (1997). Effect of catalyst distribution in a membrane reactor: experiments and model. AIChE journal 43, 2059-2072. https://doi.org/10.1002/aic.690430814.
- 50. Davidson, T.A., and Mines, U.S.B.o. (1993). A Simple and Accurate Method for Calculating Viscosity of Gaseous Mixtures (U.S. Department of the Interior, Bureau of Mines).
- 51. A. Maddah, H. (2018). A Comparative Study between Propane Dehydrogenation (PDH) Technologies and Plants in Saudi Arabia. American Scientific Research Journal for Engineering, Technology, and Sciences 45, 49-63.
- 52. Mickey, S.R., Schönfelder, M.G., and Wünning, J.G. (2017). Efficient Gas Heating of Industrial Furnaces. Thermal Processing, Pelham, 1.
- 53. Reddy, S., and Vyas, S. (2009). Recovery of Carbon Dioxide and Hydrogen from PSA Tail Gas. Energy Procedia *I*, 149-154. https://doi.org/10.1016/j.egypro.2009.01.022.
- 54. High-Pressure Propylene Splitter Column System. International Process Plants.
- 55. Nawaz, Z. (2015). Light alkane dehydrogenation to light olefin technologies: a comprehensive review. *31*, 413-436. doi:10.1515/revce-2015-0012.
- 56. Choi, S.W., Sholl, D.S., Nair, S., Moore, J.S., Liu, Y., Dixit, R.S., and Pendergast, J.G. (2017). Modeling and process simulation of hollow fiber membrane reactor systems for propane dehydrogenation. AIChE Journal *63*, 4519-4531. https://doi.org/10.1002/aic.15785.
- 57. Ethylene, Propylene, Olefins. Koch-Glitsch.
- 58. Miremadi, M., Musso, C., and Oxgaard, J. (2013). Chemical innovation: An investment for the ages. McKinsey on Chemicals 2, 3-12.
- 59. United States Federal Corporate Tax Rate. (2022). https://tradingeconomics.com/united-states/corporate-tax-rate.
- 60. Jenkins, S. (2019). Chemical Engineering plant cost index: 2018 annual value. Chemical Engineering *I*.
- 61. Jenkins, S. (2021). 2021 CEPCI Updates: September (prelim.) and August (final). Chemial Engineering: Essentials for the CPI Professional.
- 62. Malek, A., and Farooq, S. (1998). Hydrogen purification from refinery fuel gas by pressure swing adsorption. AIChE Journal 44, 1985-1992. https://doi.org/10.1002/aic.690440906.
- 63. Grande, C.A., Gigola, C., and Rodrigues, A.E. (2002). Adsorption of Propane and Propylene in Pellets and Crystals of 5A Zeolite. Industrial & Engineering Chemistry Research *41*, 85-92. 10.1021/ie010494o.
- 64. Wu, Y., and Weckhuysen, B.M. (2021). Separation and purification of hydrocarbons with porous materials. Angewandte Chemie International Edition *60*, 18930-18949. https://doi.org/10.1002/anie.202104318.
- 65. Van Allsburg, K.M., Tan, E.C.D., Super, J.D., Schaidle, J.A., and Baddour, F.G. (2022). Early-stage evaluation of catalyst manufacturing cost and environmental impact using CatCost. Nature Catalysis *5*, 342-353. 10.1038/s41929-022-00759-6.
- 66. Walas, S. (1988). Chemical Process Equipment Selection and Design. 3rd editions. Butterworth. United States of America.
- 67. Maximum Allowable Stress Values ASME Pressure Vessels Code. EngineersEdge. https://www.engineersedge.com/pressure,045vessel/maximum_allowable_stress_values_13906.ht m.
- 68. Thin Wall Pressure Vessels ASME Equation and Calculator. EngineersEdge. https://www.engineersedge.com/pressure,045vessel/thin wall pressure vessels 13909.htm.
- 69. Metals and Alloys Densities. The Engineering ToolBox. https://www.engineeringtoolbox.com/metal-alloys-densities-d 50.html.
- 70. Towler, G., and Sinnott, R. (2021). Chemical engineering design: principles, practice and economics of plant and process design (Butterworth-Heinemann).

- 71. Lang, W.-Z., Hu, C.-L., Chu, L.-F., and Guo, Y.-J. (2014). Hydrothermally prepared chromia-alumina (xCr/Al2O3) catalysts with hierarchical structure for propane dehydrogenation. RSC Advances 4, 37107-37113. 10.1039/C4RA06277A.
- 72. Cabrera, F., Ardissone, D., and Gorriz, O.F. (2008). Dehydrogenation of propane on chromia/alumina catalysts promoted by tin. Catalysis Today *133-135*, 800-804. https://doi.org/10.1016/j.cattod.2007.12.039.
- 73. Alibaba UIV CHEM Platinum dichloride 10025-65-7 Platinum(II) chloride factory sells self costeffective PtCl2. https://www.alibaba.com/product-detail/UIV-CHEM-Platinum-dichloride-10025-65 1600090416422.html?spm=a2700.7724857.0.0.65164a060zVcNi.
- 74. Alibaba High quality Tetrapropylammonium hydroxide CAS 4499-86-9. https://www.alibaba.com/product-detail/High-quality-Tetrapropylammonium-hydroxide-CAS-4499 1600255798342.html.
- 75. Made-in-China Tetraethoxysilane. https://www.made-in-china.com/price/tetraethoxysilane-price.html.
- 76. Alibaba Nickel Acetylacetonate. https://www.alibaba.com/showroom/nickel-acetylacetonate.html.
- 77. Singh, R.R. (2020). High Selectivity and Throughput Carbon Molecular Sieve Hollow Fiber Membrane-Based Modular Air Separation Unit for Producing High Purity O2. 2020 Gasification Project Review Meeting DOE –Fossil Energy/NETL.
- 78. Heating Oil and Propane Update. (2022). Energy Information Administration. https://www.eia.gov/petroleum/heatingoilpropane/.
- 79. Electric Power Monthly. (2022). Energy Information Administration. https://www.eia.gov/electricity/monthly/epm table grapher.php?t=epmt 5 6 a.
- 80. Henry Hub Natural Gas Spot Price. (2022). Energy Information Administration. https://www.eia.gov/dnav/ng/hist/rngwhhdm.htm.
- 81. Price of refrigeration, water. (2018). Aspentech, Aspen Plus.
- 82. Global Hydrogen Review. (2021). IEA. https://www.iea.org/reports/global-hydrogen-review-2021/executive-summary.
- 83. Peters, M.S., Timmerhaus, K.D., and West, R.E. (2003). Plant design and economics for chemical engineers (McGraw-Hill New York).
- 84. Bare, J. (2011). TRACI 2.0: the tool for the reduction and assessment of chemical and other environmental impacts 2.0. Clean Technologies and Environmental Policy 13, 687-696. 10.1007/s10098-010-0338-9.
- 85. Vengateson, U. (2017). Engineering Practice Cooling Towers: Estimate Evaporation Loss and Makeup Water Requirements. Chemical Engineering *124*, 64-67.
- 86. Solar photovoltaic generators receive higher electricity prices than other technologies. (2019). Energy Information Administration. https://www.eia.gov/todayinenergy/detail.php?id=45436.
- 87. Clausi, D.T., and Koros, W.J. (2000). Formation of defect-free polyimide hollow fiber membranes for gas separations. Journal of Membrane Science *167*, 79-89. https://doi.org/10.1016/S0376-7388(99)00276-8.